FLOW ANALYSIS OF A MICRO-SCALE DUAL ROTOR VISCOUS PUMP

by

MD. NUR ALAM MONDAL

(0416102007)

Submitted in partial fulfilment of the requirements for the degree of Master of Science in Mechanical Engineering

Under the supervision of

Dr. A.B.M. Toufique Hasan

Professor

Department of Mechanical Engineering
Bangladesh University of Engineering and Technology (BUET)

BANGLADESH UNIVERSITY OF ENGINEERING AND TECHNOLOGY,
DHAKA-1000, BANGLADESH

November 2018

Certificate of Approval

The thesis titled, **"Flow Analysis of a Micro-Scale Dual Rotor Viscous Pump"**, submitted by Md. Nur Alam Mondal, Roll No: 0416102007, Session: April 2016, has been accepted as satisfactory in partial fulfilment of the requirement for the degree of Master of Science in Mechanical Engineering on 24th November 2018.

Dr. A.B.M. Toufique Hasan Professor Department of Mechanical Engineering BUET, Dhaka	Chairman (Supervisor)
Head Department of Mechanical Engineering BUET, Dhaka	Member Ex-Officio
Dr. Muhammed Mahbubur Razzaque Professor Department of Mechanical Engineering BUET, Dhaka	Member
Dr. Mohammad Mamun Professor Department of Mechanical Engineering BUET, Dhaka	Member
Dr. A. K. M. Sadrul Islam Ex-Professor Department of Mechanical and Chemical Engineering Islamic University of Technology (IUT) Gazipur	Member (External)

Candidate's Declaration

This is hereby declared that this thesis or any part of it has not been submitted elsewhere for award of any degree or diploma.

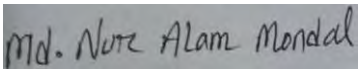

Md. Nur Alam Mondal

Acknowledgements

All the praise to the Almighty Allah for enabling me to complete this work.

I wish to express my deepest gratitude to my honourable thesis supervisor Dr. A. B. M. Toufique Hasan, Professor, Department of Mechanical Engineering, BUET for his guidance, suggestion, patience and encouragement throughout this study. Without his support, continuous guidance, meticulous suggestions and astute criticism I would not have been able to come this far.

Higher Education Quality Enhancement Project (HEQEP), UGC, MoE, GoB provided us the opportunity to use high speed computational facilities. I am really grateful to HEQEP (CP#2099-Development of Research Facilities on Biomedical Fluid Flow Phenomena) and AIF (3rd Round)-Sub-Project CP 3111 for the opportunity to use the Bio-Fluid Laboratory and High Speed Aero Laboratory of Bangladesh University of Engineering and Technology (BUET) for computational resources.

I extend my heartiest gratitude to the Head, Department of Mechanical Engineering, BUET as he has given the initial clearance to do this research work. I am also very much thankful to other faculty members for their constant support during my thesis work.

I would also like to thank my teachers, friends and juniors of Bio-Fluids Laboratory who helped me on the way either by direct help or by discussing and sharing ideas that have helped me to develop the tools in my skill set.

And last but not the least, I would like to thank my family for being persistent in supporting me throughout my research work.

Abstract

Micropump is the fundamental component of a microfluidic device and has been the subject of a number of researches for the last few decades. This type of pump can control and transfer small amount of fluid usually less than 15 μL/min. The length scale of the pump is of the order of 100 μm or less which significantly facilitates its possible applications in a number of miniature technologies such as microelectromechanical systems (MEMS), biomedical engineering, robotics, space explorations and so on. In the present study, a viscous force based pumping device is investigated. The proposed viscous pump consists of two counter rotating cylinders (rotors) which are placed symmetrically at vertical position inside a narrow channel. When the cylinders (rotors) rotate, the viscous pump could generate a net flow against an externally imposed pressure gradient.

To model the flow field around the viscous micropump, the Navier-Stokes equations have been numerically solved using Finite Volume Method (FVM). Flow has been considered to be incompressible, three dimensional (3D) and laminar. The PISO (Pressure-Implicit with Splitting of Operators) algorithm was used for the pressure-velocity coupling which ensures rapid rate of convergence without any significant loss of accuracy. Glycerine has taken as the working fluid with constant flow and thermal properties. The numerical results have been validated with available experimental data for the case of a single rotor micropump.

Results of the proposed dual rotor micropump have been reported in the form of non-dimensional flow quantities such as dimensionless average velocity, driving power and efficiency. To study the effect of geometric parameters, several pump configurations were considered with various channel height, wall clearance and channel width. The optimum size of wall clearance was determined which plays a significant role on the flow dynamics inside micropump as well as on the pump performance. For dimensionless channel heights of 2.1, 2.3, 2.5, 2.7 and 3.0, the optimum dimensionless wall clearance was found to be 0.01, 0.02, 0.05, 0.075 and 0.10 respectively, for a particular flow condition. It was also found that channel width has significant role on the performance of pump until the channel width is less or equal to 20 times the cylinder diameter. Moreover, computations have been carried out for the cases with non-Newtonian fluids (relevant to biomedical application) with power law model under different operating condition. It was observed that the performance of the proposed micropump improves in case of non-Newtonian fluids. In addition to steady flows, a number of unsteady computations have been carried out to investigate the initial transient flow dynamics of micropump operation for the cases of Newtonian and non-Newtonian fluids.

List of symbols

C_M	: Moment coefficient
C_D	: Drag coefficient
d	: Diameter of the cylinder (m)
F_D	: Drag force on cylinder (N)
h	: Half of the channel height (m)
H^*	: Non-dimensional channel height
M	: Total moment on cylinder (Nm)
m	: Consistency coefficient of Non-Newtonian fluid
n	: Power law index
P_{in}	: Pump inlet pressure (Pa)
P_{out}	: Pump outlet pressure (Pa)
P^*	: Non-dimensional pressure rise
Re	: Reynolds Number
T^*	:Non-dimensional driving power
t	: Time (s)
t^*	: Non-dimensional time
Δt	: Time step size (s)
U_{avg}	: Average velocity inside micropump (m/s)
U^*	: Non-dimensional average velocity
U	:Cylinder surface velocity (m/s)

$U(y)$	: Local velocity (m/s)
u	: Velocity in x-direction (m/s)
v	: Velocity in y-direction (m/s)
w	: Velocity in z-direction (m/s)
W	: Channel width (m)
W^*	: Non-dimensional channel width
y	: Distance from channel axis to cylinder center (m)
μ	: Absolute viscosity of fluid (kg/m-s)
υ	: Kinematic viscosity of fluid (m^2/s)
ρ	: Density of fluid (kg/m^3)
ω	: Angular velocity of cylinder (rad/s)
ε	: Wall clearance (m)
ε^*	: Non-dimensional wall clearance
η	: Pump efficiency
τ	: Shear stress on the rotor surface (Pa)
τ^*	: Non-dimensional shear stress on the rotor surface
θ	: Angular distance on rotor surface (°)

TABLE OF CONTENTS

ABSTRACT (iv)

CHAPTER 1: INTRODUCTION

1.1 Micropump 1
1.2 Applications of Micropumps 2
1.2.1 Controlled Drug and Insulin Delivery 2
1.2.2 Microelectronic Cooling 3
1.2.3 Chemical and Biological Aspects 3
1.2.4 Blood Transportation Through Artificial Heart and Valve 3
1.3 Micropump Types 5
1.3.1 Micropumps Based on Actuation Principles 6
1.4 Viscous Micropumps 8
1.5 Objectives 11
1.6 Thesis Layout 11

CHAPTER 2: LITERATURE REVIEW

2.1 Micro-scale Viscous Pump 12
2.2 Viscous Micropump Experiment with Rotating Cylinder 13
2.3 Numerical Study (2-D) on Viscous Micropump with Rotating Cylinder 14
2.4 Numerical Study (3-D) on Viscous Micropump with Rotating Cylinder 16
2.5 Viscous Micropump with Non-Newtonian Flow 17
2.6 Symmetrical Dual Cylinder Viscous Micropump 17
2.7 Motivation of Current Study 18

CHAPTER 3: COMPUTATIONAL MODEL AND SOLUTION

3.1 Micro Pump Geometry 19
3.2 Governing Equations 22
3.3 Fluid Property 22
3.4 Flow Conditions 23
3.5 Boundary Conditions 23
3.6 Solution Method 24
3.7 Grid Independency Test 25
3.8 Validation 32

CHAPTER 4: RESULTS AND DISCUSSION

4.1 Steady Flow Visualization 35

4.1.1 Streamlines 35

4.1.2 Pressure Contour 41

4.1.3 X-Velocity Contour 47

4.1.4 Wall Shear Stress Contour 53

4.1.5 Pressure Distribution 59

4.1.6 Velocity Profile 61

4.2 Optimization of the Pump Configuration 68

4.2.1 Effect of Rotor Clearance ε* and Channel Height H* 68

4.2.2 Effect of Channel Width W* 73

4.2.3 Effect of Reynolds Number 77

4.2.4 Effect of Pump Load 81

4.3 Non-Newtonian Fluid Flow in Dual rotor Micro Viscous pump 85

4.3.1 Validation with Analytical Solution 85

4.3.2 Optimization of the Model with Non-Newtonian Fluid 88

4.4 Transient Flow Behavior inside the Micropump 93

4.4.1 Time Independency Test 93

4.4.2 Transient Performance of the Viscous Micropump 95

4.4.3 Comparison with Steady State Results 100

4.5 Transient Behaviour Inside the Micropump with Non-Newtonian Fluid (n=0.785) 102

CHAPTER 6:CONCLUSIONS 108

REFERENCES 111

APPENDICES 115

Appendix-A Design of Numerical Experiments 115

Appendix-B Computational Fluid Dynamics (CFD) 117

Appendix-C Buckingham's PI Theorem 127

Computer Disk DOC and PDF version of Thesis Report

CHAPTER 1
INTRODUCTION

1.1 Micropump

Micropump is a microfluidic device which is being developed to meet the demand of both small scale flow (usually less than 15 μL/min) and high pressure fluid transport. According to the convention for MEMS (Micro-Electro Mechanical System), micropump is a specialized pump appropriate for devices with prominent features having length scales of order 100 μm or smaller. Some examples of micropump used in biomedical applications are shown in Fig. 1.1. The fluid may differ according to the application of micropump. It may be blood for the use in artificial heart valve, insulin in case of insulin supply for controlling blood glucose, drug in drug delivery system, and air in case of electronic cooling etc.

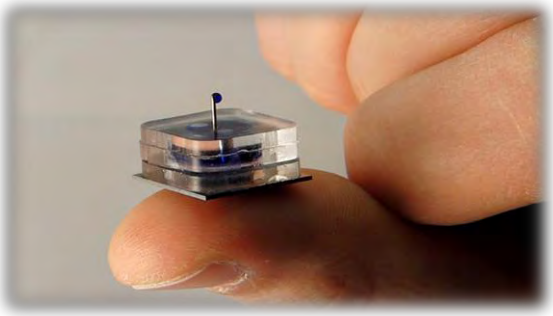

(a)a skin-contact-actuated dispenser/micropump ($14 \times 14 \times 8$ mm^3) [1]

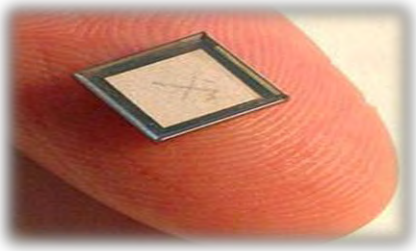

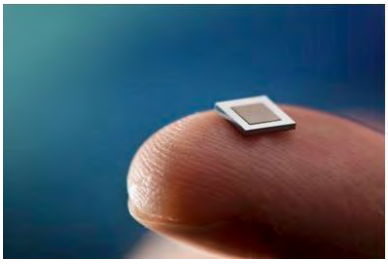

(b) Infusion micropump ($14 \times 10 \times 3$ mm^3) [2] (c) Silicon pump chip ($5 \times 5 \times 0.6$ mm^3) [3]

Fig.1.1 Micropumps in different operations

1.2 Applications of Micropumps

The wide number of applications causes several researches being carried out for the design and fabrication of micropumps. Different micropumps are effective and suitable for different applications. So there remains a wide area of research on developing more versatile micropumps that can meet multiple applications with much more effectiveness. Some of the emerging fields of micropump are described below.

1.2.1 Controlled Drug and Insulin Delivery

The one of the major field of application of micropump was in insulin delivery system for maintaining diabetic's blood sugar within a desired level without the need of frequent needle injections. A general insulin delivery system consists of a drug or insulin reservoir, a micropump for pumping insulin from the reservoir to the blood vessel through microvalves, and a control system as shown in Fig. 1.2. The purpose of the control system is to measure the glucose level of the body and send an appropriate signal to the controller to regulate the actuating signal of the micropump. The control portion is usually programmed in computer and signals are provided by proper electronic circuit arrangements. The most essential and sophisticated part is the micropump and a very good design and fabrication process is a must to obtain good and precise control of flow according to the controller signal.

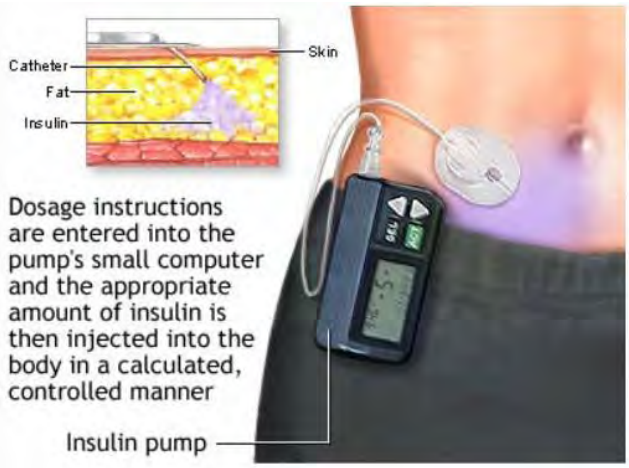

Fig.1.2An insulin pump injecting insulin through a catheter in the abdominal fat to control blood sugar level [4]

1.2.2 Microelectronic Cooling

In integrated circuit industry, micropumps are widely used as a cooling device in microelectronic components. Micropumps are capable of blowing air with a desired high flow rate and high pressure to the hot spots of microelectronic circuits and provide an effective forced convection heat transfer process. Micropumps can deliver high pressure cooling air through micro-channels in micro heat sinks. Micropumps can be built directly into the ICs as an integral part. Thus fabrication process is of great concern for the provision of sufficient delivery of coolant to the transient hot zones.

1.2.3 Chemical and Biological Aspects

Micropumps have become an essential component in such fluid transport systems which are intended to analyze live cells, DNA, etc. Cell analysis can be conducted in four stages: cell sampling, cell trapping, sorting and cytometry on chip, cell transport, and cell treatment and analysis. Micropumps with other micro-sensors and devices are widely used in each of the stages.

1.2.4 Blood Transportation Through Artificial Heart and Valve

Micropump, in a large scale, has been used as Left Ventricular Assist Device (LVAD), a mechanical heart used to pump blood in case of heart failure. LVADs pump oxygen-rich blood from the heart's left ventricle to the aorta through which it circulates throughout the body as shown in Fig. 1.3. The mechanical device has three primary components:

- A mechanical pump with an inflow and outflow cannula (tube), 10 L/min blood flow
- A system controller
- A pair of batteries

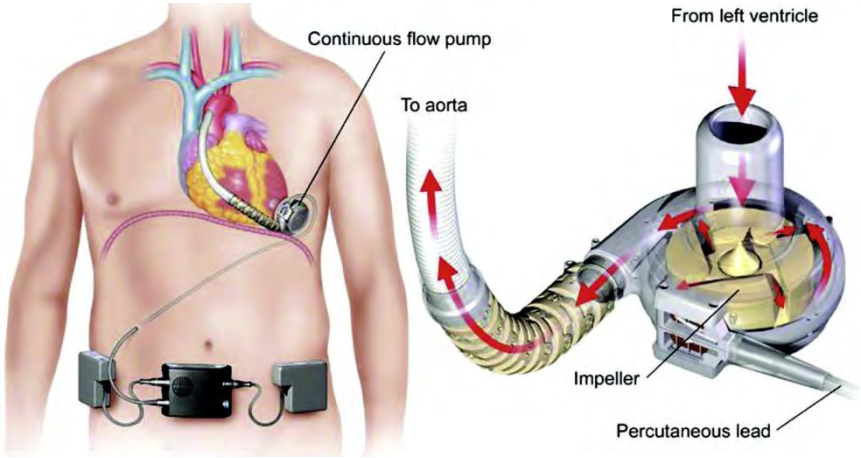

(a)

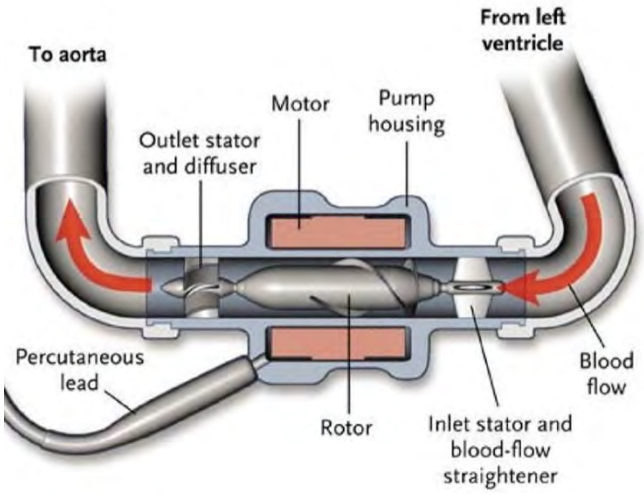

(b)

Fig.1.3 LVAD pumping O_2 rich bloodfrom heart and delivering to body [5] (b) Working principle of LVAD [5]

1.3 Micropump Types

There have been several studies where micropumps are classified differently. In a paper of Nisar et. al. [6], micropumps are classified mainly as mechanical and non-mechanical micropumps which have been broadly explained with actuation principles, performances, fabrication processes and applications. Comparison of different types of mechanical and non-mechanical micropumps has been found based on different performance parameters such as pressure, flow rate, actuation voltage, driving frequency.

Laser et. al. [7], in their review paper list different types of micropumps based on the different types of actuation principles, fluid chamber configurations like two or three chamber configurations (peristaltic micropump), valve configurations, membrane or diaphragm configurations. A broad discussion on the application of micropumps in biomedical fields such as in blood transport, and in drug delivery has been provided. Suitability and requirements of mechanical and non-mechanical micropumps with respect to different performance parameters like frequency, actuating pressure, flow rate, power consumption have been described with references.

Woias [8] classified micropumps as reciprocating and continuous flow micropumps which are basically mechanical and non-mechanical micropumps. Various types of materials and fabrication technologies have been elaborated. Micro Total Analysis System (μTAS), a special field of application of micropumps, has been explained with references.

Iverson et. al. [9] classified micropumps as diaphragm displacement pumps, fluid displacement pumps and rotary pumps. The actuation principles involved in each category have been discussed in detail. Different valve mechanisms have been discussed. Valves have been classified as dynamic geometry valve and static geometry valve. Several dynamic and static valves and their mechanisms have been discussed broadly. Non-mechanical or Electro- and magneto-kinetic micropump has been classified as electrohydrodynamic, electroosmotic, magnetohydrodynamic, electrowetting, opto-electrostatic and flexural plate wave pumps.

In the study of Blanchard et. al. [10], the different viscous pump configurations are separated into four categories: (i) disk viscous channel pumps (ii) disk viscous lobe pumps (iii) disk viscous spiral channel pumps, and (iv) cylinder viscous pumps. They compare the effectiveness of the viscous pump configuration to identify best performance configuration. The comparisons are made by using non- dimensionless parameter based on maximum flowrates, maximum pressure rise and pump geometry.Different types of other piezoelectric micropumps were designed by researchers. Many of them operate with peristaltic behavior. Some of the profound researches and designs are listed in the reference [11, 12, 13, 14, 15, and 16].

1.3.1 Micropumps Based on Actuation Principles

Based on actuation principle, micropumps can be classified as Dynamic micropumps and Mechanical displacement micropumps which is shown in Fig.1.4. Pumping action of micropumps strongly depends on the actuation method.

1.3.1.1 Non- Mechanical or Dynamic Micropumps

Dynamic micropumps simply add momentum to the fluid by means of fast moving blades or vanes or certain special designs. There is no closed volume. The fluid momentum increases while moving through open passages and then converts its high velocity into a pressure increase by exiting into a diffuser section. Dynamic pumps generally provide a higher flow rate and a much steadier discharge than positive-displacement pumps but are ineffective in handling high-viscosity liquids. Some of the common examples of dynamic micropumps found in literature are Magneto hydrodynamic (MHD), Electro hydrodynamic (EHD), Electroosmotic, Electrowetting, Electrochemical, Flexural Planer Wave (FPW), Bubble type, Evaporation type micropump etc.

1.3.1.2 Mechanical Displacement Micropumps

In Mechanical displacement micropumps, a moving boundary forces the fluid along by the volume changes. A cavity opens and the fluid is admitted through an inlet. The cavity is then closed and the fluid is squeezed through an outlet. The classic example is the mammalian heart in large scale, but mechanical versions are in wide use which may be classified as rotary pumps and reciprocating pumps. All mechanical displacement

micropumps deliver a pulsating or periodic flow as the cavity volume opens, traps, and squeezes the fluid and so they are also named as periodic micropump in some literature. Their great advantage is the delivery of any fluid regardless of viscosity.

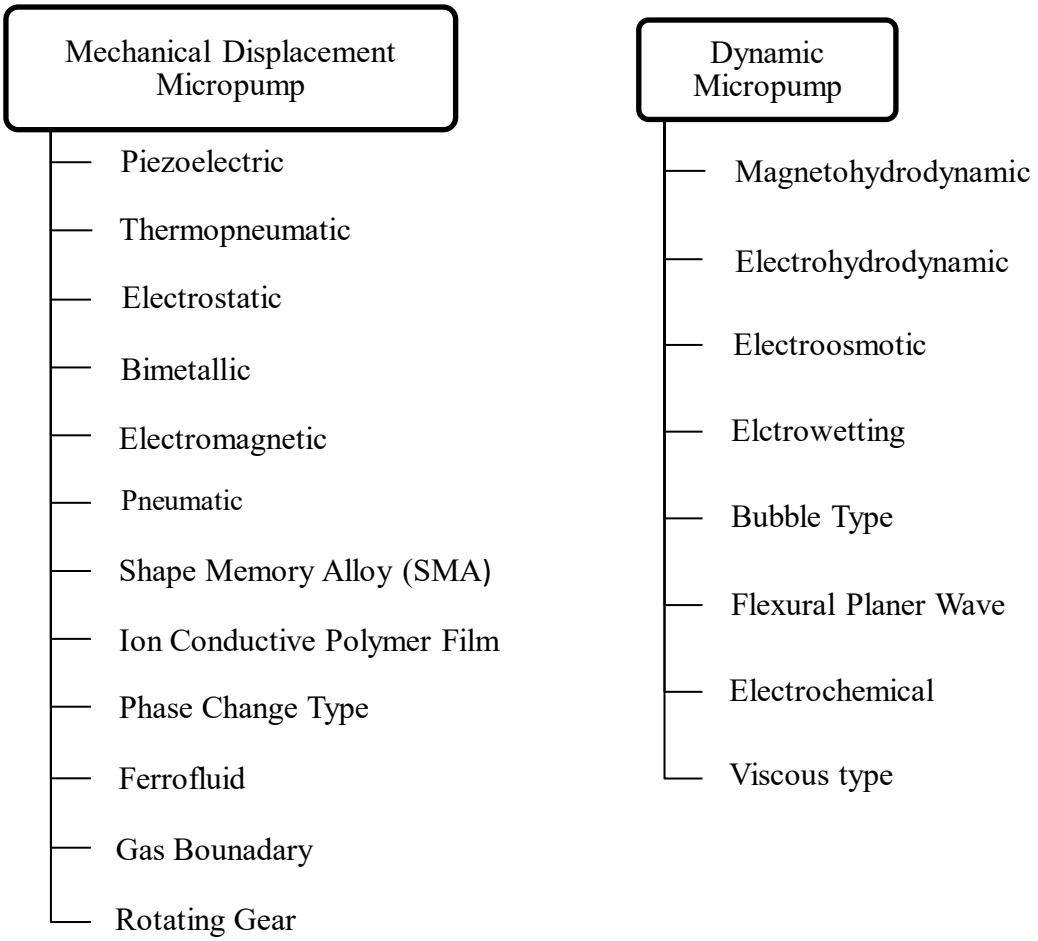

Fig.1.4Classification of micropump based on actuation method

1.4 Viscous Micropumps

Viscous pumps employ viscous fluid forces generated between two surfaces moving relative to each other to induce fluid motion and produce a pumping effect. Many viscous pumps include non-pulsatile flow rate and steady discharge pressure. Some viscous pumps show a linear relationship between flow rate and pressure rise. Moreover, some viscous pumps do not need dynamic seals or valves [17].

In case of some viscous pumps, the rotating and stationary surfaces do not touch. Hence, the possibility of debris due to wear reduces. For this reason, viscous pumps are suitable for application where accurate flow control and high levels of cleanliness are required.

A viscous micro pump as shown in Fig.1.5, was first proposed by Sen et. al. [18]. It consists of a cylinder placed eccentrically inside an extremely narrow channel, where channel axis is perpendicular to cylinder axis. When the cylinder rotates, it generates a net force on fluid due to unequal shear stresses on the top and bottom surfaces of the cylinder. This net viscous force is capable of generating a net flow against a pressure gradient.

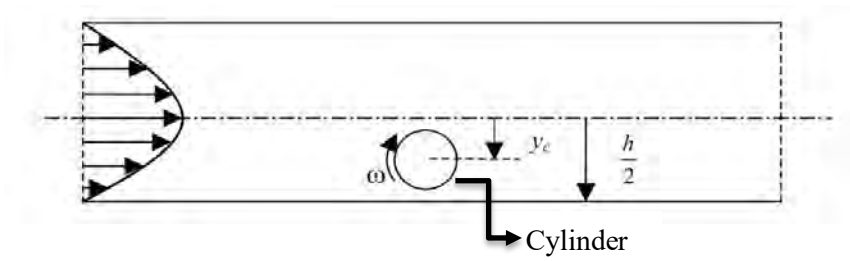

Fig.1.5 A viscous micropump with single rotating cylinder.

The design of a micropump varies according to its application and requirements. Researchers have fabricated the design to fulfill its requirement in the most effective way. A general design of a micropump especially mechanical micropump consists of

i. a pump chamber that contains fluid to be transported during the pumping action,
ii. an actuator to actuate the pumping action and
iii. valves or diffuser-nozzle elements to control the inlet and outlet flows only in one direction

The actuator action causes rotary motion of eccentrically placed rotor to provide a flow through inlet and outlet ports. The rotary motion creates unequal shear stress in upper and lower gap which in turns develop a pressure difference between upstream to downstream. This pressure difference provides a net flow from the inlet to the outlet. The pumping action is strongly dependent on the actuating principle and also on the design of the micropump. The working principle of a viscous micropump is demonstrated in Fig. 1.6.

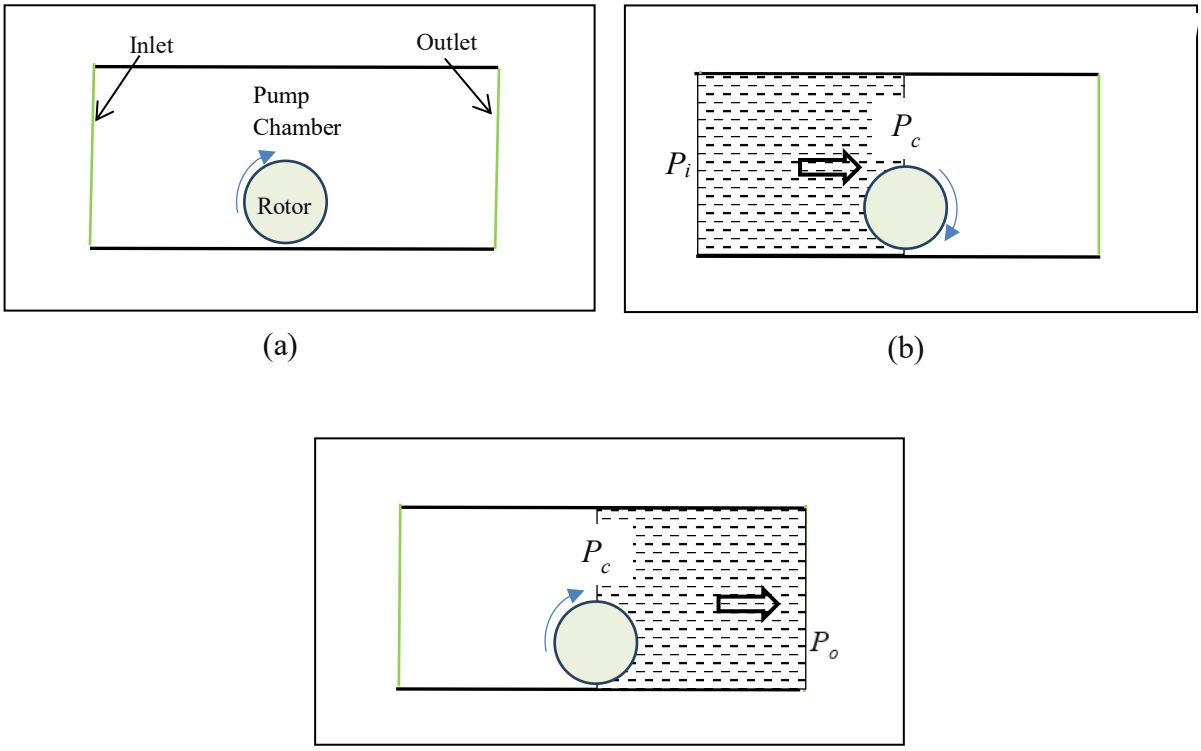

Fig.1.6 (a) 2D schematic diagram of a general viscous micropump;
(b) Suction side (P_c<P_i); (c) Delivery side ($P_c > P_o$)

However, all studies on viscous micropump assume two-dimensional behavior and the reported main drawback of such pump with single cylinder lies in poor efficiency in the range of 2-3%. To increase the pump efficiency, a concept of symmetrically placed dual rotors (in vertical orientation) is being considered in the present research which is shown in Fig. 1.7. A three-dimensional computation is performed to analyze the physical flow dynamics of a micro-scale viscous pump. The pressure difference between the inlet and outlet of the pump and the rotor surface speed are used as major operational conditions to determine the pump performance of the pumps. Different flow patterns and vortex structures at different pump configurations are presented to interpret the flow dynamic behavior. As the numerical results are based on a parametric study, the whole simulation process of this present study is summarized in design of numerical experiments section (Appendix-A).

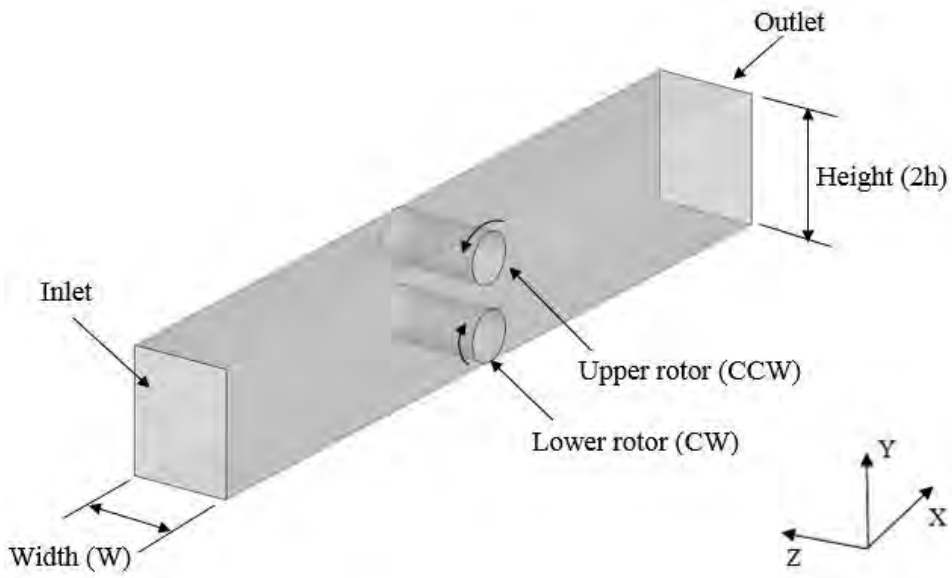

Fig.1.7 3D symmetrically placed dual rotor viscous micropump

1.5 Objectives

The specific objectives of the present study are:

- To develop a three-dimensional computational model to analyze the flow characteristics inside a micro-scale viscous pump and validate the model with available experimental results.
- To employ the above validated computational model to investigate the flow dynamic behavior of a dual rotor micro-scale viscous pump in case of Newtonian fluid.
- To characterize the non-Newtonian flow dynamics (relevant to biomedical application) inside a dual rotor micro-scale viscous pump under different operating conditions.
- To investigate the effects of geometric configurations such as channel height, width, rotor clearanceand so on of a dual rotor micro-scale pump using a parametric study for the cases of Newtonian and non-Newtonian fluids.
- To analyze the effects of pump load and Reynolds number on pump flow performance both in cases of Newtonian and non-Newtonian fluids.

1.6 Thesis Layout

- Complementing the introduction above, a thorough literature review of relevant work is presented in Chapter 2.
- The physical model, governing equations, boundary conditions, numerical simulation approach by finite volume method and the validation of the numerical method of present computational study are discussed in chapter 3.
- The detailed study of flow characteristic inside the micro-scale viscous pump and the optimal analysis of the pimp configuration are presented in Chapter 4. The study of unsteady behavior inside the pump are also presented. Moreover, the effects on flow dynamic with non-Newtonian fluidare analyzed in detail.
- Finally, observations are summarized, conclusions are made, and reflections for future work are articulated in Chapter 5.

CHAPTER 2
LITERATURE REVIEW

In the last decade, technology has blessed us with different types of mini and micro machines that are increasingly implemented in our daily life applications. These micro machines include micropumps, micro sensors, micro actuators, microchips etc. Among these micro machines, micropumps are the most promising micro electromechanical systems (MEMS) and are ready to be implemented into the mainstream. The pioneering work on micropump as a microfluidic device started in the early 1975. Based on this pioneering work, research and development on micropumps using microfabrication technology started in around 1980 and shifted towards MEMS area in around 1990. Since then, development on different aspects of micropumps is going on with high acceleration. In the past 25 years, using the blessing of microfabrication technology, the fields of application of micropumps extend from biomedical industry, genetic analysis and cell analysis to microelectronic industry and even in robotic and space exploration fields. Several review papers are available in literature where it describes the different types of micropumps, their characteristics performance and compatibility with different fields of application.

Micro pumps are designed completely in different principle than those applied in traditional pumps like axial or centrifugal pumps. Because, in small scale systems, micro dimensions limit the effect of centrifugal forces and inertia forces in general and the large surface to volume ratio enhances the effect of viscous force, making it dominant force in fluid transport[19].

2.1Micro-scale Viscous Pump

Arafaet. al. [20]discussed a number of viscous pump applications including different configurations of viscous pumps to determine the optimal arrangement for a specific application.

Blanchard et al. [21] presented experimental data for a single-disk (10.16 mm diameter) viscous pump, and a double-disk viscous pump where each has a disk inner radius of 1.19 mm, outer channel radius of 2.38 mm and a depth of 40, 73, 117 or 246 micrometers. Sato et. al. [22] analyzed a viscous pump with the multiple spiral channel arrangement with an outer pump radius of 50mm. Winoto[23], and Yohanand and Winoto[24]described viscous pumps with radial pumping grooves.Etsionet. al. [25] presented an analysis of a macroscale viscous pump that uses the semi-circular lobe arrangement.Green et al. [26] gave experimental results for this type of pump configuration with an outer radius of 55 mm.

Since micropumps operate as a result from completely different principles from traditional pumps, different designs and models were introduced. Positive displacement micropumps require check valves at the inlet and outlet ports but the design gets complicated especially on such small scales. To simplify the design, Stemmeet. al. [27] suggested replacing the check valves with a nozzle at the inlet and a diffuser at the exit, as reported in Erik et. al. [28].

To overcome the valve problems associated with positive displacement pumps, several pumping ideas and designs were proposed. In a nutshell, all the micropump concepts mentioned above are applicable but they are complex in design and require several auxiliary components in order to make the fluid environment suitable for pumping action to occur.

2.2 Viscous Micropump Experiment with Rotating Cylinder

Sen et al. [18] first introduced viscous micropump which is both suitable for microscale application and simple in design. The viscous micropump is simply a cylinder placed eccentrically inside a narrow channel where the cylinder axis is perpendicular to the channel axis. When the cylinder rotates, the unequal shear stresses on the upper and lower surfaces of the cylinder generate a net force and it is transferred to the fluid. The operation of such pumps depends on viscous force and can operate smoothly where the viscous forces are dominant. Sen et al. performed an experiment to test the pump performance.

The study focused on the effect of the channel height, rotor eccentricity, and angular velocity of the rotor on the pump performance and on the fluid velocity in the duct.

2.3 Numerical Study (2-D) on Viscous Micropump with Rotating Cylinder

Several numerical studies have been carried out to investigate the viscous micropump. Sharatchandra et. al. [29]performed a numerical simulation of the viscous micropump solving Navier-Stokes equations for the case of cylindrical rotor. The highest average velocity was achieved when the spacing between the plates is around one and half times the cylinder diameter for a fixed eccentricity or at the maximum eccentricity for a fixed plate spacing. The load versus flow rate curve was also plotted. The maximum efficiency of the pump was found to be approximately 2.5% for the optimum plate spacing. It was observed that viscous dissipation might cause a measurable temperature rise since viscous forces are the driving forces.

Theyused non-orthogonal curvilinear co-ordinates in their computation. Elliptically generated grids were used for the discretization of the computational domain. They computed the velocity profiles for Wannier problem using a 60 x 74 Grid. They showed the effect of eccentricity and plate spacing on the average velocity. This study also showed the surface plot of average velocity.

Sharatchandra et al. [29] also studied the slip effect on micropump performance. They considered a non-dimensional parameter Knudsen number to explain the slip effect, where the Knudsen number is defined as the ratio of the mean free path of gas molecules to the diameter of the rotor. Slip effects were studied for gas flows and it was shown that these effects, which tend to reduce the induced flow rate, are significant only for Knudsen numbers greater than 0.1.

In order to check the effect of viscous dissipation on the performance of micropump, the same team performed another numerical simulation [30]. They solved the continuity equation, the momentum equation with temperature dependent viscosity and the energy equation with viscous dissipation terms retained, all coupled together.

The transient performance of a single-rotor viscous micropump was investigated by Abdelgawad et al. [31].The effect of the microchannel height, rotor eccentricity, Reynolds number, and pump load on the transient performance of the single-rotor viscous micropump was studied in detail. It was found that the rotor eccentricity affects the transient performance of the micropump most significantly. Some steady-state simulations were also performed and the performance was compared to the available experimental data. The results obtained from this computation showed very good agreement with the experimental data.

Numerous studies have been performed to find out the effect of channel curvature on the performance of micropump. Silva et al. [32] presented the effect of geometric parameters such as channel height and rotor eccentricity on the mass flow rate and power consumption of a two-dimensional microscale viscous pump. The objective was to maximize the mass flow rate and at the same time minimize shaft power consumption when an external pressure load is applied along the channel that houses the rotor. In this study three different configurations of viscous micropump were considered. They are two curved housed pumps (L- and U- shaped housings) and a straight housed pump (I-shaped housing).

Because the performance of the viscous micropumps are based on the asymmetric placement of the rotor within the surrounding housing, the numerical results show that the rotor eccentricity and the channel height have a major effect on the mass flow rate generated by the rotor and on the shaft power demanded by the rotor.The results also showed that micropumps with curved housing (i.e., L- and U-shaped configurations) not only provide higher mass flow rates when compared with straight housed pumps, but also demand less shaft power to operate. Optimized geometric dimensions of all three configurations were presented for several values of the Reynolds number and pressure load.

In the study of Silva et al. [32], simulations were performed using the Finite Elements Method toolbox COMSOL Multiphysics, v. 3.2 (COMSOL MultiPhysics Inc., 2005). Second and first-order Lagrange p2–p1 mixed finite-elements were used to stabilize the pressure (i.e., second-order Lagrange elements to model velocity and linear Lagrange

elements for the pressure). Moreover, the mesh density was exhaustively tested in order to guarantee that the results were mesh-independent.

Dong Jin Kang [33] also showed the effects of channel curvature on the performance of viscous micropumps. Kang numerically investigated the effects of channel curvature on the performance of viscous micropumps with a circular channel using the Navier-Stokes equations. In this study, channel curvature was defined as the reciprocal of the radius of a circular arc along the centerline of the channel.The performance of viscous micro-pumps was studied in terms of the dimensionless mass flow rate and dimensionless driving power. To study the effects of channel curvature, various pumps were simulated by varying the radius and height of the channel, and the eccentricity of the rotor. Numerical results showed that the channel curvature plays a significant role in the performance of viscous micropumps.

Jianfeng et al. [34] simulated two different kinds of two stage viscous pumps and showed that the rotor configuration inside pump house plays an important role in the performance of viscous pumps.Lu et. al. [35]investigated the flow patterns and dynamic performance of viscous micropump with aligned and staggered rotors in a straight channel. The same team also studied a novel viscous pump with groove under rotor[36].

Phuttavonget. al. [37], numerically studied the flow behaviors induced by rotating cylinder with different rotor geometries. They showed that non-circular rotor shape could induce discrete flow structure and performance. Yokota et al. [38] investigated the pump where various vortex structures were detected. The dynamic behavior of flow over a rotating cylinder is explored by Martin et. al. [39] and Rao et al. [40].

2.4 Numerical Study (3-D) on Viscous Micropump with Rotating Cylinder

Decourtye et al. [41] introduced three-dimensional effects of the sidewalls of the channel in their study. In this case, the pump average velocity decreased with lower channel width, yet pumping action existed even for channel widths less than the rotor diameter. However, effective pumping is still observed with extremely narrow channel. In this study, full Navier-Stokes, finite-element simulations were carried out to study the

influence of the width and other geometric as well as dynamic parameters. The results were compared to previous two-dimensional numerical and physical experiments.

2.5 Viscous Micropump with Non-Newtonian Fluid

El-Sadiet. al. [42] performed numerical modeling of colloidal fluid in a viscous micropump. In this study, two-dimensional non-Newtonian simulations of a viscous micropump were performed. The effect of the height, rotor eccentricity of viscous micropump and dynamic parameters on the flow behavior of colloidal liquid in a viscous micropump was studied in this research.

Silva et. al. [43] investigated micropump with blood flow by considering non-Newtonian power law index0.5, 0.785, 1.0 or 1.5. They studied the effect of geometric parameter and curvature on pump performance as well as optimized the geometry for both straight and curved pump house for a particular flow condition.

2.6 Symmetrical Dual Cylinder Viscous Micropump

As an extension of the previous research [19], Abdelgawad et al. [44] conducted another study. This study focused on the transient and steady-state performance of multistage viscous micropumps where more than one rotor was used in order to enhance the performance. The performance of the dual-horizontal, triple-horizontal, symmetrical dual-vertical, and the eight-shaped rotors were compared to those of the single-rotor viscous micro pump. Among these, the symmetrical dual vertical rotor micropump achieved the best efficiency and highest flowrate over a wider pump load operating range.

2.7 Motivation of Current Study

Asdiscussed in the previous sections, a lot of studies, both experimental and computational,on micro-scale viscous pump is done for years and research is still going on. Since most of the studies on cylinder viscous pump are carried out by 2-D assumption, three-dimensional analysis will introduce new flow physics of a micro-scale viscous pump. The phenomenon of unsteady effect on flow inside the pump is still unknown. Moreover, in most of the study on micropump, fluid is considered as Newtonian. But in reality, the viscosity in most of the fluids does not remain constant. Therefore, in the present study the effect of geometric parameters on 3-D micropump, the unsteady effect of flow dynamics and the effect with non-Newtonian fluid are investigated in details.

CHAPTER 3
COMPUTATIONAL MODEL AND SOLUTION

3.1 Micro Pump Geometry

The micropump consists of two cylinders of diameter *d*, placed symmetrically at the vertical position inside an extremely narrow channel of height 2*h*, where channel axis is perpendicular to cylinder axis shown in Fig. 3.1. The cylinders are horizontally placed at the middle along the channel length. The length of the channel is taken as 16 times the diameter of the cylinder to establish fully developed flow in far upstream (8d) and far downstream (8d) of the cylinder.

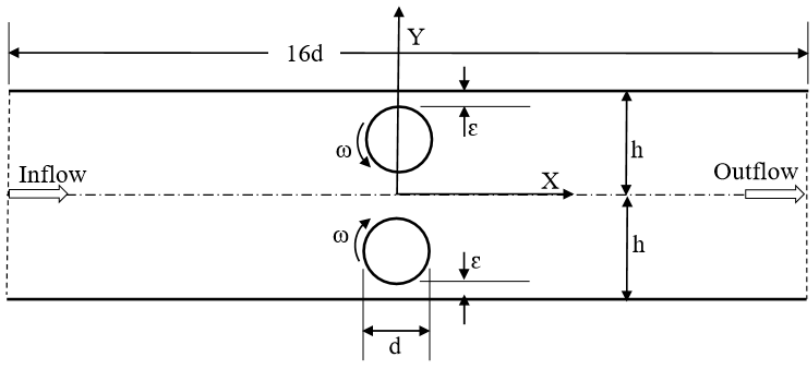

(a)

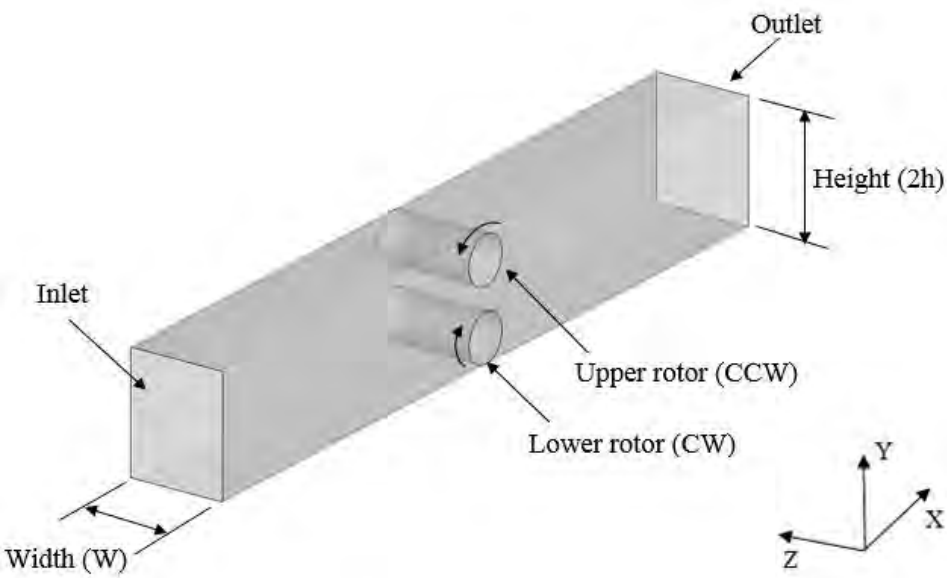

(b)

Fig. 3.1Micropump Geometry (a) 2D view (b) 3D view

The main geometric parameters in the present study are the channel height *2h,* channel width W and the wall clearance ε, which indicates the position of the rotor inside the channel.

The non-dimensional channel height is defined as: $H^* = \frac{2h}{d}$ (3.1)

The non-dimensional channel width is defined as: $W^* = \frac{W}{d}$ (3.2)

The non-dimensional wall clearance is defined as: $\varepsilon^* = \frac{\varepsilon}{d}$ (3.3)

The clearance, ε is the only parameter that identifies the position of the rotor. When ε = 0, cylinder is in contact with either upper or lower channel wall. When ε >0, the cylinder is away from the channel wall.

The cylinder rotates with an angular velocity inside the channel. Reynolds number is imposed to characterize the angular speed of the cylinder. The Reynolds number is defined as:

$$\mathrm{Re} = \frac{Ud}{\upsilon} = \frac{\omega d^2}{2\upsilon} \tag{3.4}$$

Where, U is the tangential velocity of the cylinder, ω is the angular speed of the cylinder and ν is the kinematic viscosity of the fluid

The non-dimensional average velocity inside the channel, $U^* = \frac{U_{avg}}{U}$ (3.5)

Where, the average velocity U_{avg} at the cylinder outlet section is defined as

$$U_{avg} = \frac{1}{2h}\int_{-h}^{+h} U(y)dy \tag{3.6}$$

Where, U(y) is the local velocity along the y direction at channel outlet.

The scale used to non-dimensionalize the time in the simulation was chosen to be the time taken by the rotor to finish one complete revolution:

$$t^* = \frac{t}{\frac{2\pi}{\omega}} = \frac{t\omega}{2\pi} \tag{3.7}$$

The load on the pump section is characterized by a back pressure. A high pressure is set at outlet to simulate the pump load. The back pressure is non-dimensionalized with respect to a quantity that is not dependent on the pump rotation. The dimensionless pump load can be derived from the Buckingham PI theorem (Appendix-C) in the following form,

$$P^* = \frac{P_{out} - P_{in}}{\rho \nu^2 / d^2} \tag{3.8}$$

Where, ρ is the density of fluid, ν is the kinematic viscosity of the fluid andP_{in}& P_{out} are channel input and output pressure respectively.

Similarly, the non-dimensional shear stress on the rotor surface can be expressed as

$$\tau^* = \frac{\tau}{\rho U^2} \tag{3.9}$$

Where, τ is wall shear stress around the cylinder and U is the rotor tangential velocity.

The non-dimensionalize driving power (detail derivation shown in Appendix-C) can be defined as

$$T^* = \frac{(M\omega)\,\mathrm{Re}}{\rho U^3 d^2} \tag{3.10}$$

Where, M is the total moment on the cylinders which is measured by using the following equation,

$$M = 2\left(\frac{d}{2}\int_{rotor} \tau ds\right) \tag{3.11}$$

Where, τ is wall shear stress around the cylinder and ds is the differential element of the rotor surface.

The efficiency is defined as the ratio of the flow energy rise to the driving power.

Flow energy rise = Flow rate × Pressure rise

$$= \frac{m}{\rho} \times \Delta P$$

Driving power = Torque × Rotor angular speed

$$= M \times \omega$$

Therefore, the micropump efficiency may be obtained from,

$$\eta = \frac{\frac{m}{\rho}\Delta P}{M\omega} \tag{3.12}$$

The dimensionless coordinates used in this study are:

$$(X,Y,Z)^* = \frac{(X,Y,Z)}{d} \tag{3.13}$$

The drag and moment coefficients on rotor surface are defined as,

$$C_D = \frac{F_D}{\frac{1}{2}\rho U^2 d} \tag{3.14}$$

$$C_M = \frac{M}{\frac{1}{2}\rho U^2 d^2} \tag{3.15}$$

3.2 Governing Equations

The flow in this study is considered to be incompressible, viscous, laminar and unsteady. Governing equations for the present system are the conservation of mass and conservation of momentum, can be written in the following form:

$$\frac{1}{\rho}\frac{\partial \rho}{\partial t} + \frac{\partial(u)}{\partial x} + \frac{\partial(v)}{\partial y} + \frac{\partial(w)}{\partial z} = 0 \tag{3.16}$$

$$\rho\left(\frac{\partial(u)}{\partial t} + u\frac{\partial(u)}{\partial x} + v\frac{\partial(u)}{\partial y} + w\frac{\partial(u)}{\partial z}\right) + \frac{\partial(p)}{\partial x} = \mu\left(\frac{\partial^2 u}{\partial x^2} + \frac{\partial^2 u}{\partial y^2} + \frac{\partial^2 u}{\partial z^2}\right) \tag{3.17}$$

$$\rho\left(\frac{\partial(v)}{\partial t} + u\frac{\partial(v)}{\partial x} + v\frac{\partial(v)}{\partial y} + w\frac{\partial(v)}{\partial z}\right) + \frac{\partial(p)}{\partial y} = \mu\left(\frac{\partial^2 v}{\partial x^2} + \frac{\partial^2 v}{\partial y^2} + \frac{\partial^2 v}{\partial z^2}\right) \tag{3.18}$$

$$\rho\left(\frac{\partial(w)}{\partial t} + u\frac{\partial(w)}{\partial x} + v\frac{\partial(w)}{\partial y} + w\frac{\partial(w)}{\partial z}\right) + \frac{\partial(p)}{\partial z} = \mu\left(\frac{\partial^2 w}{\partial x^2} + \frac{\partial^2 w}{\partial y^2} + \frac{\partial^2 w}{\partial z^2}\right) \tag{3.19}$$

3.3 Fluid Property

In the present study, micropump flow analysis is carried out for both Newtonian and non-Newtonian fluids. For Newtonian fluid, we have taken glycerin as the working fluid, whose density (ρ)is 1260 kg/m^3 and viscosity (μ)is 1.10 kg/m-s (1100 cP) [18]. For, non-Newtonian fluid, a power law model is used to characterize the fluid property.

3.4 Flow Conditions

The flow inside the viscous micropump was considered to be:

- Three dimensional flow
- Incompressible flow
- Laminar flow
- Unsteady flow

3.5 Boundary Conditions

Inlet: Pressure inlet boundary condition is used. Total pressure for an incompressible fluid is defined as:

$$P = P_s + 1/2\ \rho|U_{avg}|^2 \tag{3.20}$$

The inlet pressure was kept always zero, $P_{in} = 0$ (gage pressure)

Outlet: Pressure outlet boundary condition is used.

P_{out} = Gage pressure that varies depending on pump load

Non dimensional pump load, $P^* = \dfrac{P_{out} - P_{in}}{\dfrac{\rho \upsilon^2}{d^2}}$

Channel Wall:

- No slip condition
- Stationary wall

Cylinder Wall:

- No slip condition
- Moving wall (Rotational)
- Rotational speed, ω (rad/s)

3.6 Solution Method

The CFD package ANSYS fluent 14.5 [47] is used to solve the problem. The importance and use of CFD is detail explained in Appendix-B. The Piso-Simple algorithm(Appendix-B), PISO standing for Pressure-Implicit with Splitting of Operators, was used for the pressure-velocity coupling. It is nearly the same as the SIMPLE algorithm, except that it takes into account two additional corrections which are neighbor correction and skewness correction. The use of PISO allows for a rapid rate of convergence without any significant loss of accuracy rendering it more suitable for transient applications. Two different discretization schemes were used for the time and momentum equations. A power law scheme was used for the momentum equation while a second order discretization scheme was used for the time derivatives. To ensure convergence, under-relaxation was used during the solution with the under-relaxation factors varying between 0.15 to 1. Other schemes (linear or second-order schemes) lead to strong divergence or to slow convergence. The results are obtained at time step size 0.0001s and the solver iterated the equations until the scaled residuals were less than 10^{-5} or it was stabilized at a constant value. This time step size ($\Delta t = 0.0001$s) is small enough to recognize all the changes in the flow field over time and in addition, is large enough to obtain reasonable computation time.In addition, the computation time depends on the mesh refinement as well as on the RAM and system configuration used to run the process. However, the computational time required for different cases is shown in Table 3.1.

Table 3.1Computational time (Transient simulation)
(System configuration: 64 bit operating system, CPU 3.0 GHz, RAM 8 GB)

Case	Number of Cells	Approx. Computational time (hour)
H*=2.1, ε* = 0.01, W*= 20, Re=1.0, P*=1.0	422000	13.00
H*=2.5, ε* = 0.05, W*= 1.0, Re=1.0, P*=1.0	22350	1.00
H*=2.5, ε* = 0.05, W*= 10, Re=1.0, P*=1.0	223500	9.00
H*=2.5, ε* = 0.05, W*= 20, Re=1.0, P*=1.0	474000	18.00
H*=3.0, ε* = 0.05, W*= 20, Re=1.0, P*=1.0	751200	28.00

3.7 Grid Independency Test

Grid convergence is used to analyse the improvement of results by using successively smaller cell sizes for the calculations. If the mesh is finer, the calculation converges to the correct solution. That's why, grid convergence is important in computation. But for finer grids, the number of cell increases. So the calculation becomes lengthy. To avoid this drawback, a CFD technique is used to start with a coarse mesh and gradually refine it until the variation found in the results is smaller than a pre-defined acceptable error. This approach is called grid-independency test. Numerical results are greatly influenced by mesh generation. Hence, mesh generation is important in this regard. A parameter named 'minimum orthogonal quality' represents the mesh quality. The value of 'minimum orthogonal quality' ranges from 0 to 1. The mesh becomes better as this value approaches 1. Grid independency test is performed to optimize the number of elements to discretize the computational domain. Extensive tests are carried out with different sizes of mesh number.

GAMBIT software is used as mesh generator for creation of two-dimensional and three-dimensional meshes. For 2-D case, mesh is created on the side wall of pump house. The nodal points on channel wall and cylinders wall are distributed in such way so that the whole domain can be subdivided into quadrilateral elements. The region where the gradient of field variables is higher, the nodal points are kept densed (near the cylinder surface and small gap between cylinder and channel wall) and for smaller gradients (at inlet and outlet region), the nodal points are kept sparsed. Once the 2-D mesh of the pump side wall is specified, the 3-D mesh is created by projection of 2-D mesh in the z-axis, resulting in a regular mesh in span wise direction. As example, Different sizes of structured 2-D mesh are shown in Fig. 3.2.

Grid independency test is assured for both 2-D and 3-D casesby observing three parameters:steady state velocity at outlet, velocity x-component and C_D or C_M value on rotor.

Table 3.2Properties of different grids used and comparison of results
[H*=2.5, ε* = 0.025, Re=1.0, P*=10]

Mesh (2-D)	Number of Cells	***U****	Relative difference
Mesh 1	2140	0.126198	------
Mesh 2 (used)	2952	0.126939	< 0.59%
Mesh 3	4450	0.127122	< 0.15%
Mesh 4	6000	0.127098	< -0.019%

In Table 3.2, the grid independency for particular case of pump configuration is shown. The relative difference between mesh 1 and mesh 2 is 0.59% and the difference between mesh 2 and mesh 3 is 0.15%. However, mesh 2 is used for the present study, because there is no significant variation in U* for higher sizes of mesh. Moreover, x-velocity component at particular section and Drag coefficient with time for different sizes are shown in Fig. 3.3, which also justify that the grid independency is achieved at mesh 2.

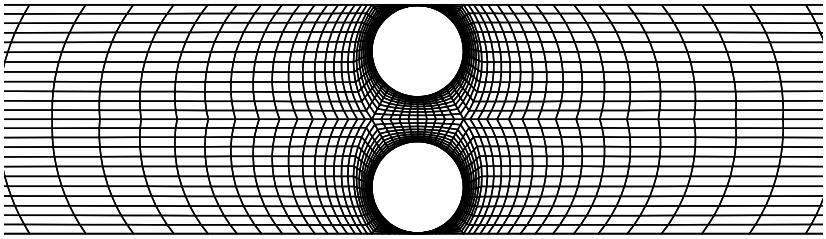

(a) Mesh1(2140 cells)

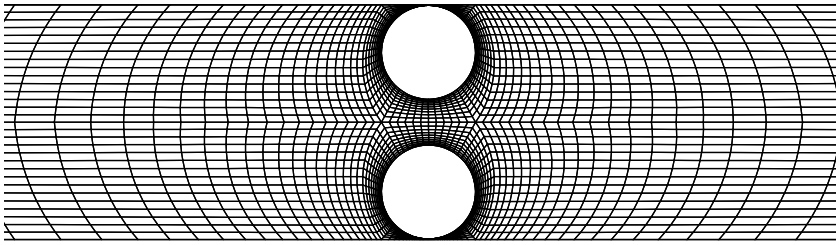

(b) Mesh2 (2952 cells)

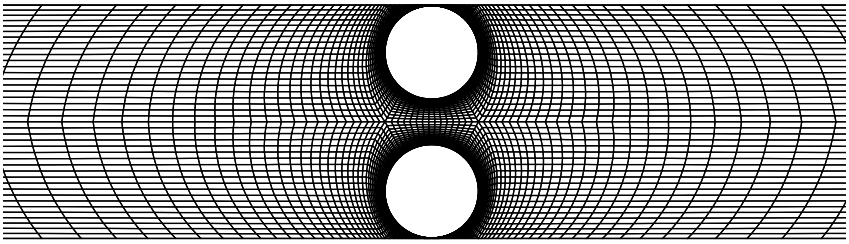

(c) Mesh3 (4450 cells)

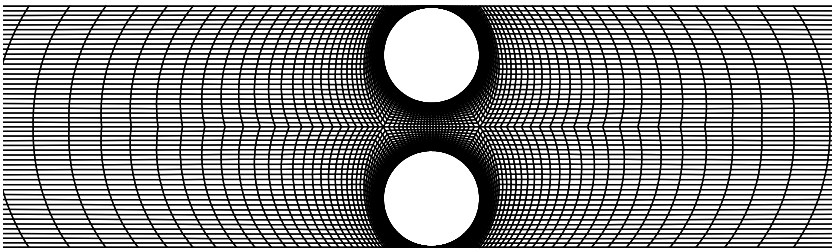

(d) Mesh 4 (6000 cells)

Fig. 3.2Different meshes (2-D) used for grid independency test

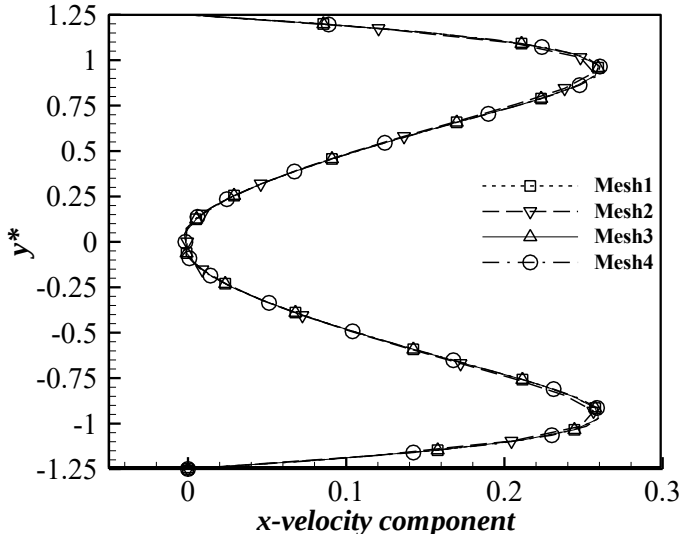

(a)

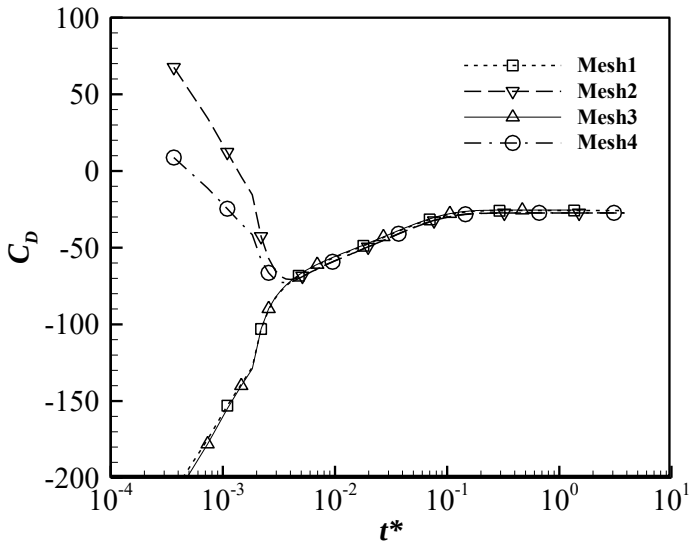

(b)

Fig. 3.3(a)Variation of velocity (x-component) on a vertical plane away 1d from cylinder vertical axis at downstream side (b) Variaion of Drag coefficent (C_D) with time [H*=2.5, ε=0.025, ΔP*=10, Re=1.0]

Table 3.3Properties of different grids used and comparison of results
[H*=2.5, ε* = 0.025, W*=20, Re=1.0, P*=10]

Mesh (3-D)	Number of Cells	U*	Relative difference
Mesh 1	14760	0.0635819	------
Mesh 2 (used)	29520	0.0610460	< 4%
Mesh 3	44280	0.0610303	< 0.026%
Mesh 4	88560	0.0610606	< -0.05%

In Table 3.3, the effect mesh sizes on the average velocity (U*) is shown. The relative difference between mesh 1 and mesh 2 is around 4%, but the difference between mesh 2 and mesh 3 is around 0.026%. Therefore, the size of mesh 2 is used as a reference for meshing of other pump configurations. Moreover, x velocity component at particular section, average velocity with time, Drag and Moment coefficient time for different mesh sizes are shown in Fig. 3.4-Fig. 3.6, which also justify that the grid independency is achieved at mesh 2.

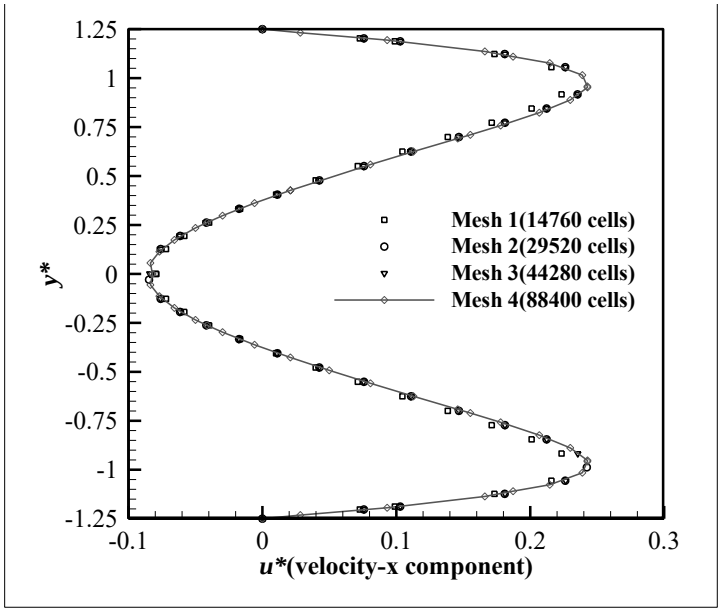

Fig. 3.4 Velocity x-component profile at X*=1.0, Z*=0 (symmetric plane) of dual rotor pump [H*=2.5, ε*=0.025,W*=1.0, P*=10, Re=1.0]

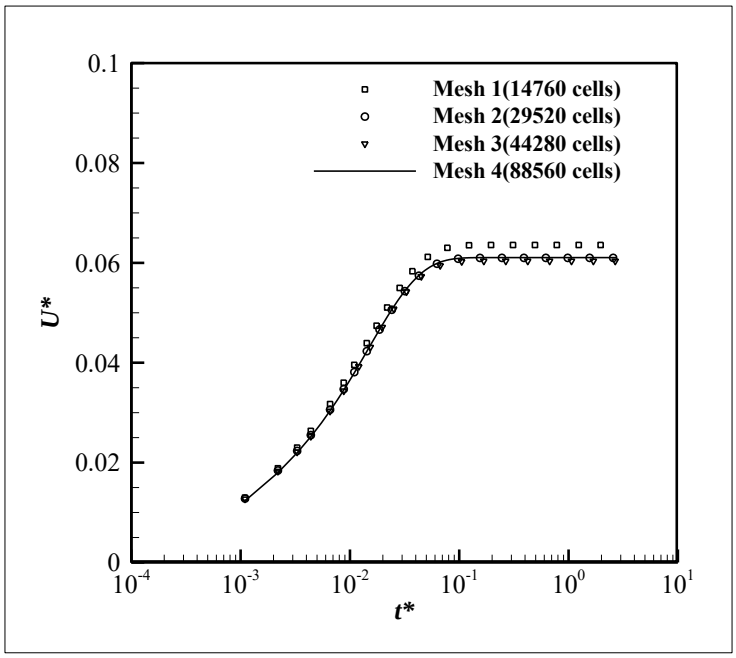

Fig.3.5Average velocity at outlet with time of dual rotor pump [H*=2.5, ε*=0.025,W*=1.0, P*=10, Re=1.0]

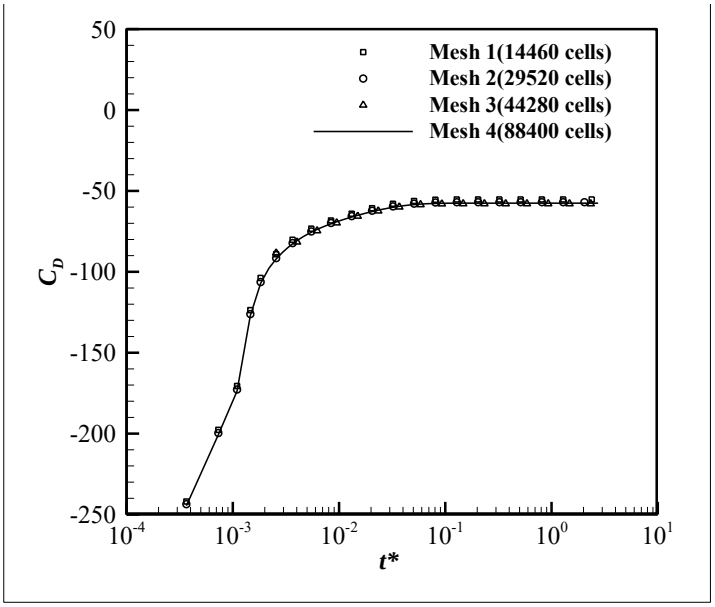

(a)

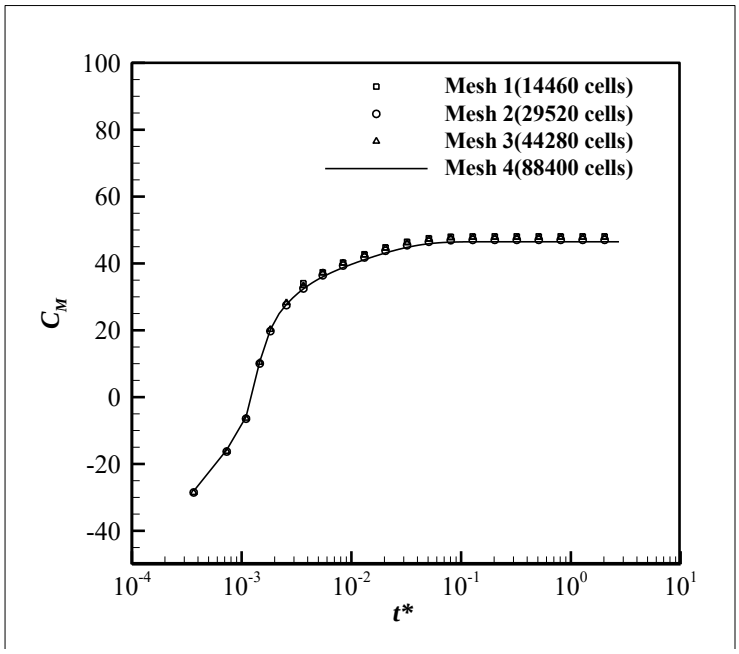

(b)

Fig. 3.6 (a) Drag coefficient, C_D with time (b) Moment coefficient, C_M with time on lower rotor of dual rotor pump([H*=2.5, ε*=0.025, W*=1, P*=10, Re=1.0]

4.8 Validation

To validate the computational method, we simulate the single cylinder micropump, which has been experimentally studied by Sen et. al.[18]. The corresponding condition is ε*=0.025, W*=16.93, Re=0.5, P*=0.5. Fig. 3.7 compares the non-dimensional average velocity with the experimental data which show that the results are in good agreement. Besides, velocity profile on vertical line at symmetric plane (Z*=0) and average velocity with cylinder speed are presented in Fig. 3.8 and Fig. 3.9 respectively for proper justification of the present numerical method.

However, an acceptable overall agreement between experimental and numerical results is achieved throughout the range of H* considered. The validated computational model is then employed to investigate the flow dynamic behaviour of a dual rotor micro-scale viscous pump in case of Newtonian fluid.

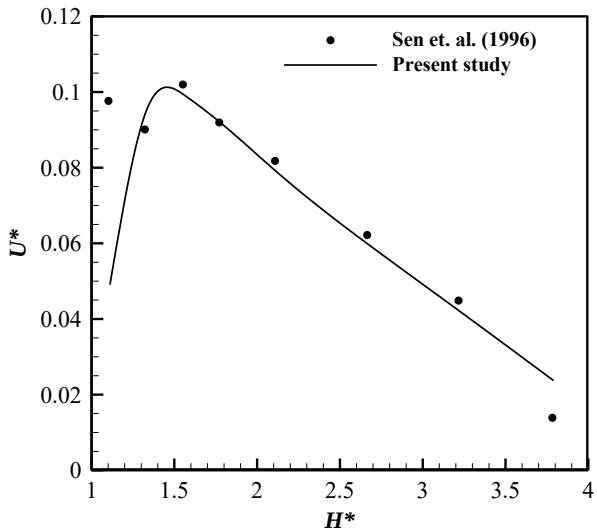

Fig. 3.7Variation of average velocity with channel height. [ε*=0.025, W*=16.93, Re=0.5, P*=0.5]

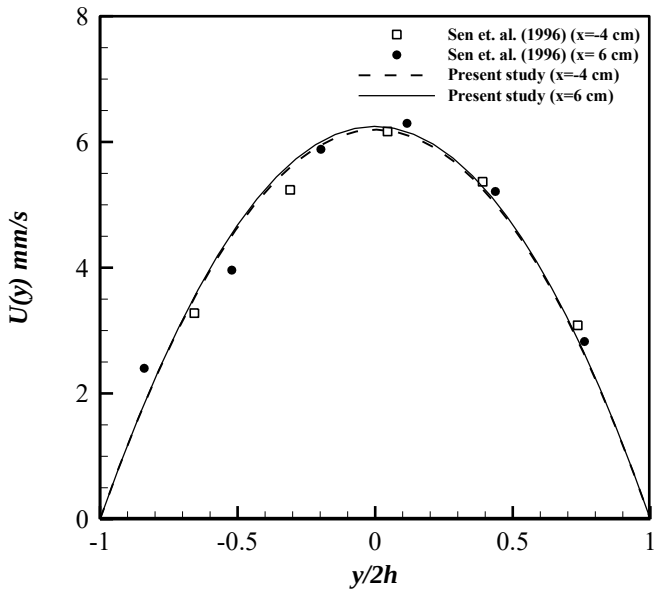

Fig. 3.8 Velocity profiles at different sections along x axis. [H*=1.56, W*=16.93, ε*=0.025, Re=0.5, P*=0.5]

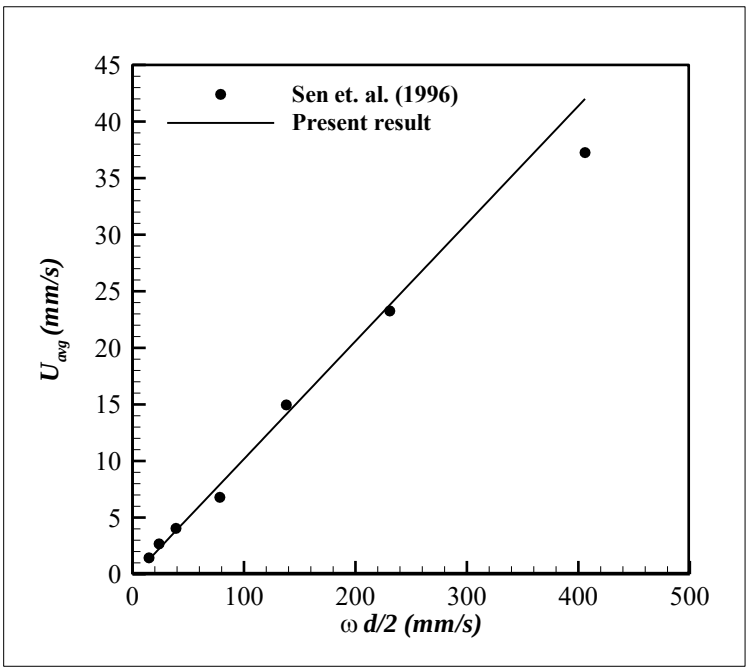

Fig. 3.9Variation of channel average velocity as a function of cylinder tangential velocity [H*=1.56, W*=16.93, ε*=0.025, P*=0.5]

The flow pattern development with time inside the micropump shown in Fig. 3.10 is compared at same operating condition with the result of Abdelgawad et. al. [31] for further validation of the present study.

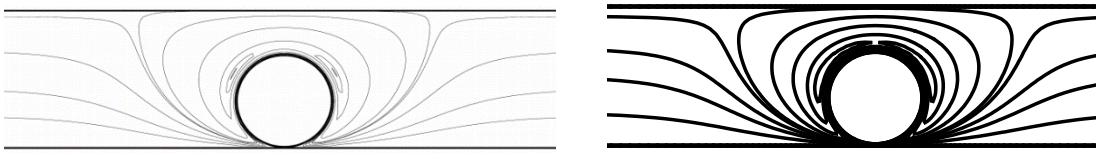

(a) (b)

t^*=0.00048

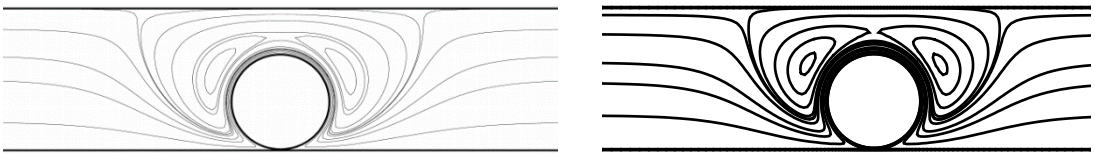

(c) (d)

t^*=0.0048

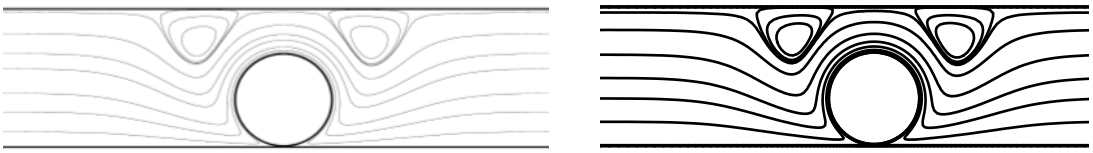

(e) (f)

t*= Steady State

Abdelgawad et al. (2004) [31] Present Computation

Fig. 3.10Flow pattern (a), (c), (e) are obtained at H*= 2.5, ε*= 0.0125, Re=1.0, P*=0 from Abdelgawad et al. (2004) for 2-D case and the flow pattern (b), (d), (f) from the present study.

CHAPTER 4
RESULTS AND DISCUSSION

As previously stated, the objectives of the present study is to investigate the flow dynamic behavior of a dual rotor micro-scale viscous pump, to analyze the effect of geometric configurations (i.e., channel height H*, wall clearance ε* and channel width W*), Reynolds numberand pump load on the pump flow performance for the both cases of Newtonian and non-Newtonian fluids, and to study the initial transient nature of the flow field inside the micro pump.

4.1 Steady Flow Visualization

4.1.1 Streamlines

Streamlines give a good qualitative picture of the flow patterns.Fig. 4.1-Fig. 4.5 show the effect of change in wall clearance on the streamlines at different channel heights and at the same flow conditions i.e. Re=1.0 and P*=1.0. In all cases, the flow patterns are symmetrical about the centerline of the micro-pump channel. Results for channel height of H*=2.1 and H*=2.3 are shown in Fig. 4.1 and Fig. 4.2 respectively where four vortices, of them two at upstream side and the other two at downstream side are observed. The size of the flow vortices for both cases (H*=2.1 and H*=2.3) increase with wall clearance ε*. This is due to the narrow gap (effective flow area) between the two cylinders which becomes smaller with increasingε*. Therefore, it restricts the effective flow and results in larger vortices both on upstream and downstream sides.

In case of channel height H*=2.5 in Fig. 4.3, no vortex is seenat lower wall clearance, but vortices are found at higher wall clearance. Because, at higher wall clearance the phenomena of restricting the flow area is same as the case of channel height H*=2.1 and H*=2.3.

However, the flow patterns are quite same in all cases for channel height of H*=2.7 and H*=3.0which are shown in Fig. 4.4and Fig. 4.5 respectively.Here, no vortex is found throughout the channel. Rather, the flow streamlines near the bottom and upper regions bend more around the respective rotor with increasing wall clearanceε*.

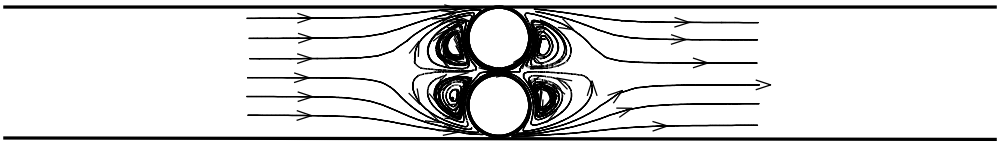

(a) ε*=0.00625

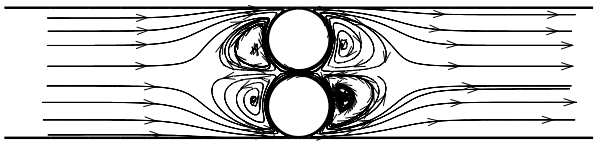

(b) ε*=0.01

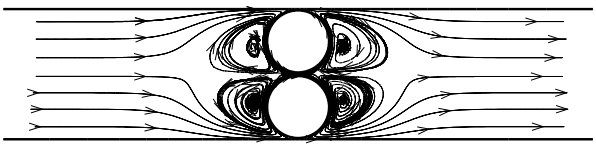

(c) ε*=0.02

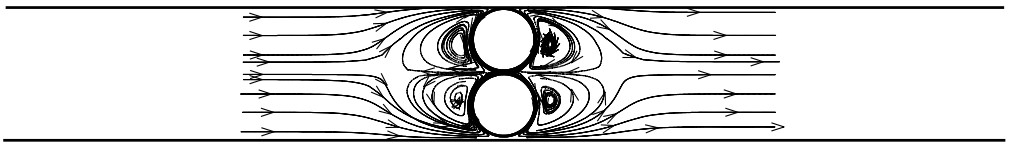

(d) ε*=0.025

Fig. 4.1Streamlines at symmetric plane (Z*=0) for **H*=2.1**, W*=20, P*=1.0, Re=1.0

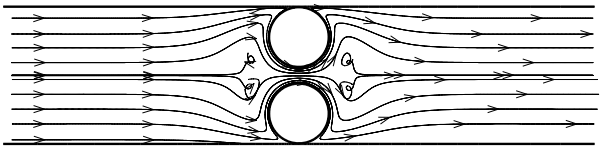

(a) ε*=0.01

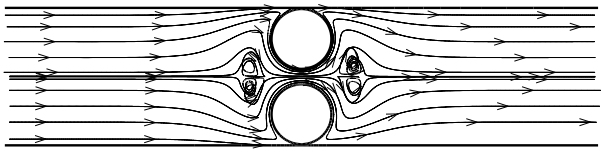

(b) ε*=0.02

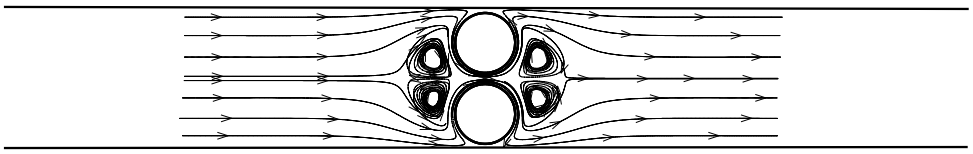

(c) ε*=0.03

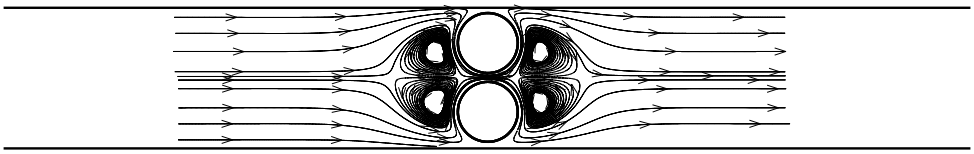

(d) ε*=0.05

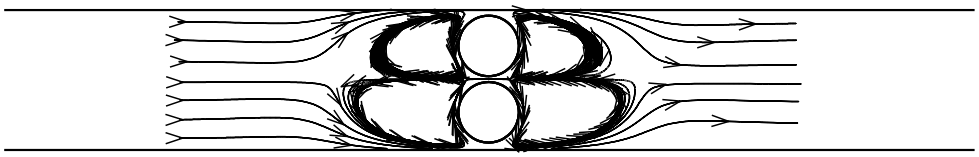

(e) ε*=0.075

Fig. 4.2 Streamlines at symmetric plane (Z*=0) for **H*=2.3**, W*=20, P*=1.0, Re=1.0

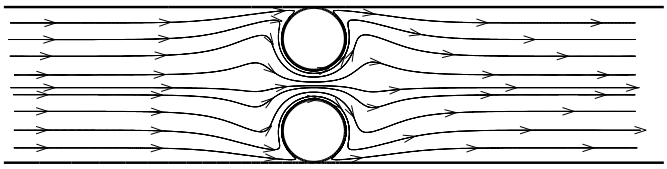

(a) ε*=0.01

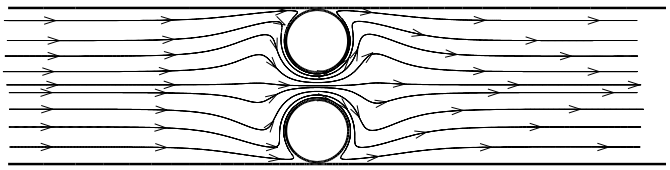

(b) ε*=0.03

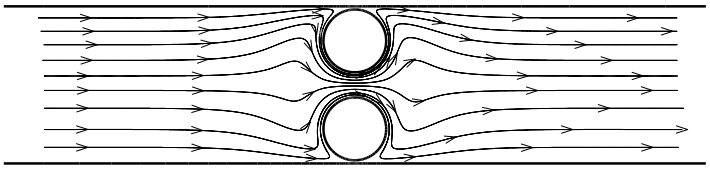

(c) ε*=0.05

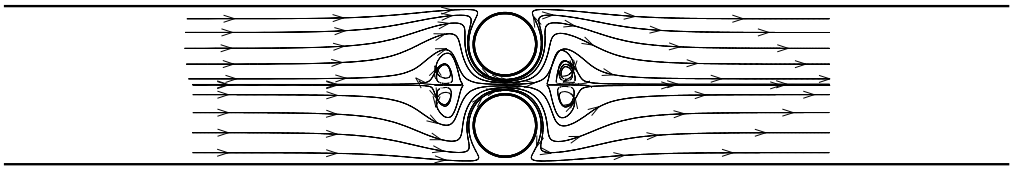

(d) ε*=0.10

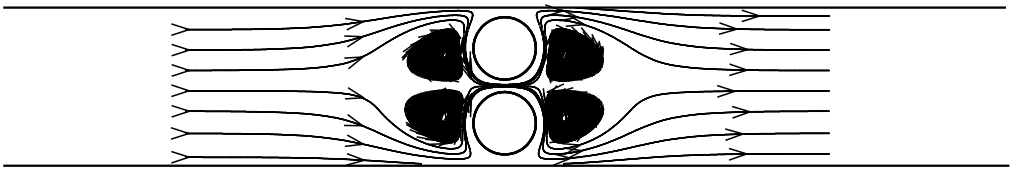

(e) ε*=0.15

Fig. 4.3 Streamlines at symmetric plane (Z*=0) for **H*=2.5**, W*=20, P*=1.0, Re=1.0

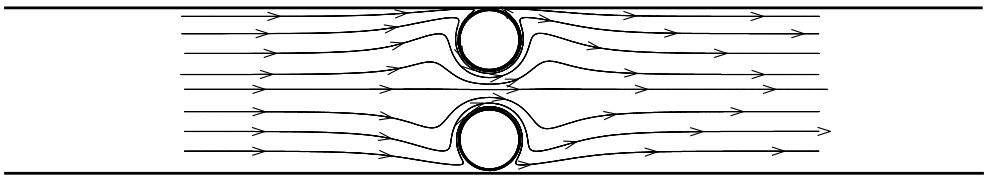

(a) ε*=0.03

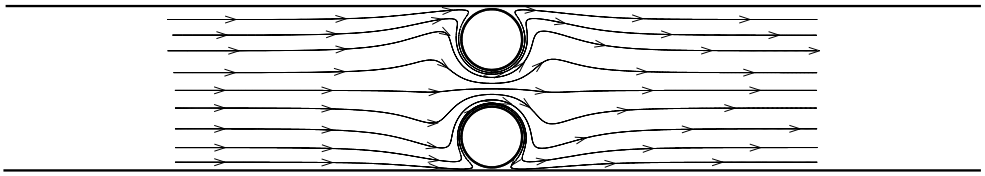

(b) ε*=0.05

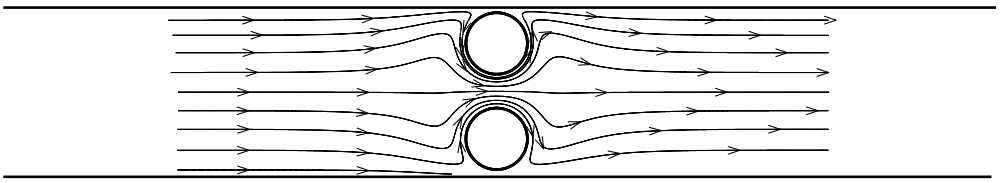

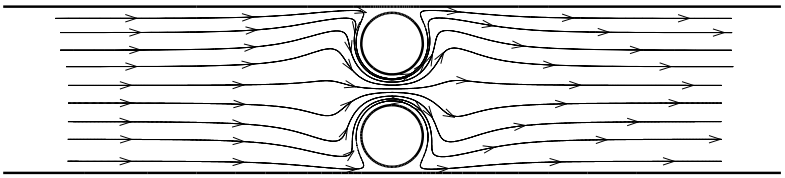

(d) ε*=0.10

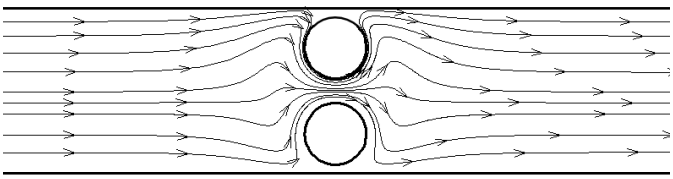

(e) ε*=0.15

Fig. 4.4 Streamlines at symmetric plane (Z*=0) for **H*=2.7**, W*=20, P*=1.0, Re=1.0

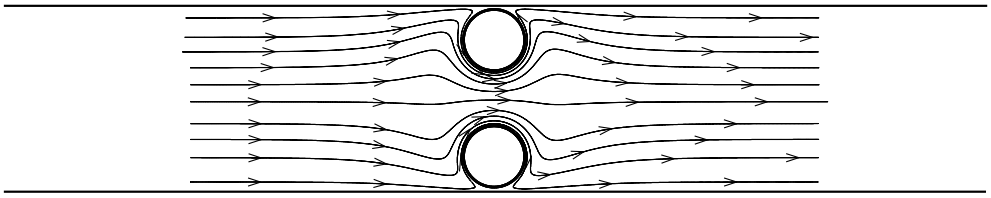

(a) ε*=0.05

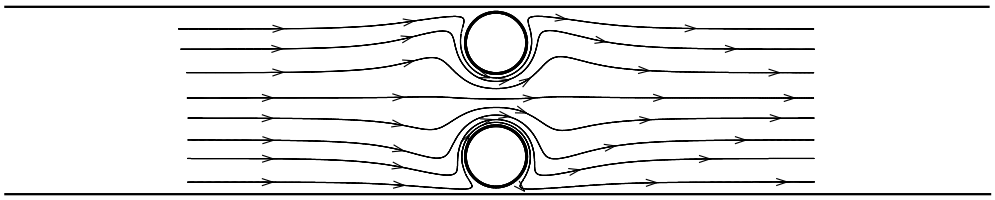

(b) ε*=0.075

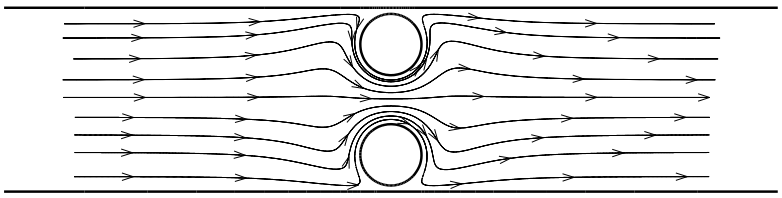

(c) ε*=0.10

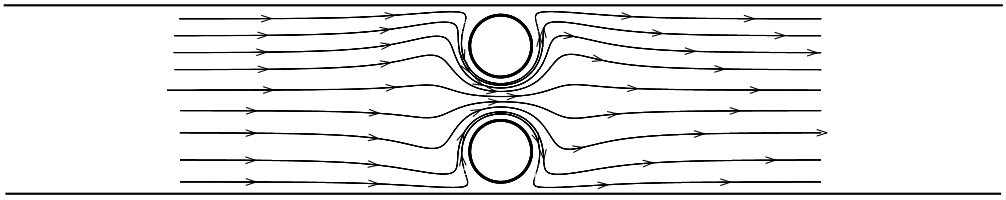

(d) ε*=0.15

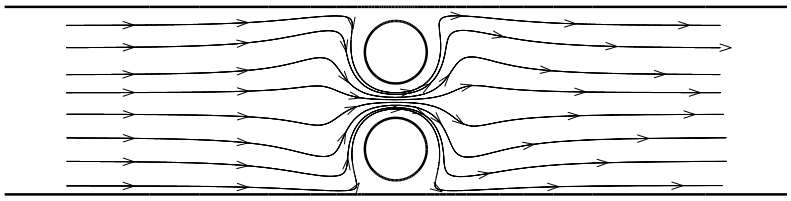

(e) ε*=0.20

Fig. 4.5 Streamlines at symmetric plane (Z*=0) for **H*=3.0**, W*=20, P*=1.0, Re=1.0

4.1.2 PressureContour

Fig. 4.6 - Fig. 4.7 show the static pressure contour at the symmetric plane inside the viscous micropump for different pump configurations. In all cases of channel height,there are two distinct zones where the difference of pressure is significantly high. The first one is the high pressure zone on the downstream below the lower cylinder surface and above the upper cylinder surface. The high pressure zone results from the presence of lower and upper channel walls, which restrict the vertical component of flow creating a semi-stagnation zone. The second location is the low pressure zone on the upstream below the lower cylinder and above the upper cylinder results from the suction created by the vertical component of flow, which directed away from the wall.

In case of channel heightof H*=2.1 in Fig. 4.6, a significant variation in pressure between rotor gap is observed. It is seen with the help of color contrast that the positive pressure lies near upstream whereas the negative pressure lies near downstream. The interesting observation is that the intensity of pressure on those locations increases with wall clearance. This is due to the effect of restricting the flow as discussed in previous section. It is also seen that the pressure intensity on the high pressure zone and the low pressure zone at different wall clearances are approximately same.

In other cases of channel height (H*=2.3, H*= 2.5, H*=2.7 and H*=3.0), which are shown in Fig. 4.7 to Fig. 4.10, the significant variation in pressure intensity on high pressure zone and low pressure zone are observed. It is found thatthe intensity of pressure in high and low pressure zone decreases with the increase of wall clearance.

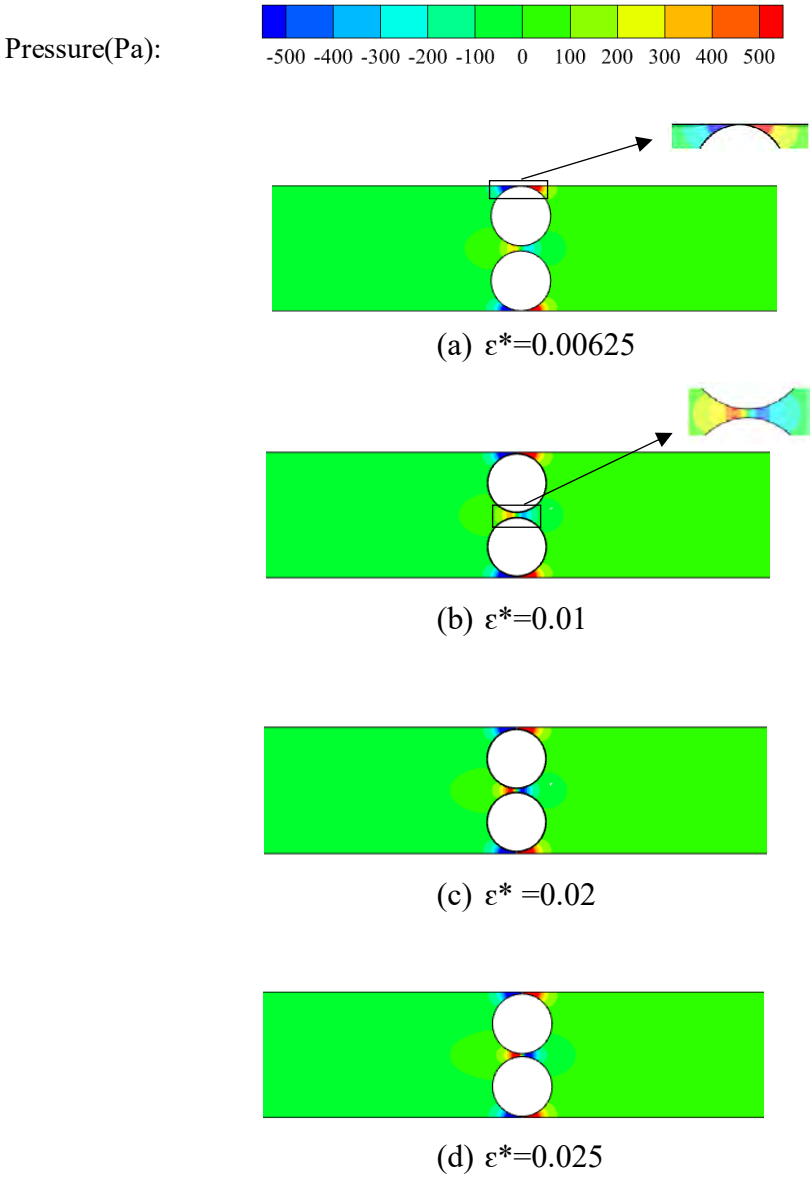

Fig. 4.6Static pressure contour at Z*=0 (symmetric plane) for **H*=2.1**, W*=20, P*=1.0, Re=1.0

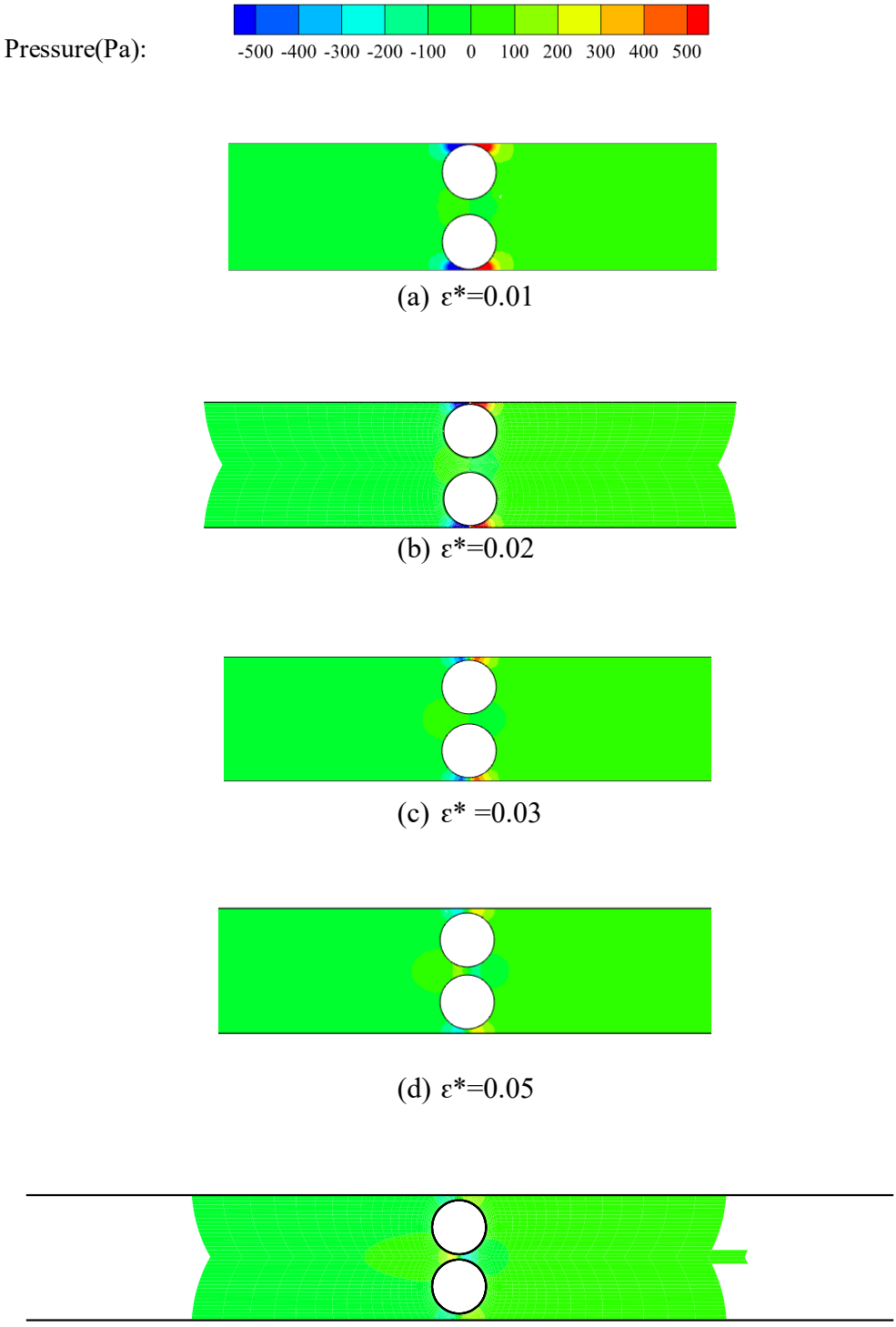

(a) ε*=0.01

(b) ε*=0.02

(c) ε* =0.03

(d) ε*=0.05

(e) ε*=0.075

Fig. 4.7 Static pressure contour at Z*=0 (symmetric plane) for **H*=2.3**, W*=20, P*=1.0, Re=1.0

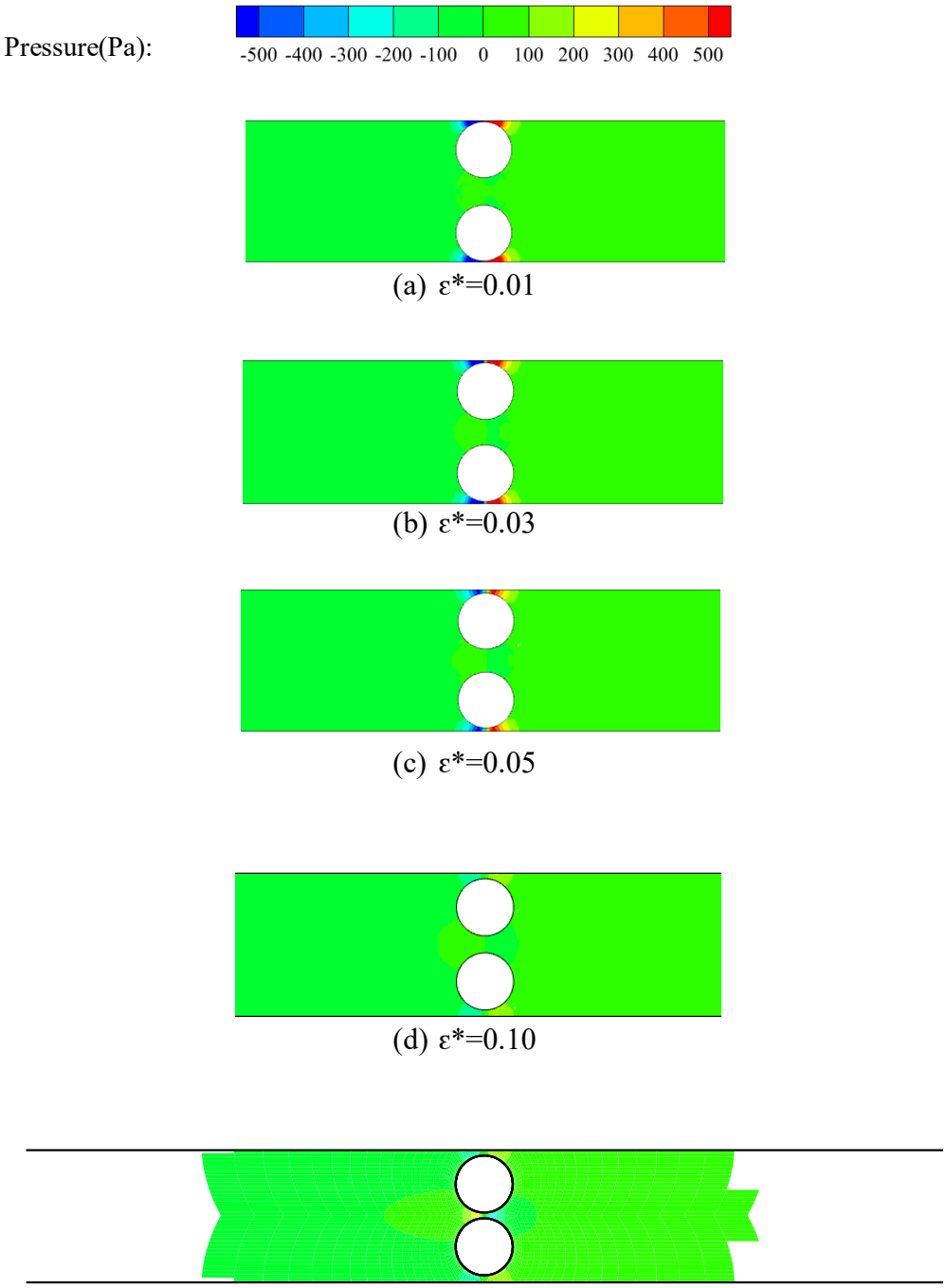

(a) ε*=0.01

(b) ε*=0.03

(c) ε*=0.05

(d) ε*=0.10

(e) ε*=0.15

Fig. 4.8 Static pressure contour at Z*=0 (symmetric plane) for **H*=2.5**, W*=20, P*=1.0, Re=1.0

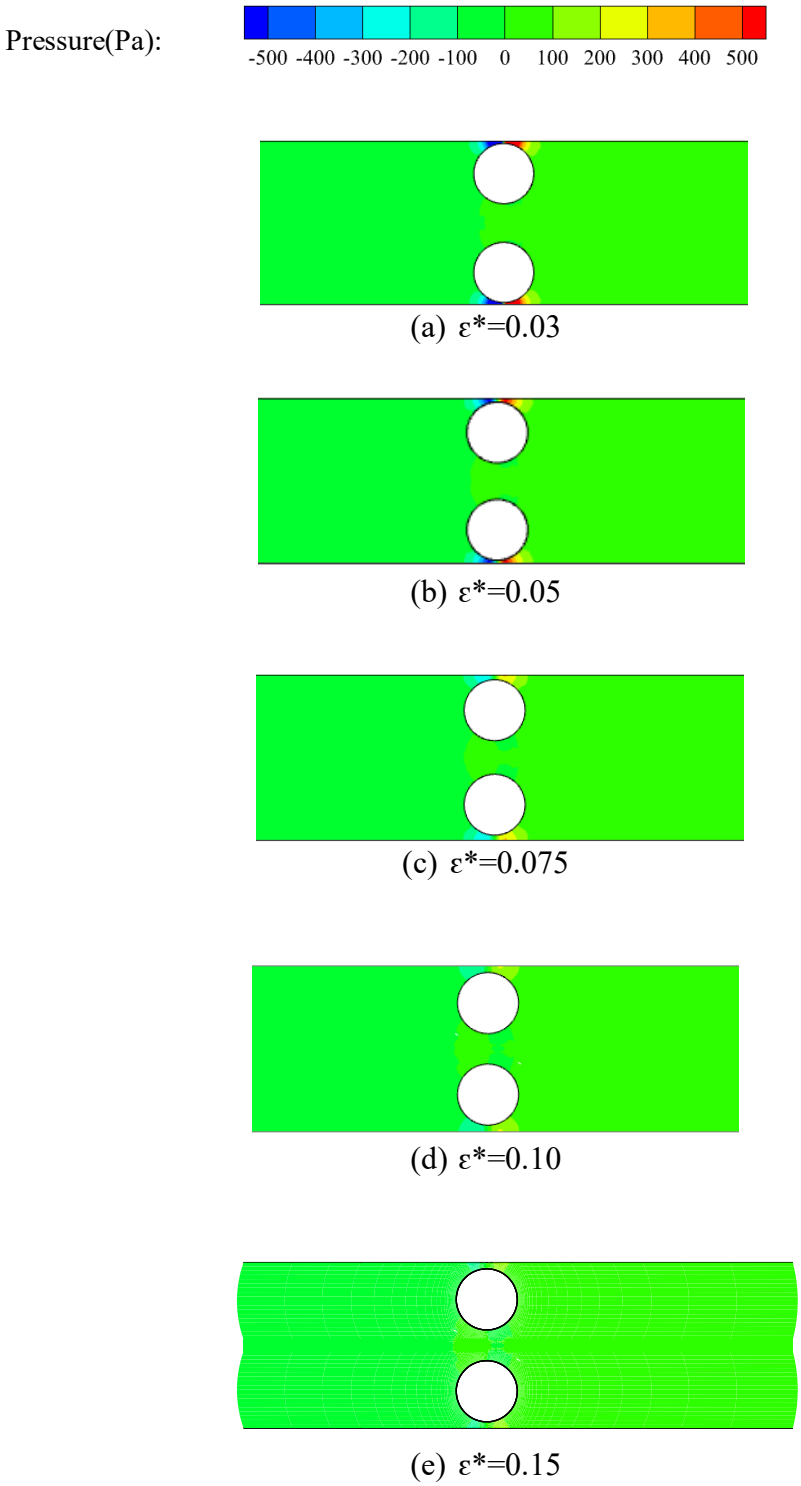

Fig. 4.9 Static pressure contour at Z*=0 (symmetric plane) for **H*=2.7**, W*=20, P*=1.0, Re=1.0

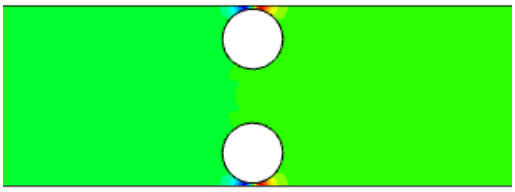

(a) ε*=0.5

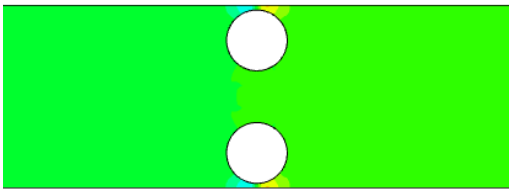

(b) ε*=.075

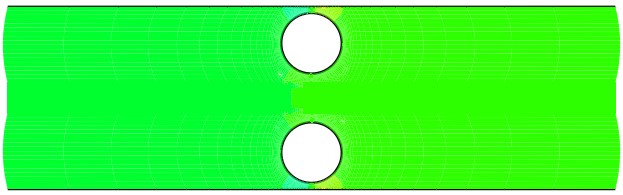

(c) ε*=0.1

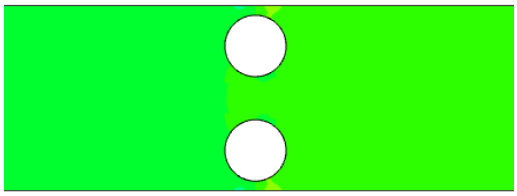

(d) ε*=0.15

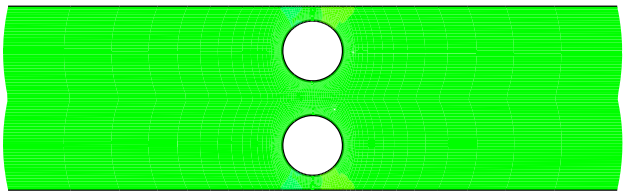

(e) ε*=0.20

Fig. 4.10 Static pressure contour at Z*=0 for **H*=3.0**, W*=20, P*=1.0, Re=1.0

4.1.3 X-VelocityContour

The velocity is one of the most important performance parameters as it quantifies the pumping effect. Fig. 4.11-Fig. 4.15 illustrate the effect of the wall clearance on the velocity contour inside the micropump. As the rotors are counter rotating i.e. the upper rotor in anti-clock-wise and the lower rotor in clockwise direction, the positive velocity exists between the gap of the two rotors and the negative velocity exists between gap of the rotor and the channel wall. According to the color contrast which are presented for all the cases, the rotors at lowwall clearance ε* provide high velocity. The main reason behind this is the higher effective flow area in lower ε*.

In case of channel height of H*=2.1 in Fig. 4.11, it is seen that the negative velocity exists near upstream and near downstream due to presence of the two counter rotating vortices in each side (Fig. 4.1). It is also seen that the area of negative velocity on both side increases with wall clearance.

Similar phenomenon as H*=2.1 are found at higher wall clearance for channel height of H*=2.3 and H*=2.5 shown in Fig. 4.12 and Fig. 4.13 respectively. No negative velocity in upstream and upstream are observed for channel height of H*=2.7 and H*=3.0 presented in Fig. 4.14 and Fig. 4.15 respectively.

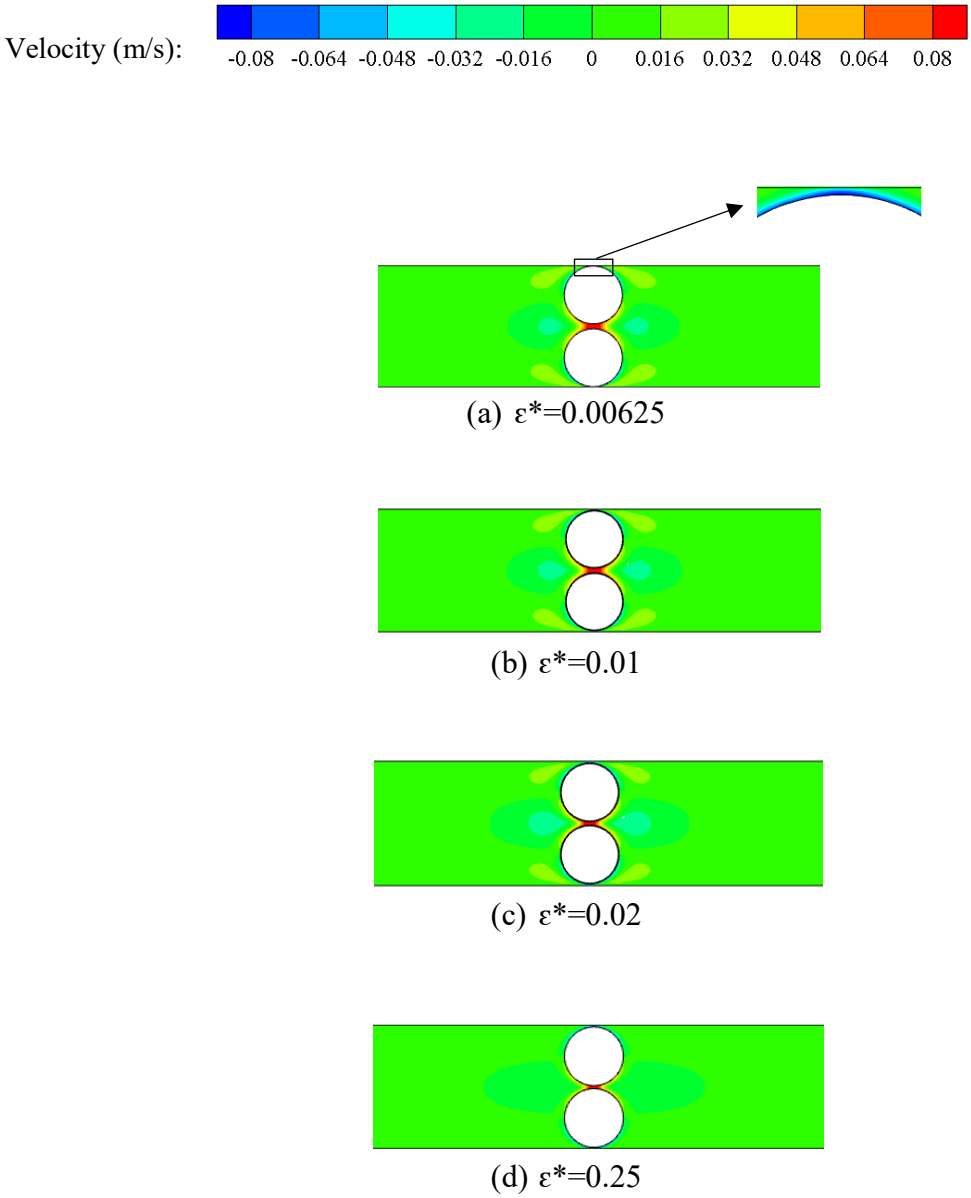

Fig. 4.11X-Velocity contour at Z*=0 (symmetric plane) for **H*=2.1**, W*=20, P*=1.0, Re=1.0

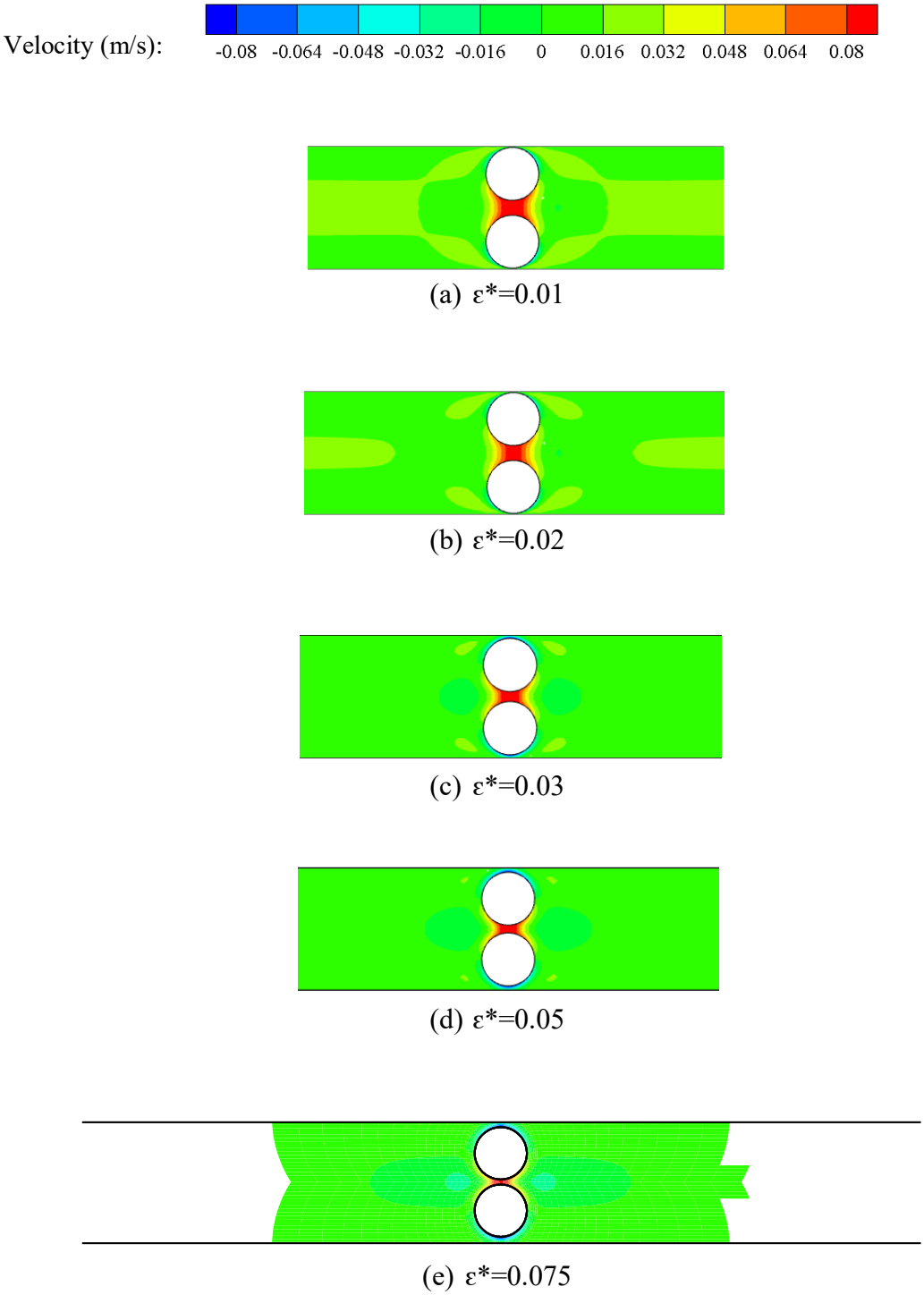

Fig. 4.12X-Velocitycontour at Z*=0 (symmetric plane) for **H*=2.3**, W*=20, P*=1.0, Re=1.0

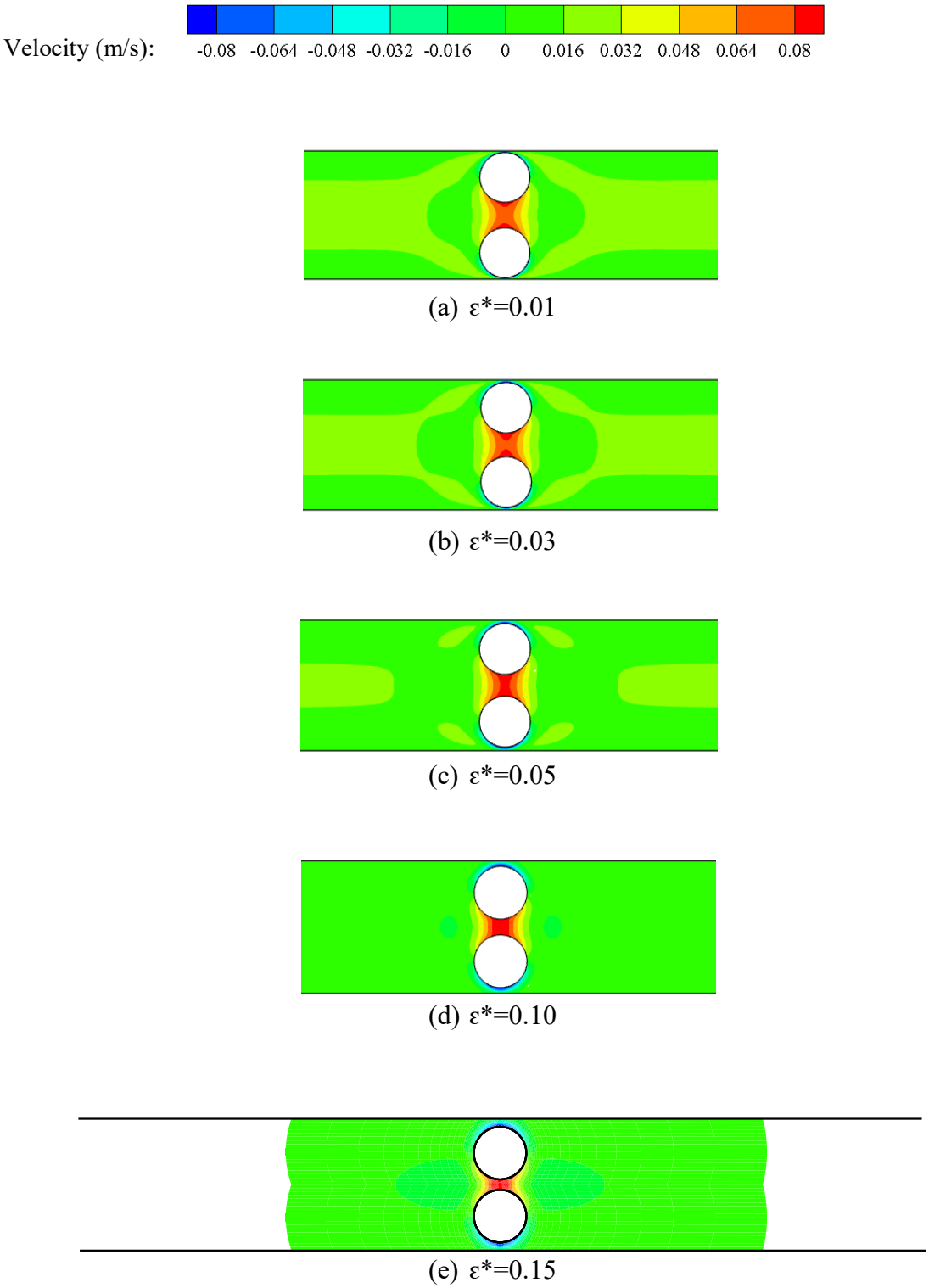

Fig. 4.13X-Velocity contour at Z*=0 (symmetric plane) for **H*=2.5**, W*=20, P*=1.0, Re=1.0

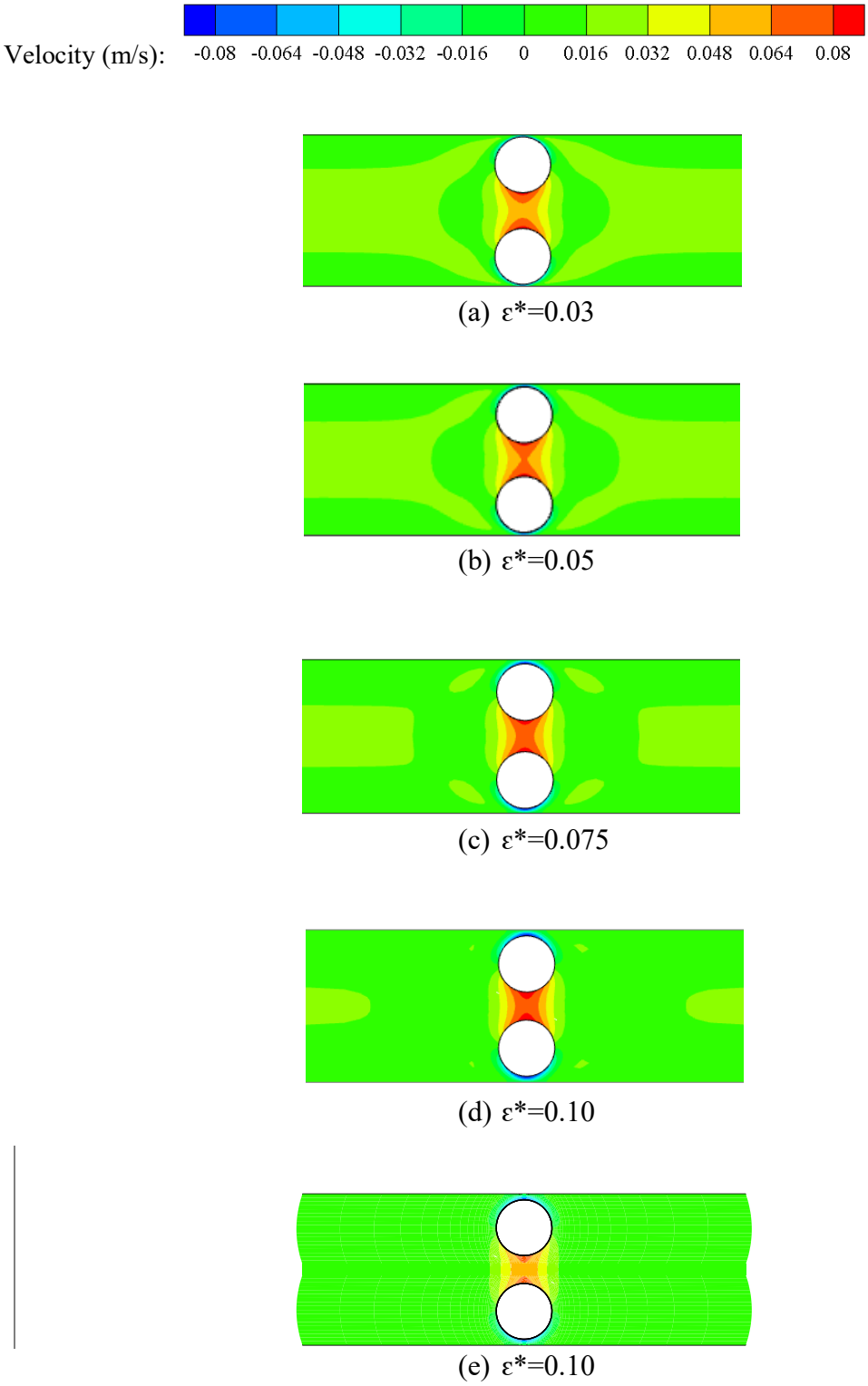

Fig. 4.14 X-Velocity contour at Z*=0 (symmetric plane) for **H*=2.7**, W*=20, P*=1.0, Re=1.0

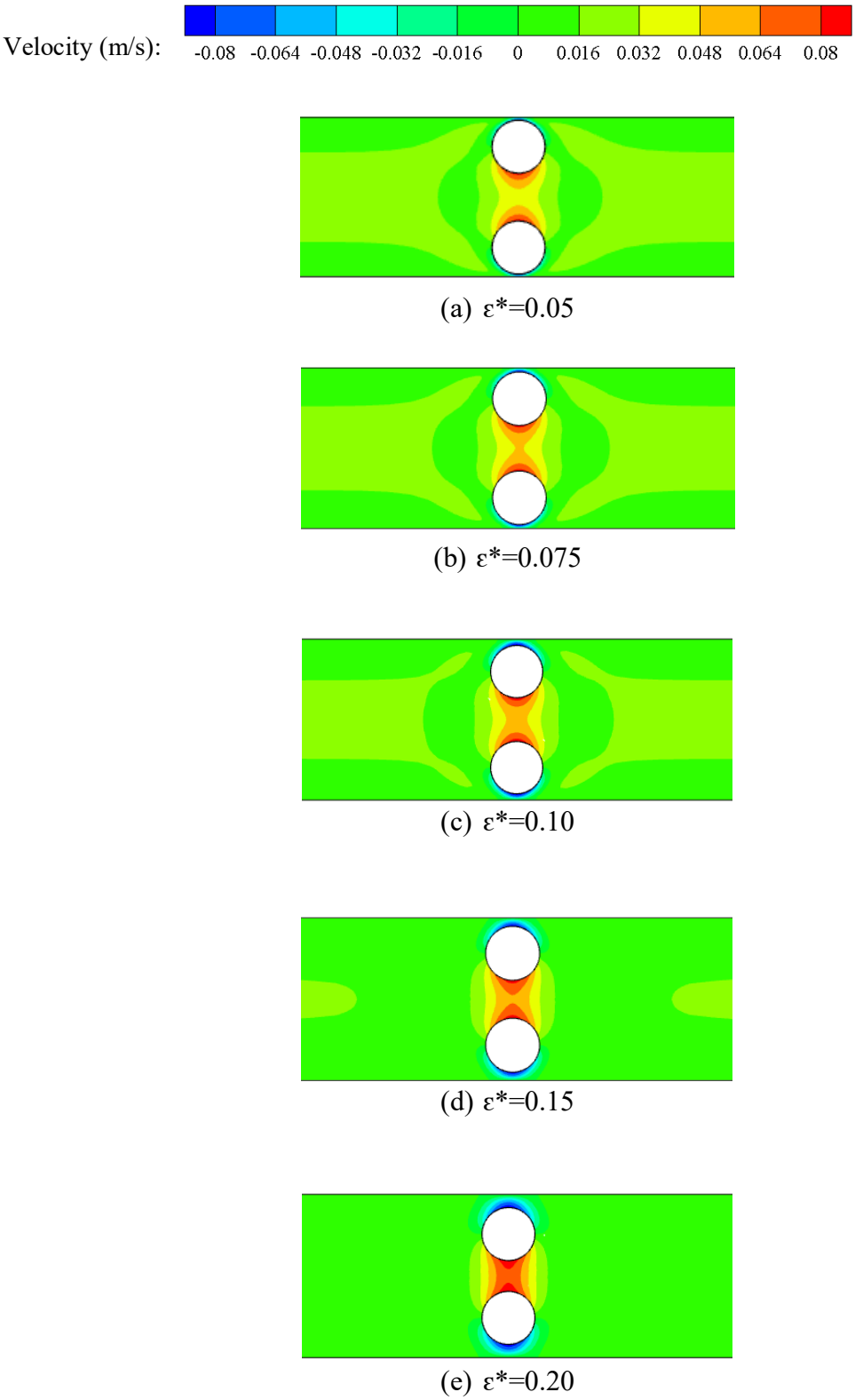

Fig. 4.15X-Velocity contour at Z*=0 (symmetric plane) for **H*=3.0**, W*=20, P*=1.0, Re=1.0

4.1.4. Wall Shear Stress Contour

The torque on the rotor is directly related to the shear stress on the surface of the rotor. The effect of wall clearance on the wall shear stress distribution around the rotors are presented in Fig. 4.16-Fig.4.20. In all cases, it shows that maximum shear stress are developed approximately at regions below the lower cylinder and above the upper cylinder. It also shows that shear stress distribution is symmetrical about the channel vertical axis.

The rotor position inside the micropump has significant influence on the magnitude of shear stress. As the channel height does not significantly affect the driving power discussed in Fig. 4.29 (b), results for shear stress distribution on rotors (Fig. 4.16-Fig.4.20) are taken for a gradual change in wall clearance at different channel heights.It is found that the shear stress intensity around the rotors for wall clearance $\varepsilon^*=0.01$ in Fig. 4.16 is comparatively higher than the $\varepsilon^*=0.02$ in Fig. 4.17, which is then comparatively higher than the next higher values of ε^* and so on shown in Fig. 4.18-Fig. 4.20. This is due to high velocity gradient from channel wall to the rotor surface, which increases with smaller wall clearance ε^*.

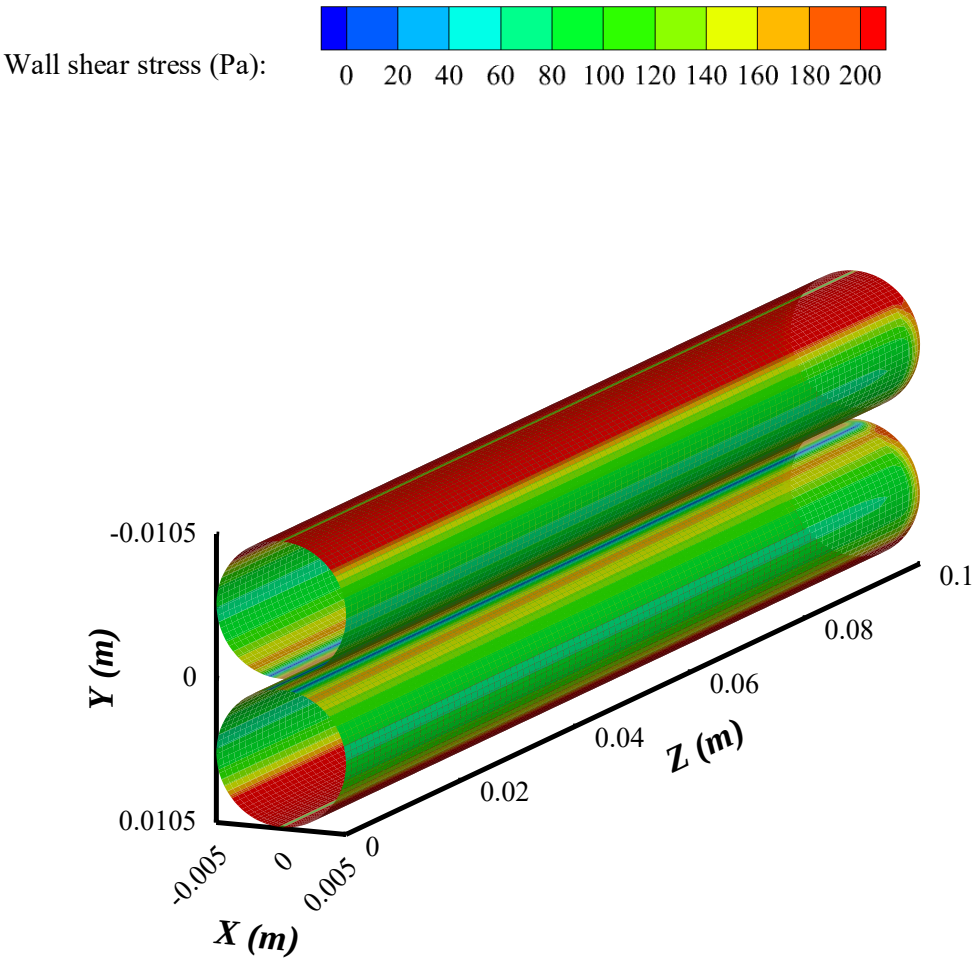

Fig. 4.16 Wall shear stress contour on cylinders for H*=2.1, ε*=0.01, W*=20, P*=1.0, Re=1.0

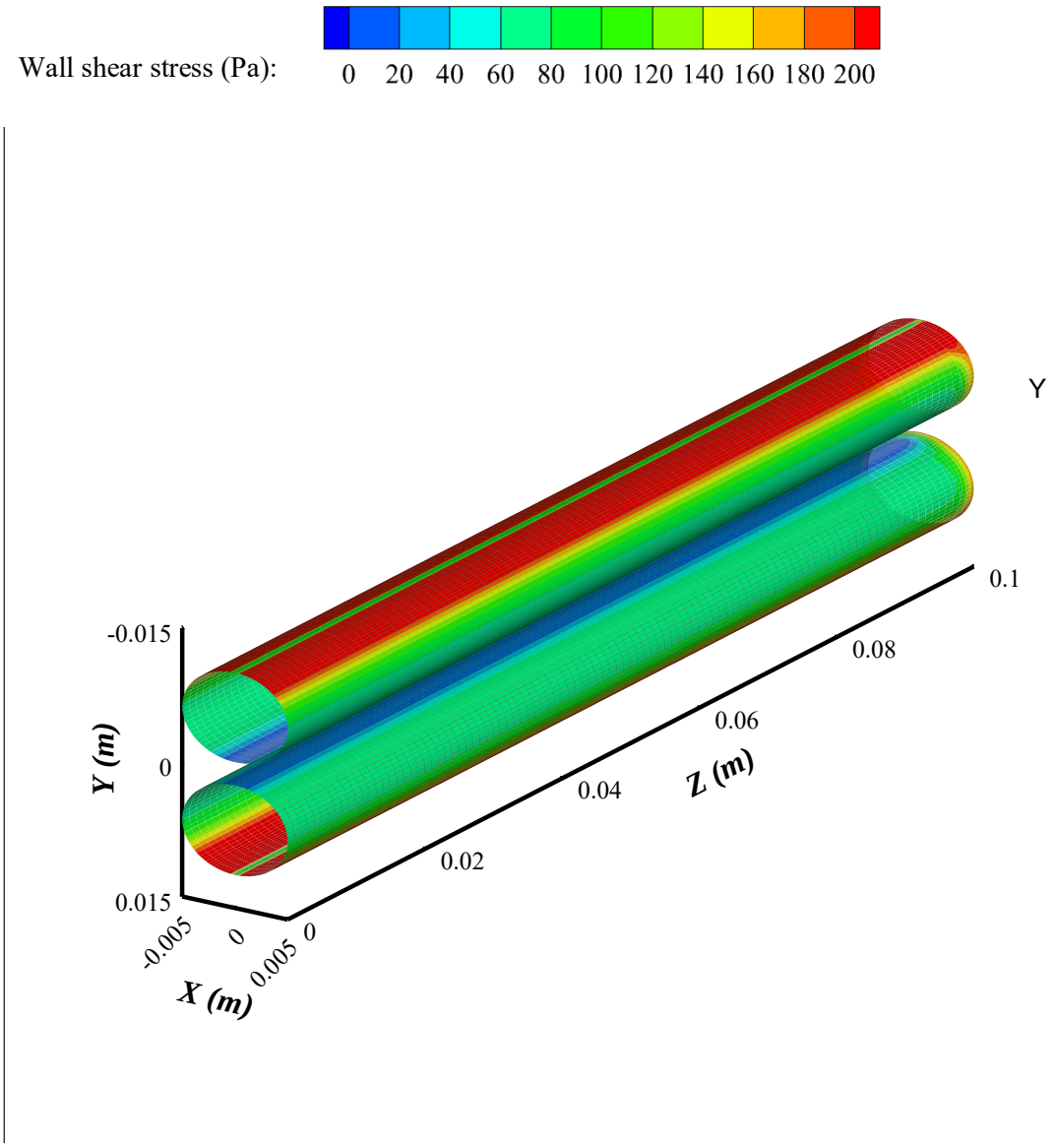

Fig. 4.17 Wall shear stress contour on cylinders for H*=2.3, ε*=0.02, W*=20, P*=1.0, Re=1.0

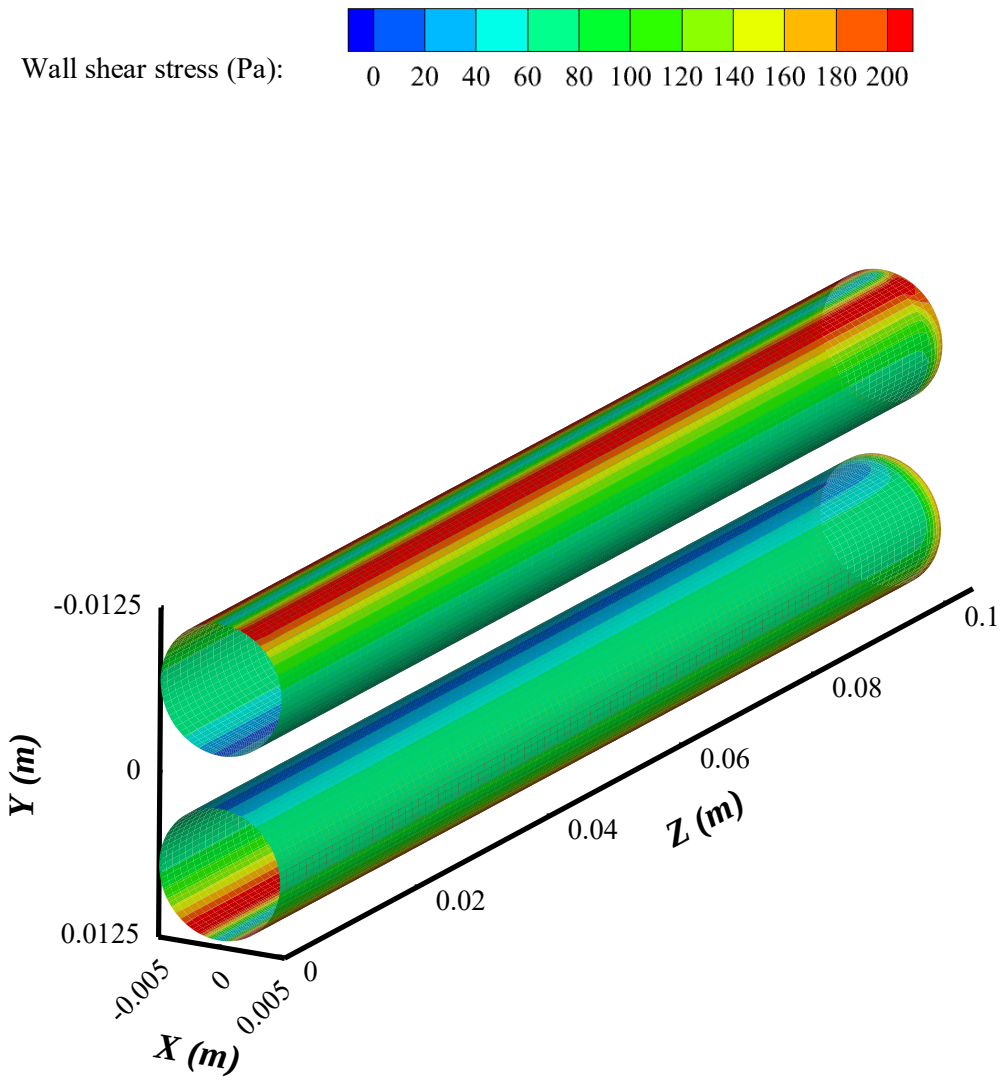

Fig. 4.18 Wall shear stress contour on cylinders for H*=2.5, ε*=0.05, W*=20, P*=1.0, Re=1.0

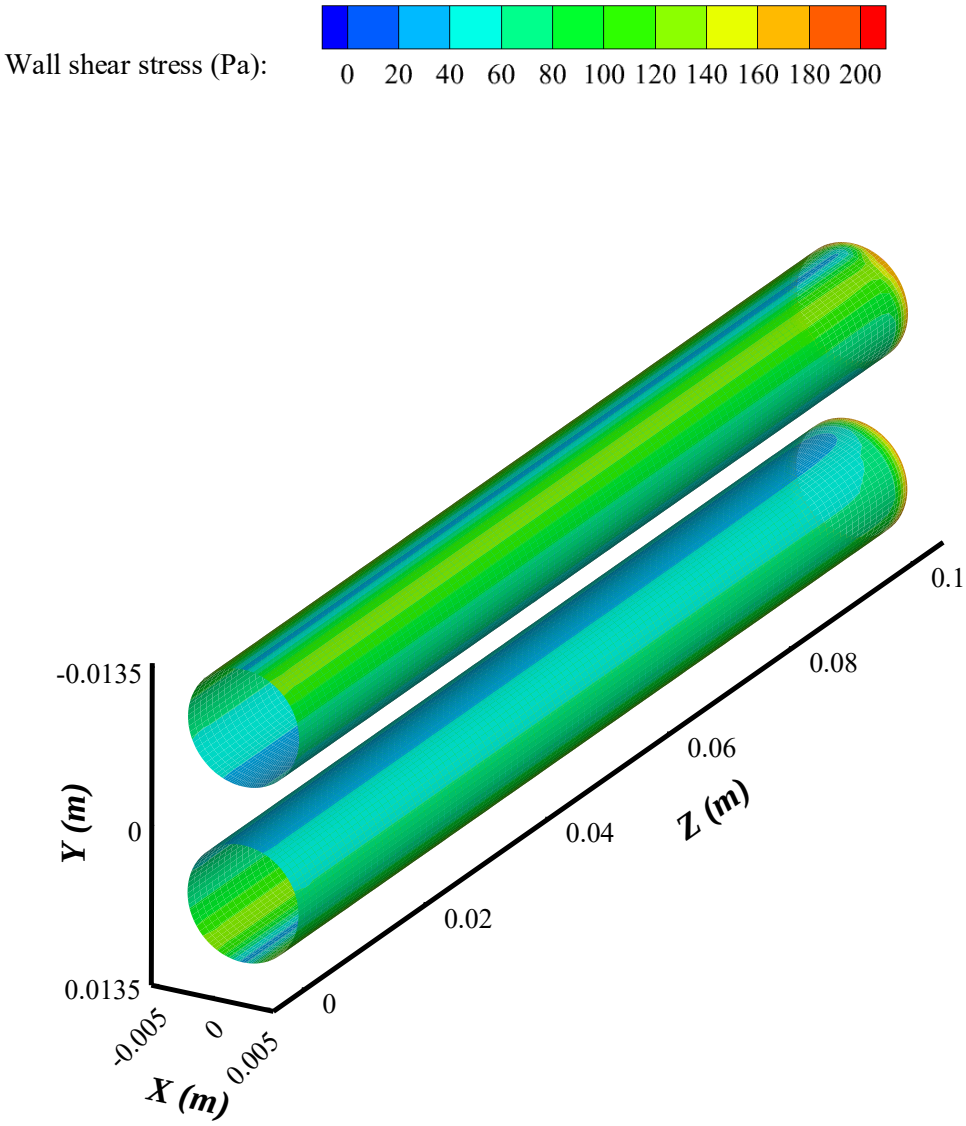

Fig. 4.19 Wall shear stress contour on cylinders for H*=2.7, ε*=.075, W*=20, P*=1.0, Re=1.0

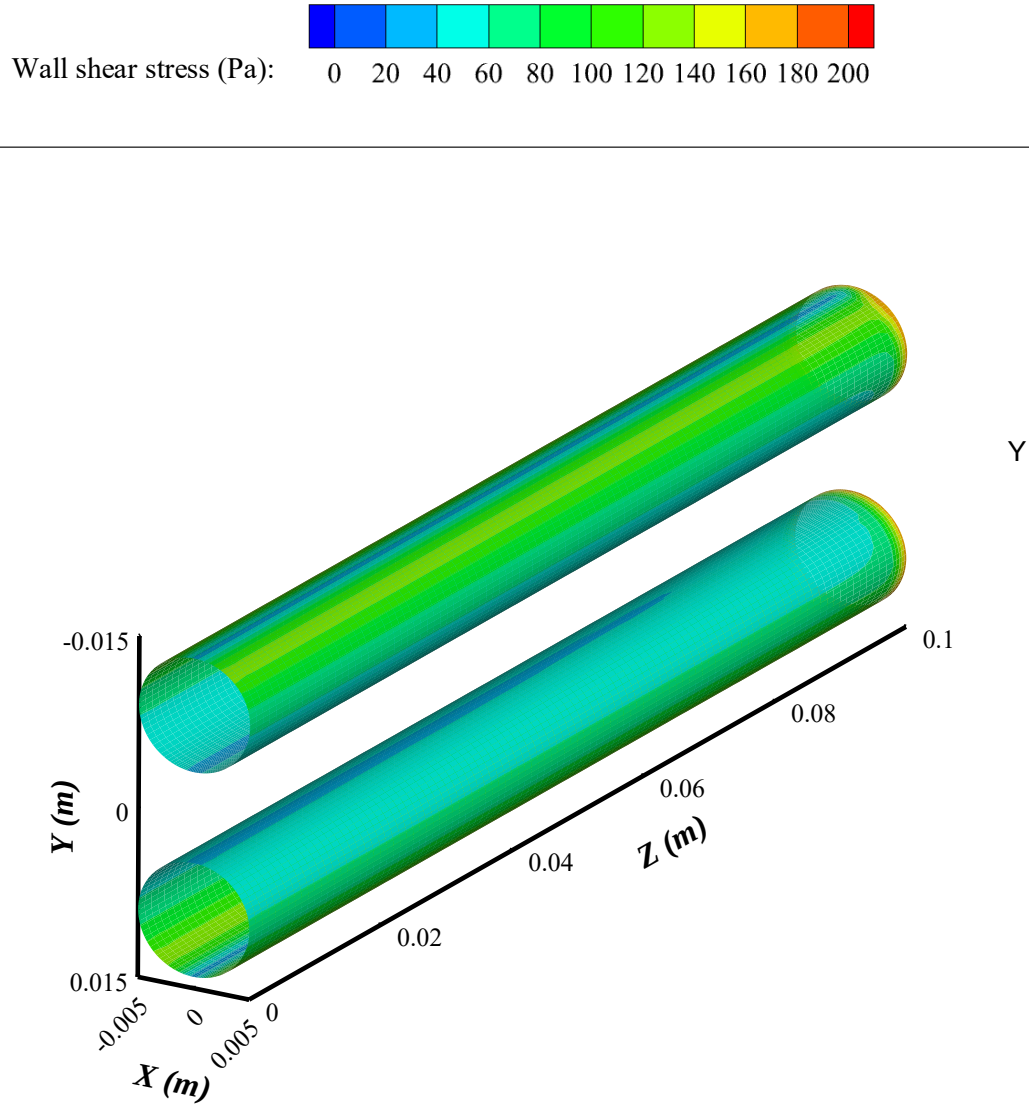

Fig. 4.20 Wall shear stress contour on cylinders for H*=3.0, ε*=0.10, W*=20, P*=1.0, Re=1.0

4.1.5 Pressure Distribution

The pressure distributions at symmetric plane for three pump configurations are shown in Fig. 4.21, for two locations: at upperchannel wall and at a horizontal line passing through the channel centerline axis. As the rotors are symmetrically placed inside the pump, the pressure distributions on upper and lower channel walls are similar. The pressure variation near the channel upper/ lower wall is the steepest because of the presence of the rotating cylinder. At a distance of one diameter from the rotor the pressure gradient is linear.

The pressure magnitudes near the upstream and downstream of pump configurations ($H^*=2.1$, $\varepsilon^*=0.01$) in Fig. 4.21(a) are higher than the configuration ($H^*=2.5$, $\varepsilon^*=0.05$)in Fig. 4.21(b), which is then higher than the configuration ($H^*=3.0$, $\varepsilon^*=0.10$) in Fig. 4.21(c). This is due to the change of relative position of rotors inside pump. However, an analysis from pressure contour section, it is found that the pressure magnitude of around the rotor regions at lower channel height and at lower wall clearance is higher than the others.

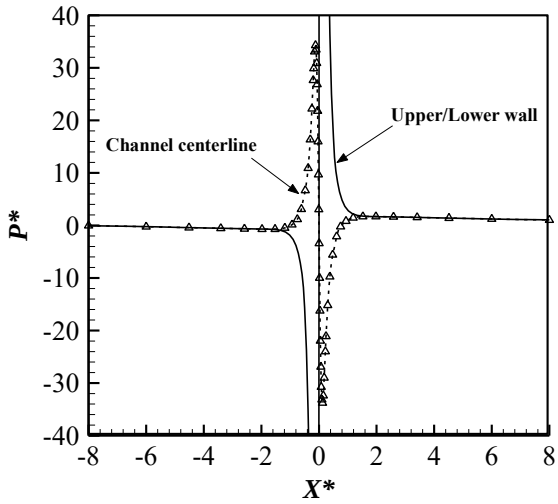

(a) H*=2.1, ε*=0.01

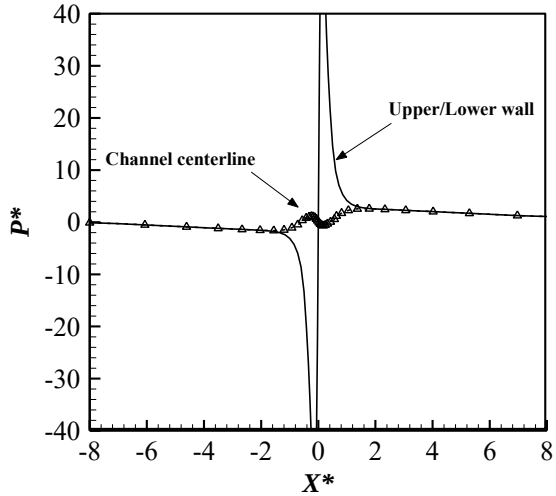

(b) H*=2.5, ε*=0.05

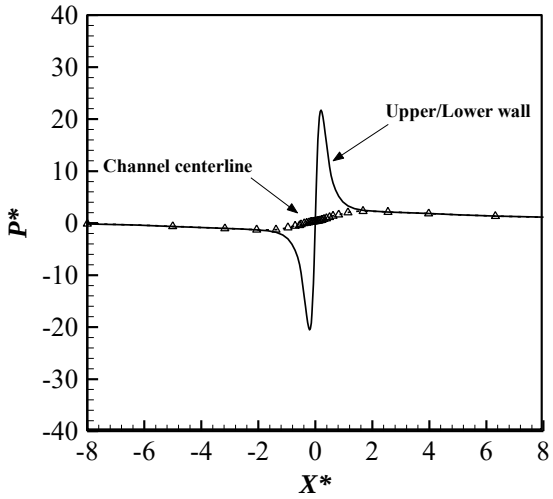

(c)H*=3.0, ε*=0.10

Fig. 4.21Pressure distributions on the channel upper/lower wall and channel centerline axis for W*=20, Z*=0, Re=1.0

4.1.6 Velocity Profile

The velocity profile along y-direction at different stream wise positions (X*) at symmetric plane (Z*=0) for the case of H*=2.5, ε*=0.05, W*=20 is shown in Fig. 4.22(a). The profiles for far upstream and far downstream are nearly parabolic i.e. maximum at channel centerline and gradually deceases near the bottom and upper channel surface. No significant variation in profile is found for X* ≥4.0 and X*≤ -4. But within the range -4<X*<4, the profiles differ with each other. Moreover, the same result is reflected in X-velocity contour shown in Fig. 4.22(b). With the help of color contrast, it is seen that the only significant variations occur within the range-4<X*<4.

Similarly, the X-velocity contour and the velocity profile along y-direction at different Z* as well as along z-direction at different Y* at X*=8 (outlet) are shown in Fig. 4.23 and Fig. 4.24respectively. Although the profiles along y-directions are parabolic, along z-directions it is highly dependent on the channel width W*. Fig. 4.25shows the variation of velocity profile along z-direction for different channel width W*. It is found that velocity profiles are becoming parabolic while the W* varies from higher to a lower value. Besides, it is observed that the velocity magnitude is highest at particular location i.e. Z* = +16.5/-16.5 for the case of H*=2.5, ε*=0.05, W*=40 and this location shifts to channel centerline with decreasing W*. In Fig. 4.27, with the help of color contrast, the highest velocity magnitude at different W* are shown. For better understanding results of X-velocity contour at different W* for channel H*=2.1 and H*=3.0 are shown in Fig. 4.26 and Fig. 4.28respectively.

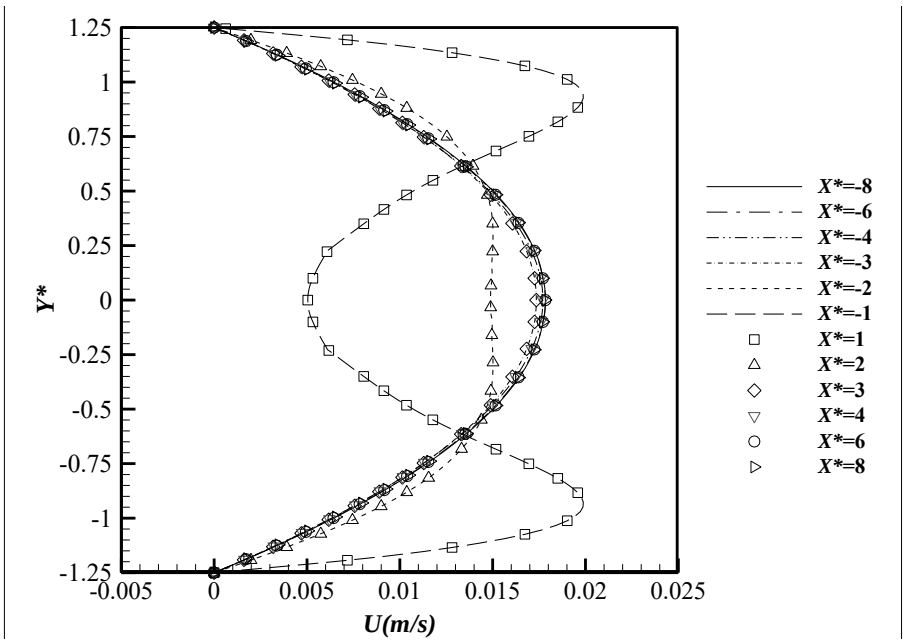

(a)

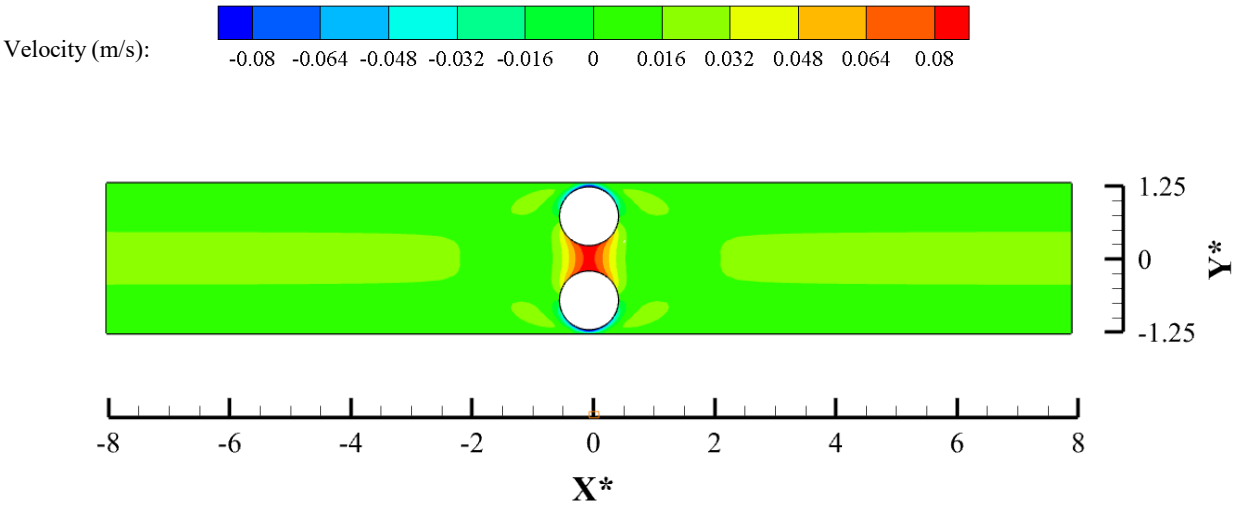

(b)

Fig. 4.22 (a) Velocity profile along y-direction at different X* (b) X-Velocity contour at Z*=0 (symmetric plane) for H*=2.5, ε*=0.05, W*=20, P*=1.0, Re=1.0

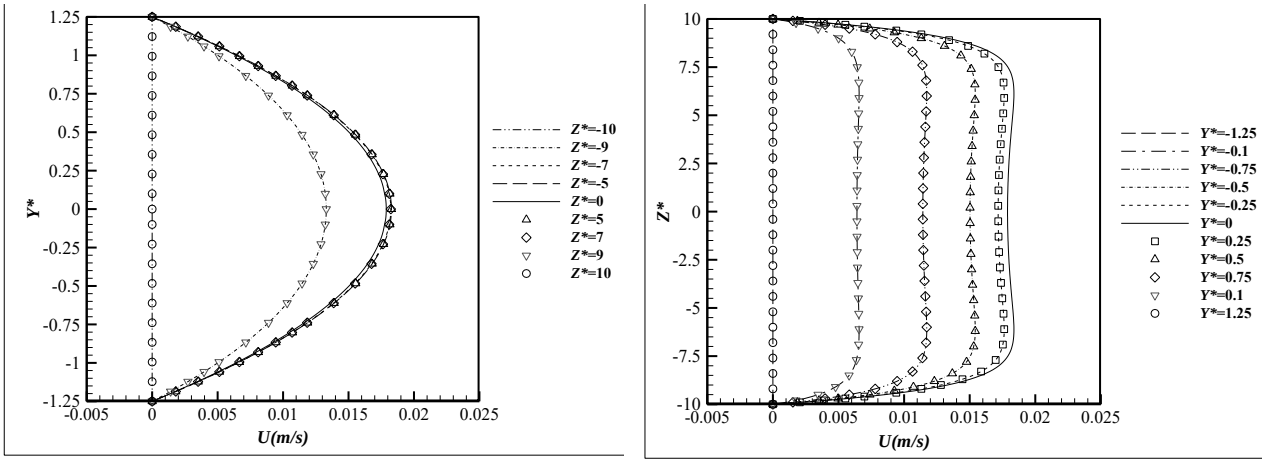

(a) (b)

Fig. 4.23 Velocity profile (a) along y- direction at different Z* and X*=8.0 (b) along z-direction at different Y* and X*=8.0 for H*=2.5, ε*=0.05, W*=20, P*=1.0, Re=1.0

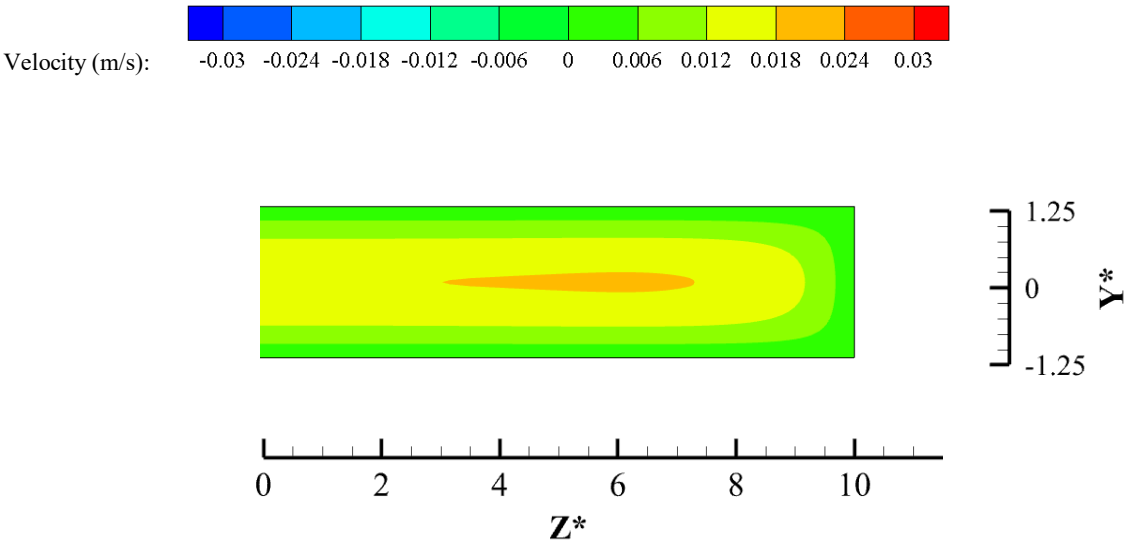

Fig. 4.24X-Velocity contour at X*=8.0 for H*=2.5, ε*=0.05, W*=20, P*=1.0, Re=1.0

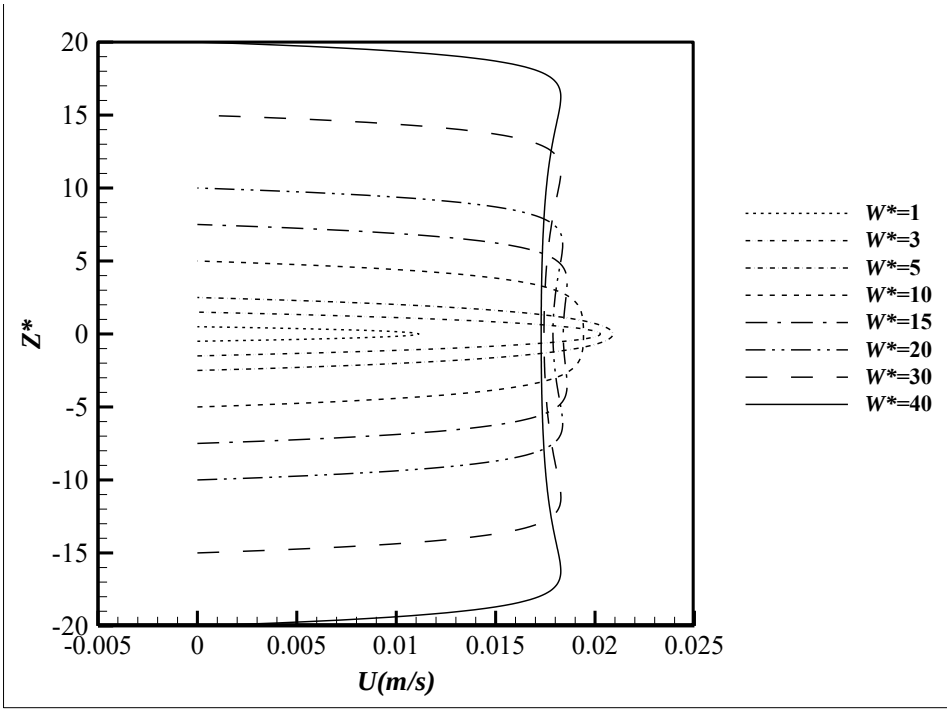

Fig. 4.25 Velocity profile along z-direction at X*=8.0 and Y*=0 for different W* and H*=2.5, ε*=0.05, P*=1.0, Re=1.0

Fig. 4.26X-Velocity contour at X*=8.0 for H*=2.1, ε*=0.01, W*=20, P*=1.0, Re=1.0

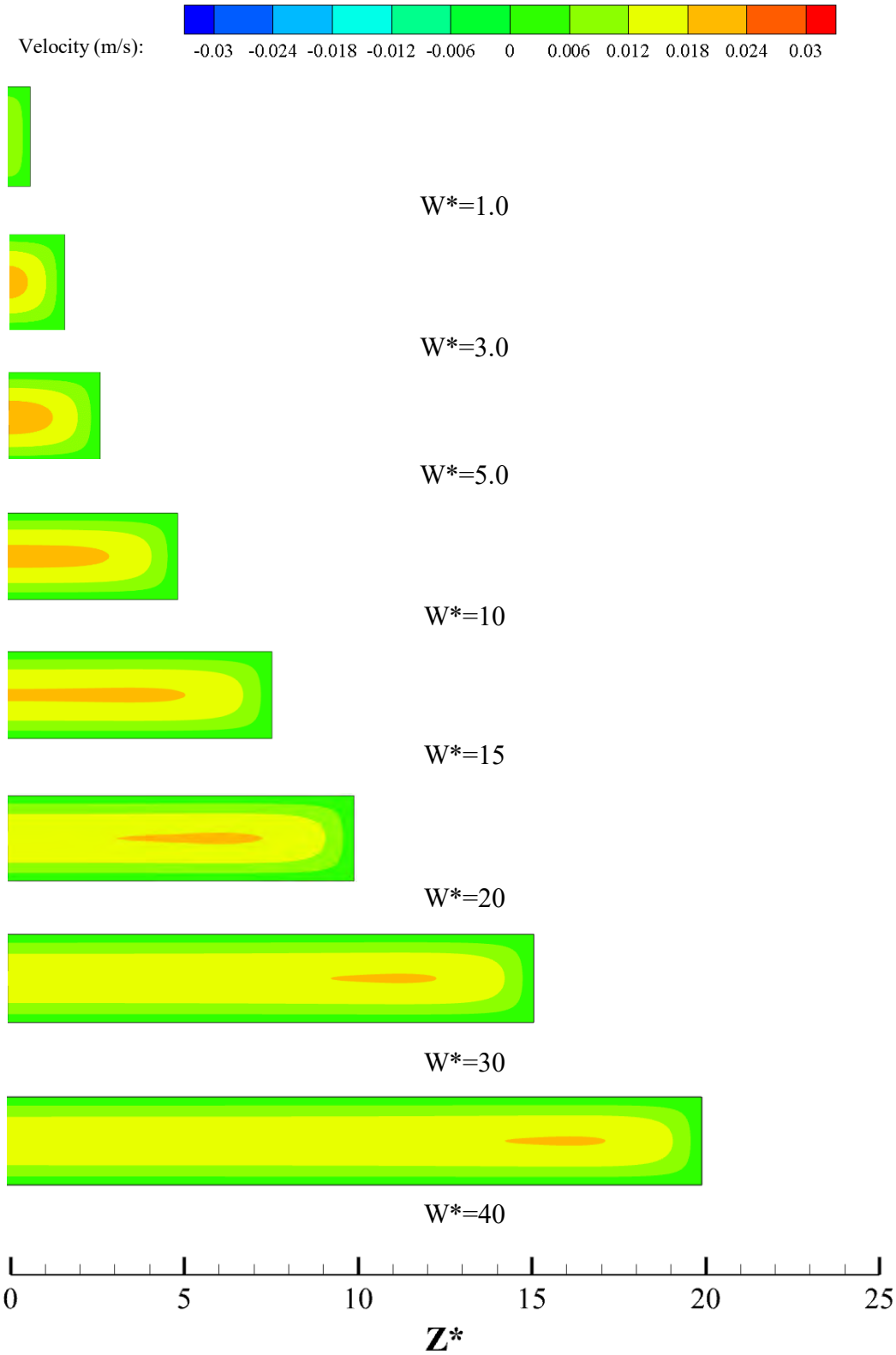

Fig. 4.27X-Velocity contour at X*=8.0 for H*=2.5, ε*=0.05, W*=20, P*=1.0, Re=1.0

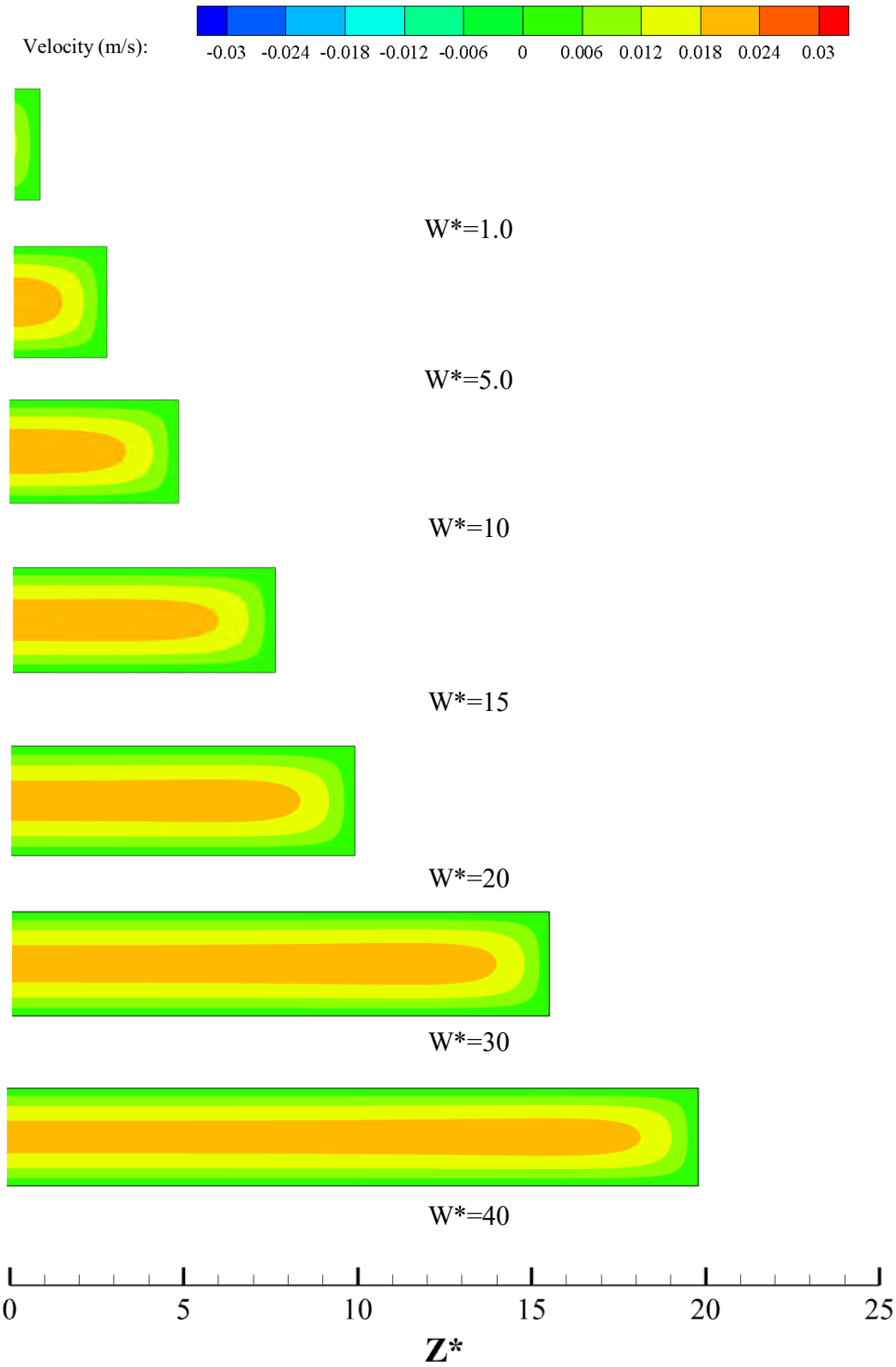

Fig. 4.28X-Velocity contour at X*=8.0 for H*=3.0, ε*=0.10, W*=20, P*=1.0, Re=1.0

4.2 Optimization of the Pump Configuration

4.2.1 Effect of Wall Clearance ε* and Channel Height H*

The rotor position i.e. the clearance between rotor surface and channel surface has a crucial effect on the performance of micropump. Because, the eccentric position of rotor introduces unequal shear stresses on upper and lower surfaces of the cylinder which provides the driving force to the fluid inside the micropump channel. Fig. 4.29(a) shows the variation of average velocity inside the channel as a function of wallclearance and channel height where the channel width is maintained at W*=20 and the operating flow parameters are kept at Re=1.0 and P*=1.0. It is found that the value of U* almost linearly decreases with the wall clearance at different channel height H* investigated. This is due to the reduction in effective flow area between cylinders with wall clearance which is described with the velocity vector field in Fig. 4.30 for the case of H*=2.5. Besides, the vortices effect that is stronger at lower channel height shown in stream wise flow in Fig. 4.1 to Fig. 4.3, is also responsible for the lower value of U*. However, the U* value is higher for larger channel height at particular rotor position.

In the next step, in Fig. 4.29(b), the effect of ε*and H* on the rotor driving power T* is shown. The value of T* decreases nearly exponentially with the ε* and the effect H* on driving power is insignificant. This variation is due to the velocity gradient from the cylinder surface to the channel wall that varies mainly with wall clearance ε*. When the rotors are adjacent to the channel wall, the velocity gradient quickly increases, so the wall shear stress on rotor and the driving power sharply increase to a very high value. The wall shear stress distribution developed on rotors surface for the case of H*=2.5, W*=20 is shown in Fig. 4.31, which clarifies the ε* effect that the more narrowed the gap between rotating cylinder and channel surface, the higher the value of wall shear stress on rotors. The Fig. 4.29(c) shows the effect of ε*and H* on pump efficiency at flow condition Re=1.0 and P*=1.0. It is seen that there is an optimum rotor position for a particular channel height where the best performance is obtained. All the plots have the similar pattern: initially it is increasing with ε*, reaches a maximum point and then decreases. The respective optimum values of ε* for channel heights 2.1, 2.3, 2.5, 2.7 and 3.0 are 0.01, 0.02, 0.05, 0.075 and 0.10. The optimal position of rotor for channel height of H*=2.5 is checked for different flow conditions by varying P* in Fig. 4.32, which results in same observations.

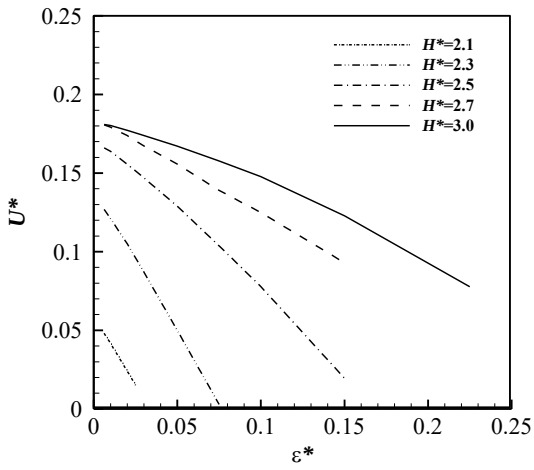

(a)

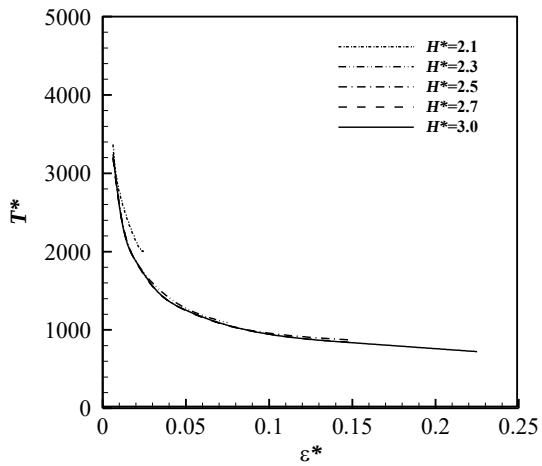

(b)

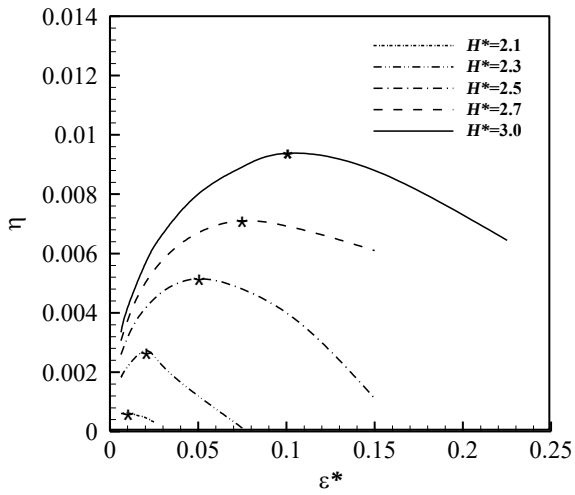

(c)

Fig. 4.29 Effect of geometric parameters on pump (a) average velocity (b) driving power and (c) efficiency for W*=20,Re=1.0, P*=1.0.

The relationship between the optimized wall clearance and the channel height is approximately linear and can be written in the following form.

$$\varepsilon^* \cong \frac{H^* - 2}{10} \qquad 4.1$$

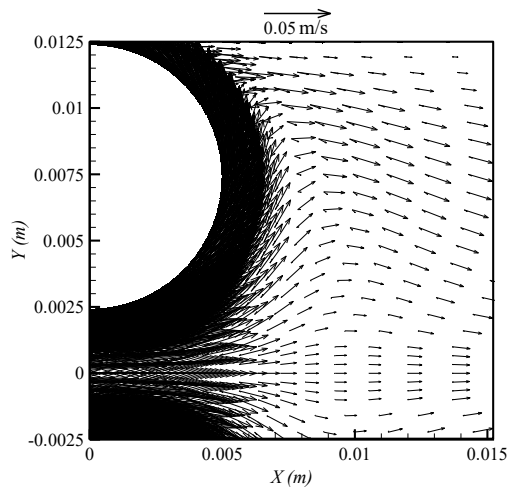

(a) ε*=0.01

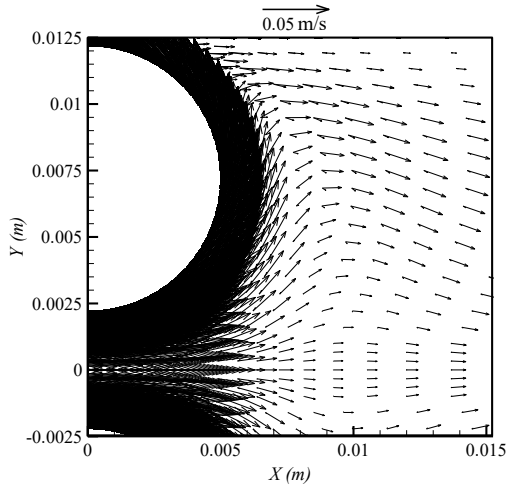

(b) ε*=0.03

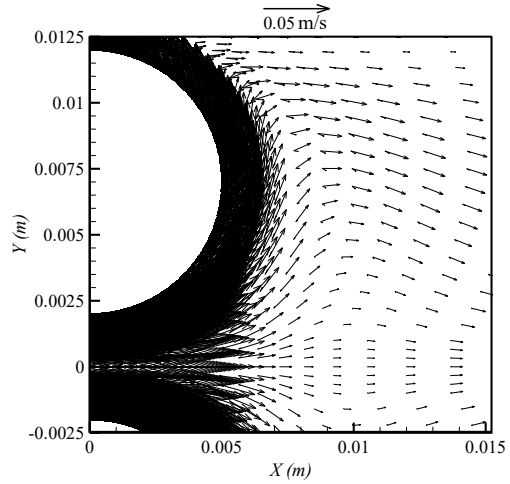

(c) ε*=0.05

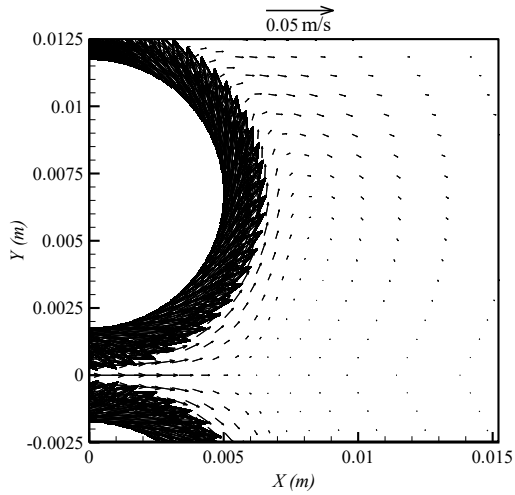

(d) ε*=0.075

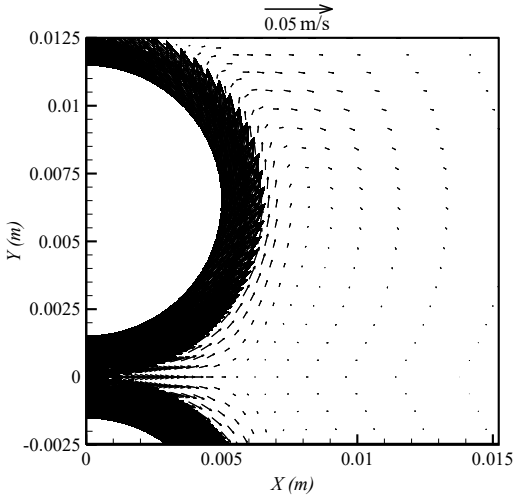

(e) ε*=0.10

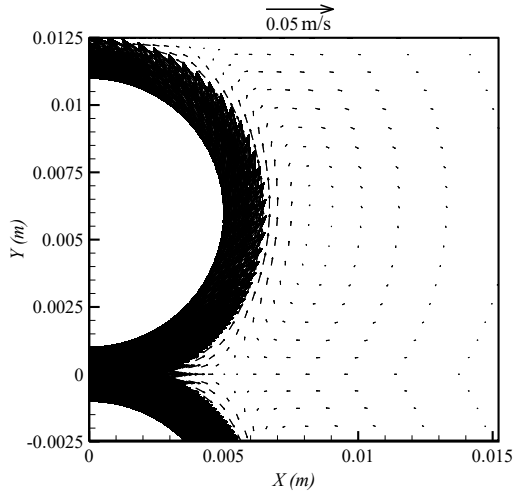

(f) ε*=0.15

Fig. 4.30Velocity vector field on near downstream inside pump for different wall clearance and H*=2.5, W*=20, Re=1.0, P*=1.0

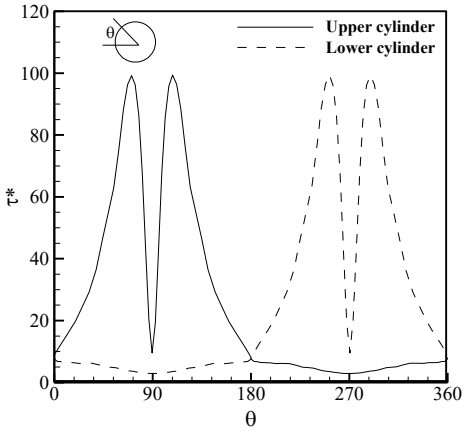

(a) ε*=0.01

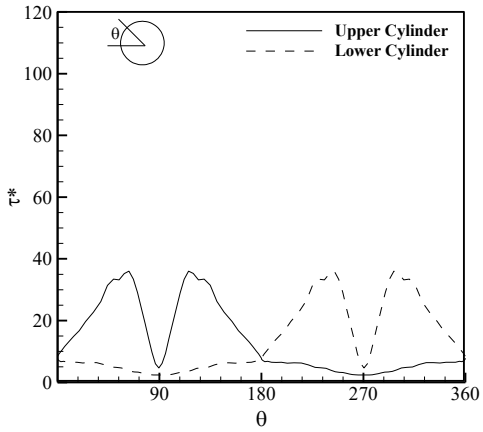

(b) ε*=0.03

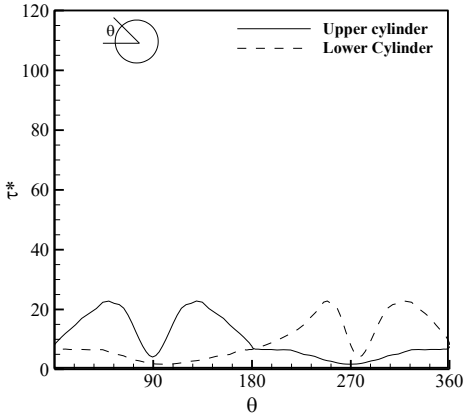

(c) ε*=0.05

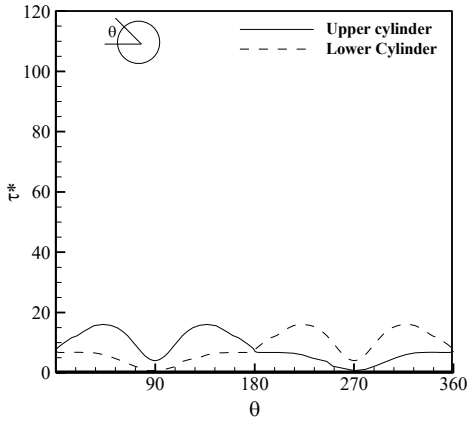

(d) ε*=0.075

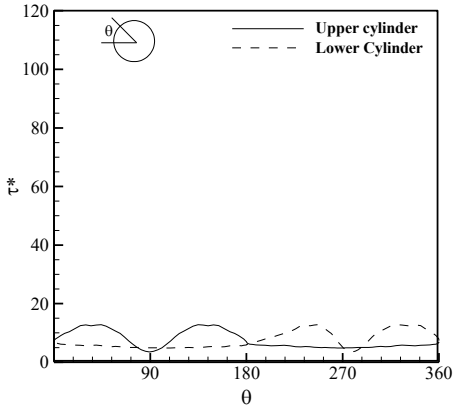

(c) ε*=0.10

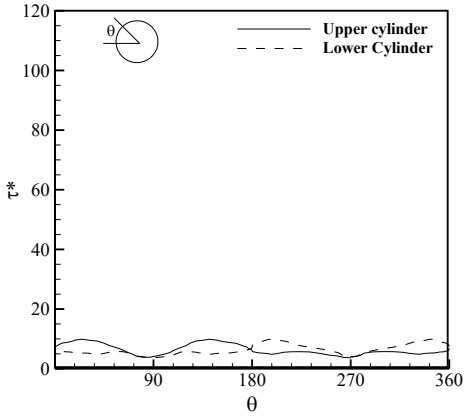

(d) ε*=0.015

Fig. 4.31Wall shear stress distribution around the cylinder at different wall clearance for H*=2.5, W*=20, Z*=0, Re=1.0, P*=1.0.

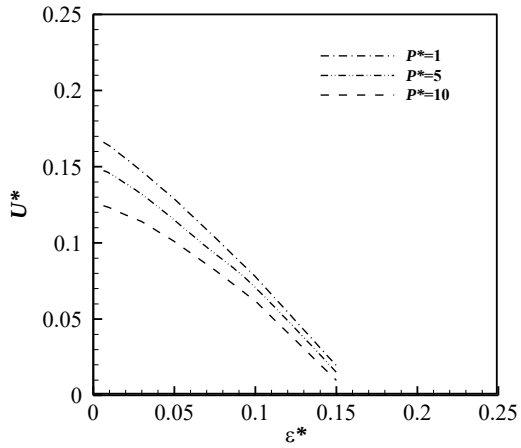

(a)

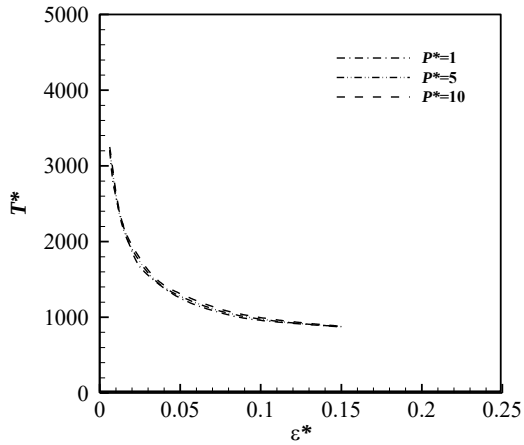

(b)

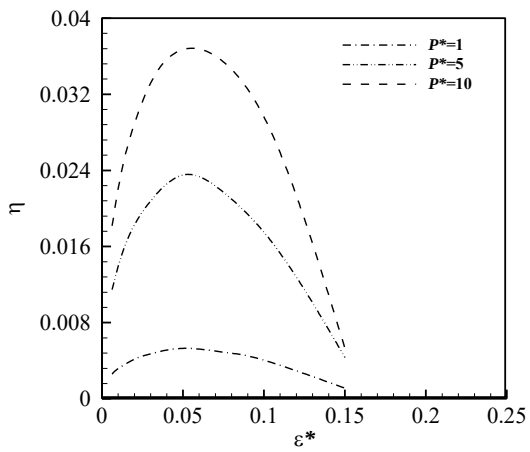

(c)

Fig. 4.32Effect of pump load on (a) average velocity (b) driving power and (c) efficiency as a function of **ε*** forH*=2.5, W*=20, Re=1.0.

4.2.2 Effect of channel width W*

The channel width i.e. the side walls effect is investigated by varying W* from 1 to 40 at channel height of 2.1, 2.5 and 3.0, which is presented in Fig. 4.33-Fig. 4.35. In Fig 4.34(a), shows that a gradual decrease of average velocity as the side walls become closer for the case of H*=2.5 and ε*=0.05. Because, with the smaller value of W*, it provides increased viscous resistance to the flow. This effect is explained with the help of X-velocity contour in Fig. 4.26-Fig.4.28. Moreover, the variation of U* is found insignificant when 3D channel width is 20 times the rotor diameter.

The Fig. 4.34(b) shows a linear relationship of driving power T* and channel width W*. As there is an increase of dimension in z axis, the pump requires more power to drive a larger amount of fluid volume. The effect of W* on efficiency is mainly the reflection of the effect of W* on the average velocity U*, which is shown in Fig. 4.34(c). Therefore, the channel height greater than 20 has only minimum influence on pump efficiency. However, for better understanding, the channel width W* effect on other pump configurations (which is shown in Fig. 4.33 and Fig. 4.35) are also checked which results in same observations.

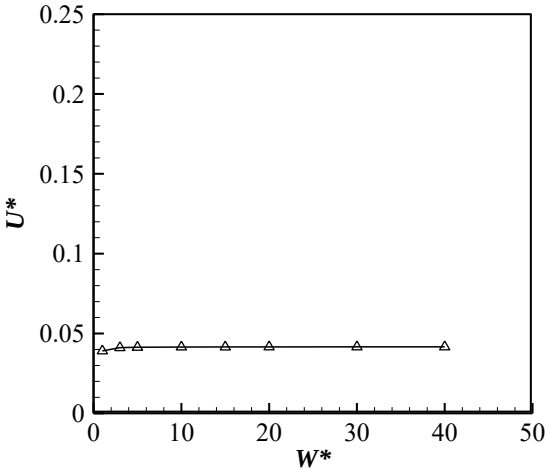

(a)

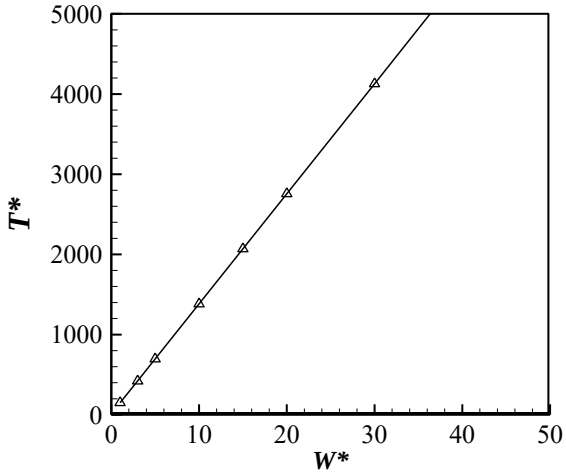

(b)

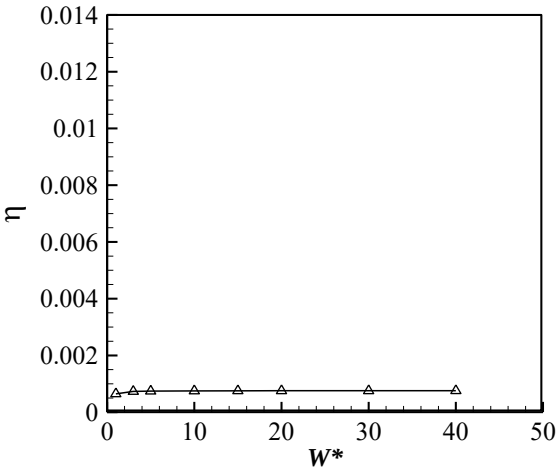

(c)

Fig. 4.33Effect of channel width on pump (a) average velocity (b) driving power and (c) efficiency for **H*=2.1**, ε*=0.01, Re=1.0, P*=1.0.

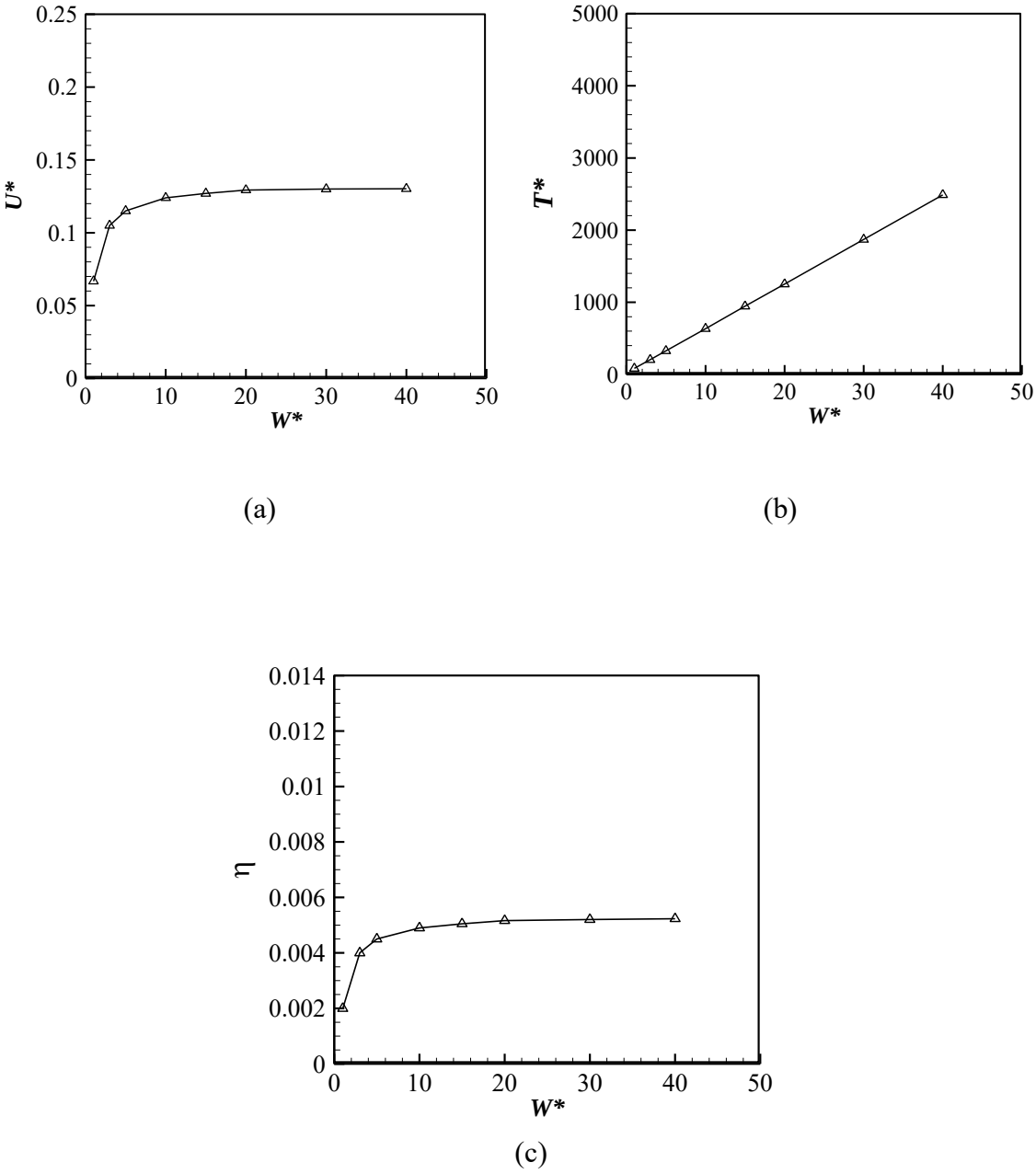

Fig. 4.34Effect of channel width on pump (a) average velocity (b) driving power and (c) efficiency for **H*=2.5**, ε*=0.05, Re=1.0, P*=1.0.

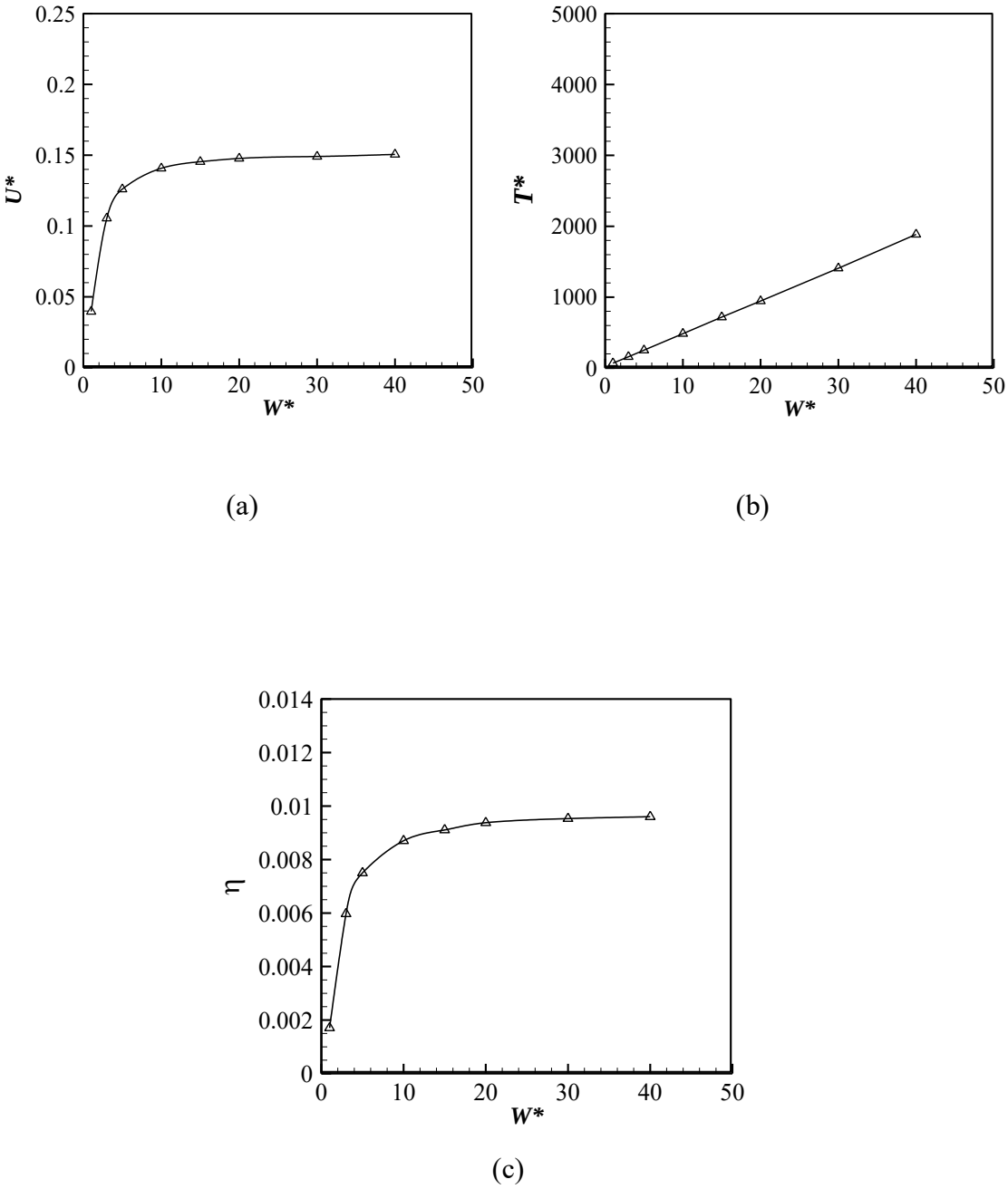

Fig. 4.35Effect of channel width on pump (a) average velocity (b) driving power and (c) efficiency for **H*=3.0**, ε*=0.10, Re=1.0, P*=1.0.

4.2.3 Effect of Reynolds Number

In this section the effect of Reynolds number i.e. the rotors speed effects inside the micro pump will be studied in detail. Most of the cases are presented in this study for Re=1 (i.e. 168 RPM), Re=5 (i.e. 840 RPM) and Re=10 (i.e. 1680 RPM), since Reynolds number up to 10 is the most usual physical operating condition for micro pump [18]. Some cases up to Re=100 (i.e. 16800 RPM) were studied to interpret the effects of increasing Reynolds number on flow field beyond the operating range. Fig. 4.36-Fig.4.37 showthe effect of Reynolds number on average velocity, driving power and efficiency for the case of $H^*=2.5$, $\varepsilon^*=0.05$, $W^*=20$, $P^*=1.0$. Here, the vertical axis in Fig. 4.36 (b) and Fig. 4.36 (d) are presented in dimensional parameter for better understanding of the effect of Re. According to the numerical results, a linear relation of average velocity with Re and an exponential growth of driving power with Re are found. Therefore, it results in very low efficiency at higher Reynolds number presented in Fig. 4.37. Flow fields inside micro pump are found stream wise flow at different Reynolds number which is shown in Fig. 4.38.

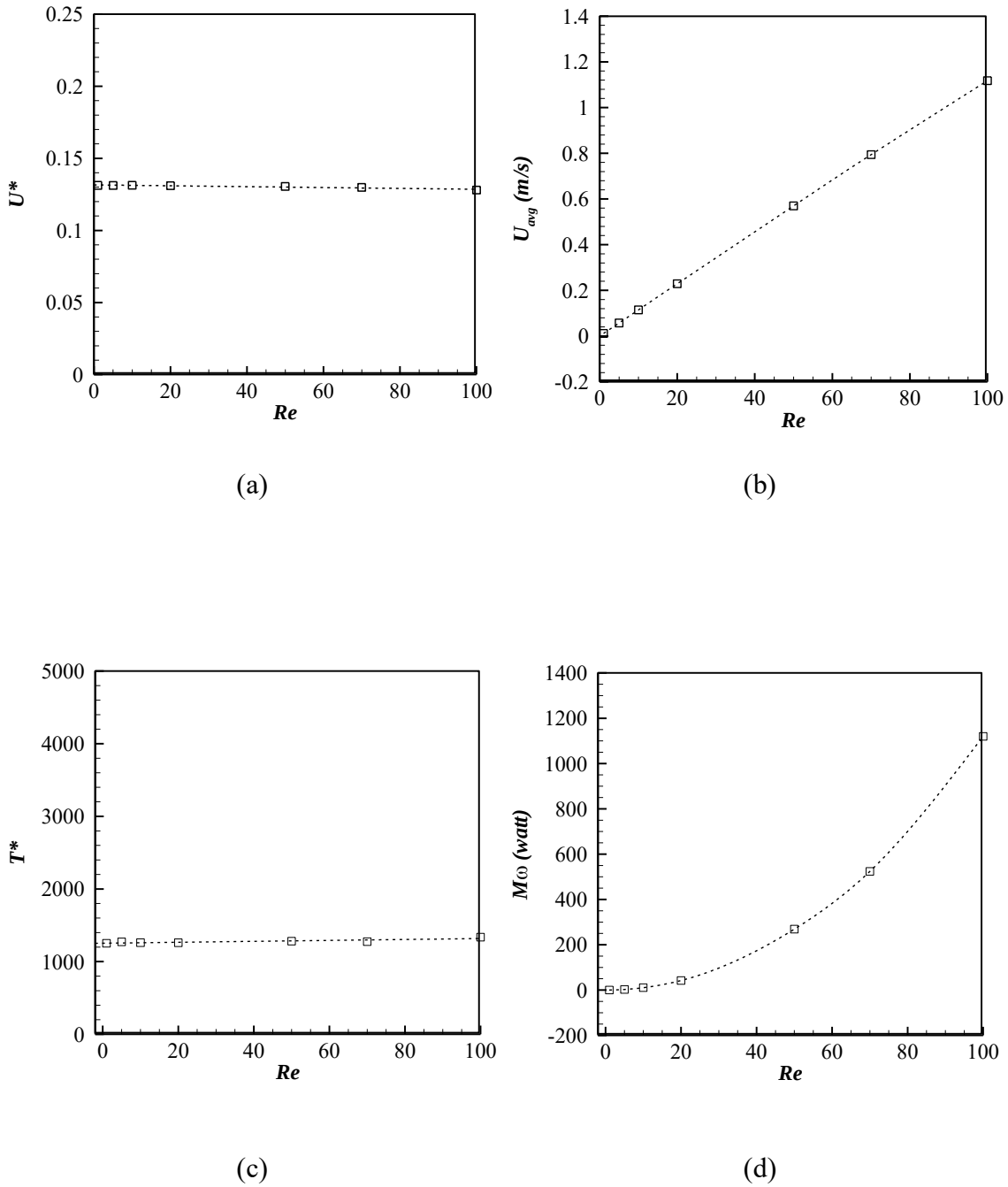

Fig. 4.36Effect of Reynolds number on average velocity and driving power forH*=2.5, ε*=0.05,W*=20, P*=1.0[(a), (c) non-dimensional form (b), (d) dimensional form]

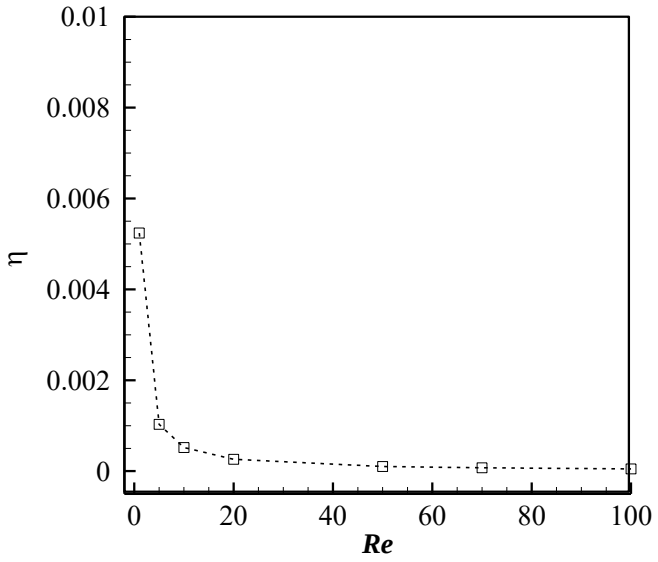

Fig. 4.37Effect of Reynolds number on efficiency forH*=2.5, ε*=0.05, W*=20,P*=1.0

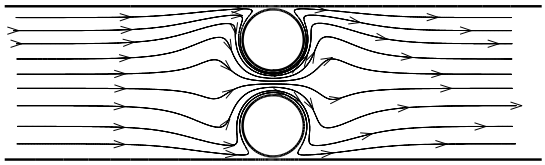

(a) Re=1

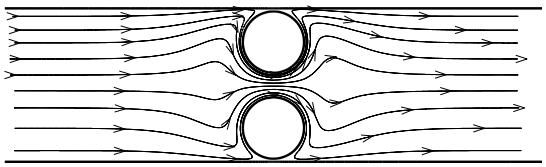

(b) Re=5

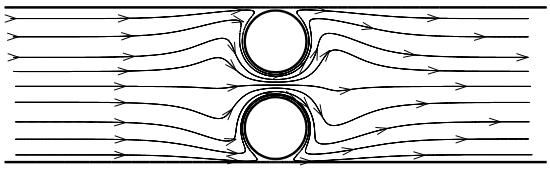

(c) Re=10

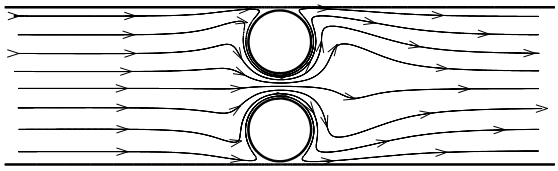

(d) Re=50

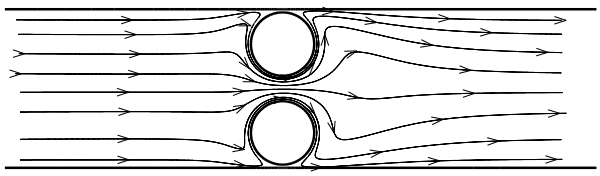

(e) Re=100

Fig. 4.38 Streamlines at Z*=0 (symmetric plane) for different Re and H*=2.5, ε*=.05, W*=20, P*=1.0

4.2.4 Effect of Pump Load

Fig. 4. 39 (a) shows the effect of back pressure (i.e. setting an external pressure at pump outlet) on the average velocity for different Reynolds numbers. Here, Reynolds number is used to characterise the rotor speed of micropump. At constant Reynolds number, the magnitude of U* decreases almost linearly with P*. Because the higher the back pressure is set at outlet, the lower the average velocity of the pump. Also, it is observed that at a particular rotor speed the flow inside the pump is positive up to a certain pump load limit. Otherwise, beyond that limit the flow is reversed. Fig. 4.40 shows the flow pattern for the case of H*=2.5, ε*=0.05, W*=20, Re=1 at different P* which clearly clarifies the pump load effect on flow performance. As the pump load increases, a one pair of vortices is formed both at downstream and upstream side which are increased in size, restricting the effective flow.

The effect of pump load on driving power is shown in Fig. 4.39 (b) for different rotor speeds i.e. Re=1, 5 and 10. Here, it is seen that the value of driving power increases with the increased value of P*

Fig. 4.39(a) shows that the pump load limit for Re =1, 5 and 10 are around 40, 210 and 420 respectively. So, it indicates that the pressure load range is wider for higher Re. Moreover, there is a particular pump load at different Re in which the efficiency of the pump becomes maximum: Re=1, P*=10; Re=5, P*=100 and Re=10, P*=220 are the highest efficiency point for the case of H*=2.5, ε*=0.05, W*=20 shown in Fig. 4.39(c). In addition, the pressure load effect on other optimal configurations at different channel heights are illustrated in Fig. 4.41. It shows that the configurations at lower channel height can able to work comparatively at higher pressure load range and can provide best performance at higher pressure.

Moreover, the performance of the best configuration of a single rotor type pump (H*=1.5, ε*=0.10) is presented in Fig. 4.41, to show a comparison in performance with different configurations of dual rotor type pump. Form numerical results, it is confirmed that dual rotor type viscous micropump can provide the best efficiency, the higher flow rate as well as capable of withstanding with higher back pressure than that of single rotor type viscous micropump.

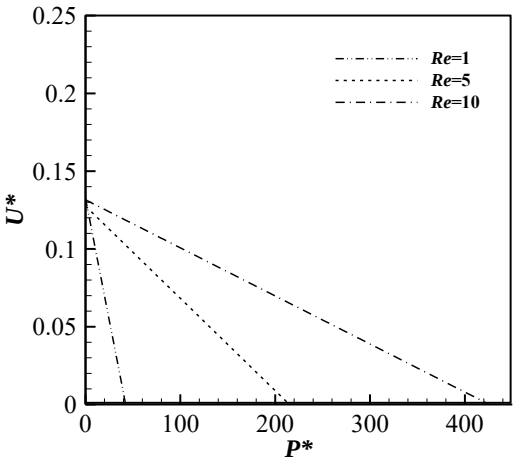

(a)

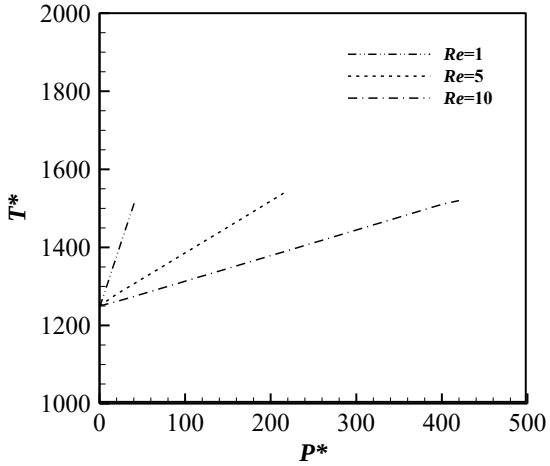

(b)

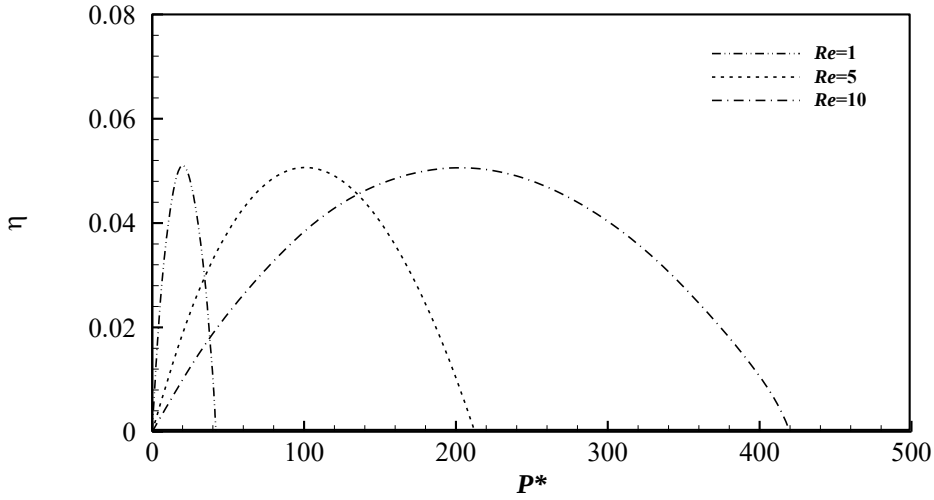

(c)

Fig. 4.39Effect of flow parameters on (a) average velocity (b) driving power and (c) efficiency a for H*=2.5, ε*=0.05, W*=20

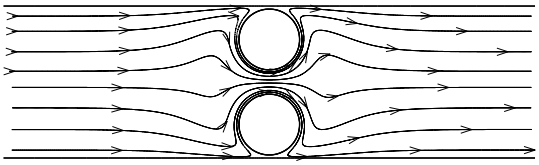

(a) P*=0

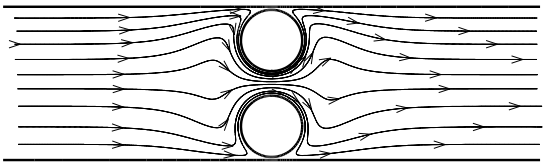

(b) P*=1

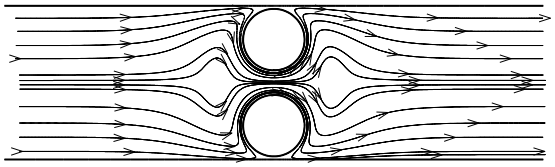

(c) P*=10

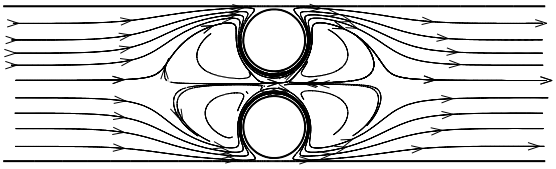

(d) P*=20

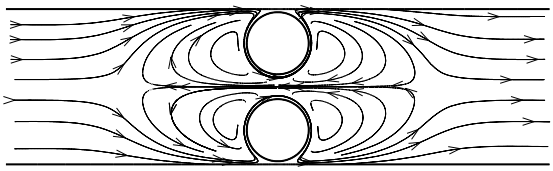

(e) P*=30

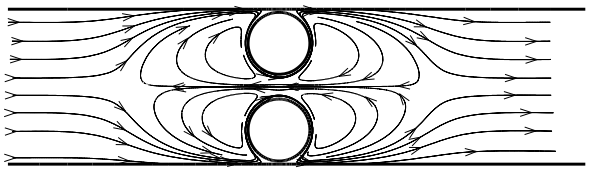

(f) P*=40

Fig. 4.40 Streamlines at Z*=0 (symmetric plane) for different P* and H*=2.5, ε*=0.05, W*=20, Re=1.0.

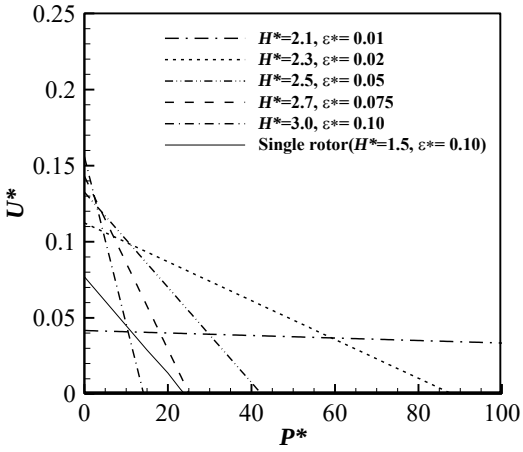

(a)

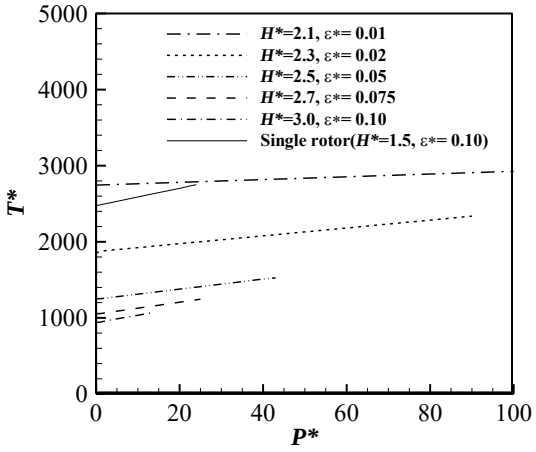

(b)

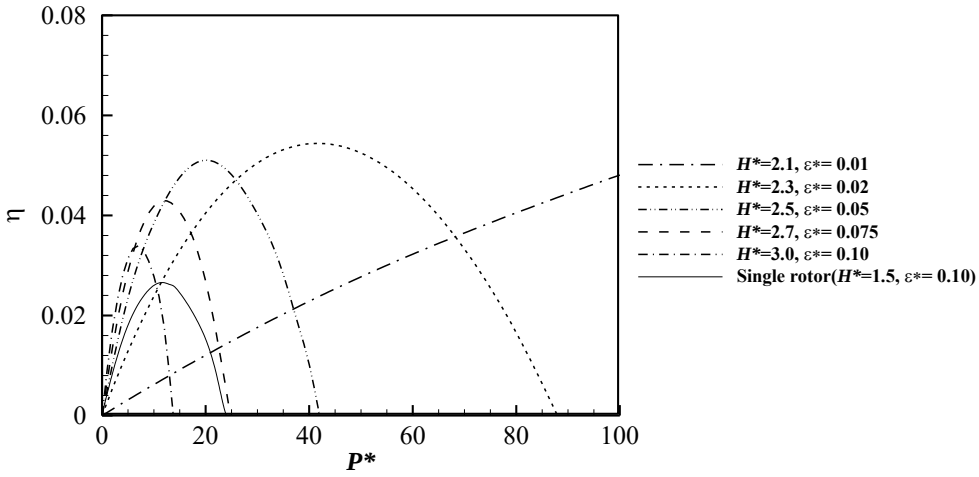

(c)

Fig. 4.41 Performance comparisons of different pump configurations for W*=20, Re=1.0.

4.3 Non-Newtonian Fluid Flow in Dual rotor Micro Viscous pump

As it is well known that the Newtonian assumption of fluid does not always work well in practical case. Therefore, we need to propose a model to describe the flow behavior of non-Newtonian fluid. Based on the shear rate dependency on shear viscosity, flow behavior that a fluid will exhibit one of the following models: power law model, Bird-Carreau Model, Carreau-Ysuda model, Cross-Power Law Model, Herschel-Bulkley Model, Bingham model etc. The most frequent research as well as the recent major concern of non-Newtonian fluid i.e. human blood is an example in biomedical applications. According to Walburn et. al. [45], power law model postulates power law dependence of viscosity on the shear rate for human blood and provides a good approximation of the stress strain relationship. Therefore, in the present study we investigate the micropump design with blood flow as well as other bio fluids that can be approximate from the power law. The power-law model for a non-Newtonian flow is expressed as

$$\mu = m\gamma^{n-1}$$

Where, m and n are the consistency coefficient and the power law index, respectively and γ is the shear rate.

4.3.1 Validation with Analytical Solution

For validation the model with non-Newtonian flow, the numerical results are compared to 2D analytical solution of fully developed velocity profile given by Bird et. al. [46]. The analytical solution of velocity profile is read as

$$\frac{U(y^*)}{U_{avg}} = \frac{(1+2n)}{(1+\mathrm{n})}[1-(2y^*)^{1+\frac{1}{n}}]$$

Where, y^* denotes the dimensionless distance measured from the center of the channel and $U(y^*)$ is the local velocity inside the channel.

Fig. 4.42shows the velocity profile of micropump at different power law index. The velocity profile is taken from the longitudinal location located at X*=4.0 of the channel downstream side as no significant variation in velocity profiles for X*≥ 4.0 shown for the case of H*= 2.5, ε* = 0.05, Re=1.0, P*=1.0, n=0.785 in Fig. 4.44. The Fig. 4.42 shows a good agreement between the analytical solution and the numerical results for different values of n: 0.5, 0.785, 1.0, 1.25 and 1.5. Again, the ratio $U(y^*=0)/U_{avg}$ i.e. the maximum velocity attained

at centerline is compared with the analytical solution in Fig. 4.43which also justify the numerical results.

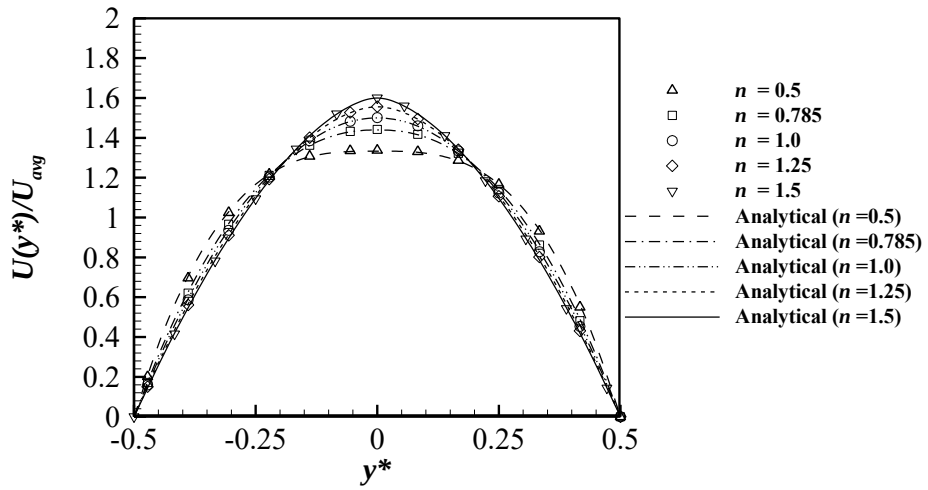

Fig. 4.42 Validation of fully developed velocity profile (2D) for H*= 2.5, ε* = 0.05, Re=1.0, P*=1.0

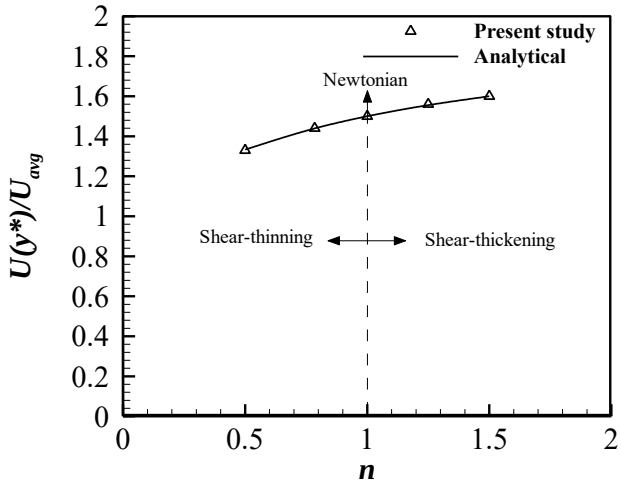

Fig. 4.43 Comparison of analytical and numerical ratio forH*= 2.5, ε* = 0.05, Re=1.0, P*=1.0, 0.5 ≤ n ≤1.5.

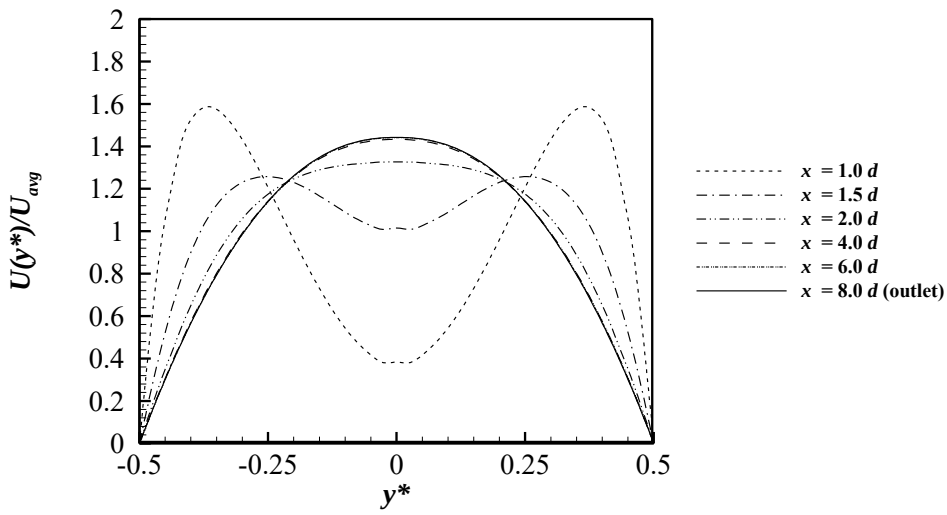

Fig. 4.44 Development of velocity profile (2D) at different sections on downstream side for H*= 2.5, ε* = 0.05, Re=1.0, P*=1.0, n=0.785.

4.3.2 Optimization of the Model with non-Newtonian Fluid Flow

The optimization of the geometrical configuration of micropump design is carried out for non-Newtonian fluids n=0.785 (considered as shear thinning) and n=1.5 (considered as shear thickening) at same flow condition (Re=1.0, P*=1.0) as it was done for optimization with Newtonian fluid (n=1.0). The Fig. 4.45 shows the variation of average velocity, driving power and efficiency with wall clearance ε* for n=0.785, 1 and 1.5. The trend of the plots for n=0.785 or 1.5 are quite similar to that of Newtonian (n=1.0) results, but there is significant variation in their numerical values. The Fig. 4.45(a) and (b) show that the plot for average velocity and driving power are shifted upward with power law index n, while in Fig. 4.45 (c) for efficiency plot it is shifted downward. For a particular wall clearance, it is seen that there is a constant increase in average velocity U* with n, while in driving power the increment is significantly high because of the higher power requirement for shear thickening fluid to keep rotor rotation at same speed. That's why the efficiency is very low compared to low value of n.

However, the micropump optimization for H*=2.5, W*=20 with n=0.785 and 1.5 is obtained at ε*=0.05 which is same for flow with Newtonian fluid. The effects of rotor clearance on flow field for n=0.785 and n=1.5 inside the micropump are shown in Fig. 4.46 and Fig. 4.47 respectively. The flow pattern for n=0.785 in all cases are same except higher curvature of streamline around the cylinder at ε*=0.1 and 0.15. Similarly, the flow patterns for n=1.5 are quite same upto ε*=0.05, but after that one pair of vortices is appeared both at upstream and downstream side which increases in size gradually with ε*.

The effect of channel width W* with non-Newtonian fluid of n=0.785 on pump performance is shown in Fig. 4.48. The W* effect is also found insignificant when W* ≥ 20. Therefore, this same configuration is used for next study with non-Newtonian fluid flow.

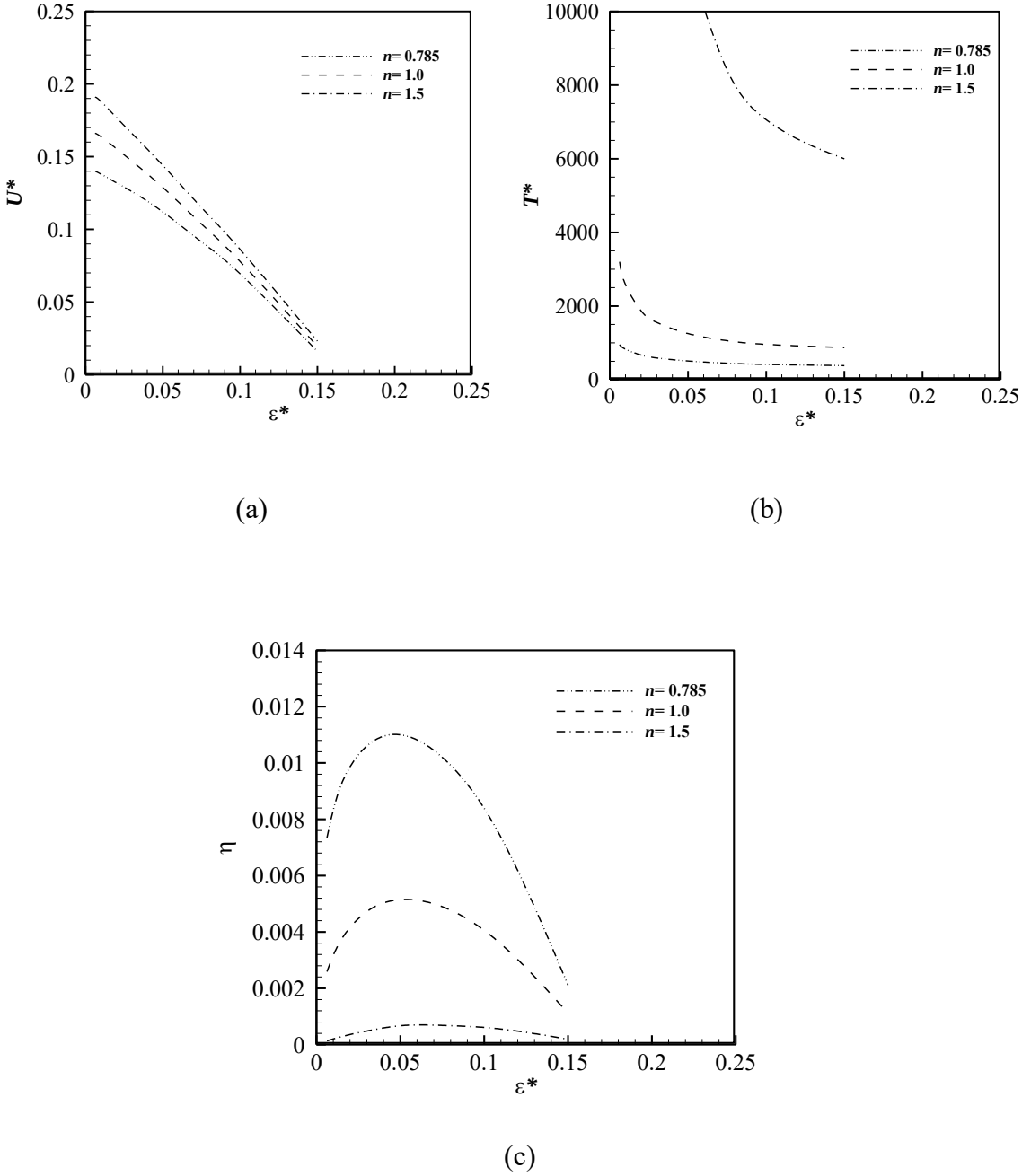

Fig. 4.45 Effect of geometric parameters on pump (a) average velocity (b) driving power and (c) efficiency for different values of n and H*=2.5, W*=20, Re=1.0, P*=1.0.

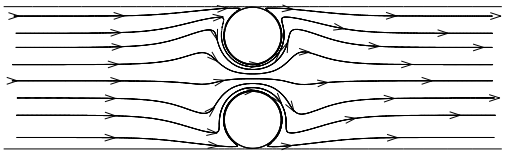

(a) ε*=0.01

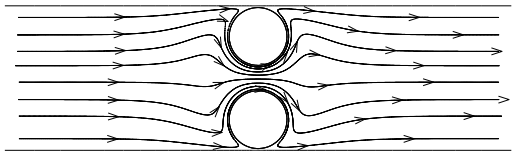

(b) ε*=0.03

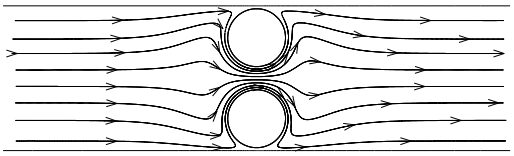

(c) ε*=0.05

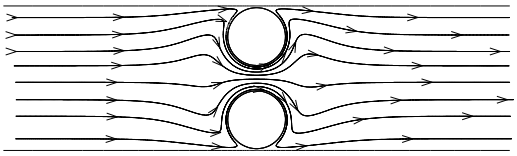

(d) ε*=0.075

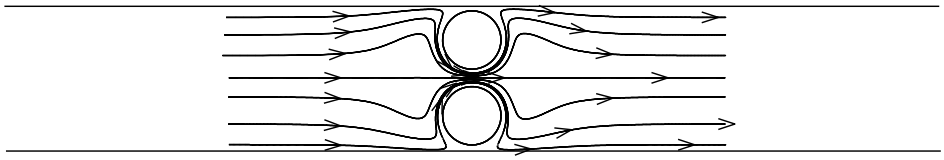

(e) ε*=0.10

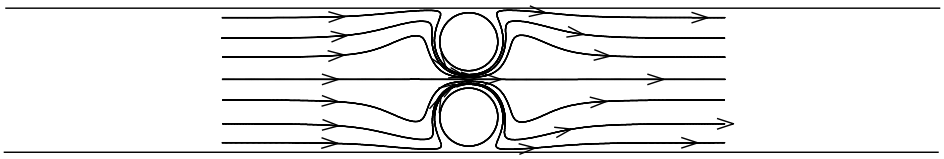

(f) ε*=0.15

Fig. 4.46Streamlines at symmetric plane(Z*=0) for H*=2.5, ε*=0.05, W*=20, Re=1.0, P*=1.0, n=0.785.

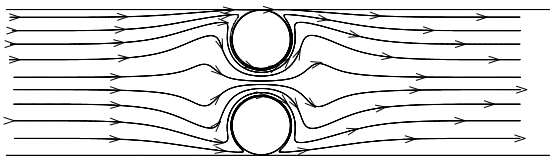

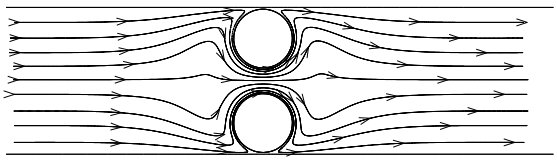

(b) ε*=0.03

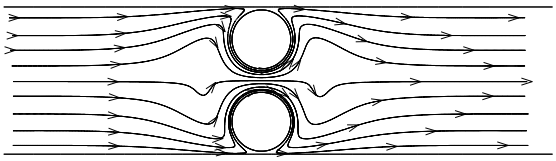

(c) ε*=0.05

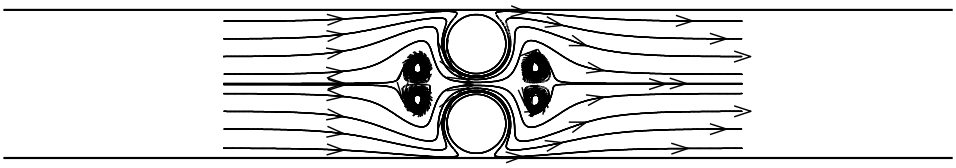

(d) ε*=0.075

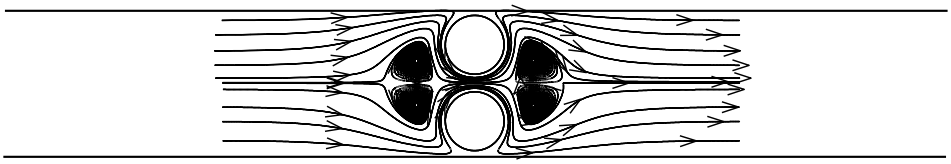

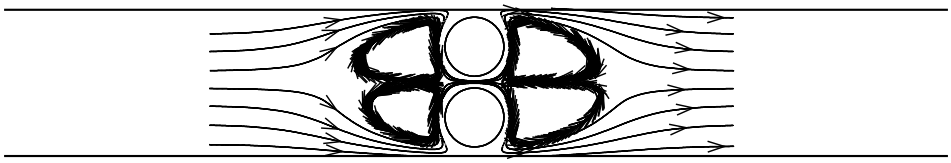

(f) ε*=0.15

Fig. 4.47 Streamlines at symmetric plane(Z*=0) for H*=2.5, ε*=0.05, W*=20, Re=1.0, P*=1.0,n=1.5.

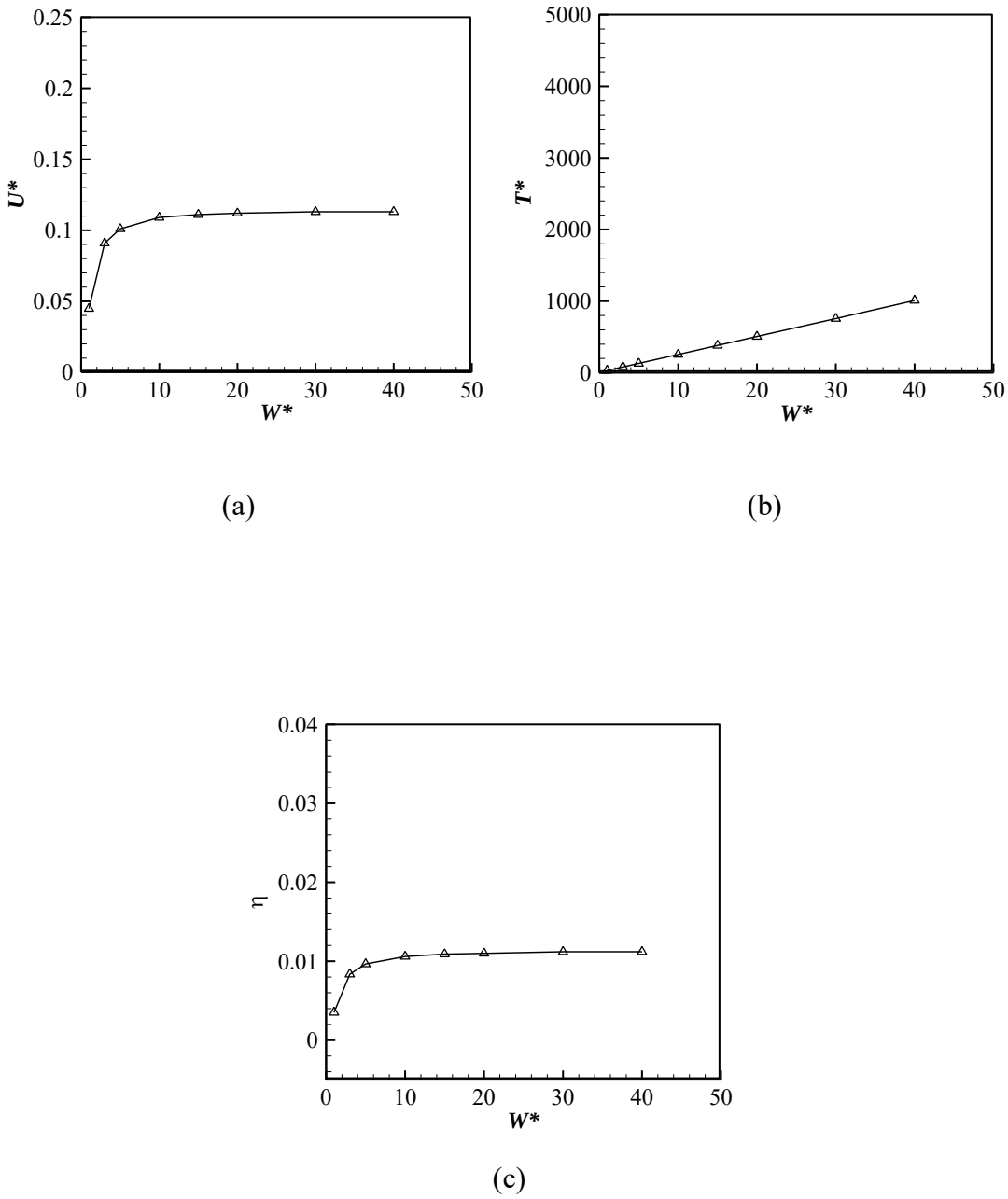

Fig. 4.48 Effect of channel on pump (a) average velocity (b) driving power and (c) efficiency for H*=2.5, ε*=0.05, W*=20, Re=1.0, P*=1.0, n=0.785.

4.4 Transient Flow Behavior inside the Micropump

Besides the steady computations, some unsteady computations have been performed to investigate the initial transient dynamics of micropump operation. Time required for the micropump to reach steady state, the time dependence of the average velocity, the driving power of the rotors and the efficiency at different operating conditions are computed. Flow patterns inside the micropump at different time are also includes in the study

4.4.1 Time Independency Test

The solution of unsteady simulations strongly depends on the selection of times step sizes. Finer step sizes give better accuracy in the numerical results. However, it needs long computational time to reach to the final solution for finer time step sizes. Therefore, a time step independency test is required to find the optimum time step size that will provide sufficient accuracy in the numerical result. In the present numerical analysis, time step independency test has been carried out for four different time step sizes, $\Delta t = 0.0005$ sec, $\Delta t = 0.0001$ sec, $\Delta t = 0.00005$ sec and $\Delta t = 0.00001$ sec. Time dependent average velocity, driving power and efficiency are presented in Fig. 4.49for determining the independency of the solution on time step sizes. In all figures, it is seen that no significant variation occurs in their corresponding parameter when $\Delta t \leq 0.0001$ sec except a deviation up to $t^* = 0.012$ has been found in Fig. 4.49 (b) in case of driving power. However, considering the computational time and consistency of the result in all time step sizes, time step size $\Delta t = 0.0001$ sec has been selected for the present numerical analysis.

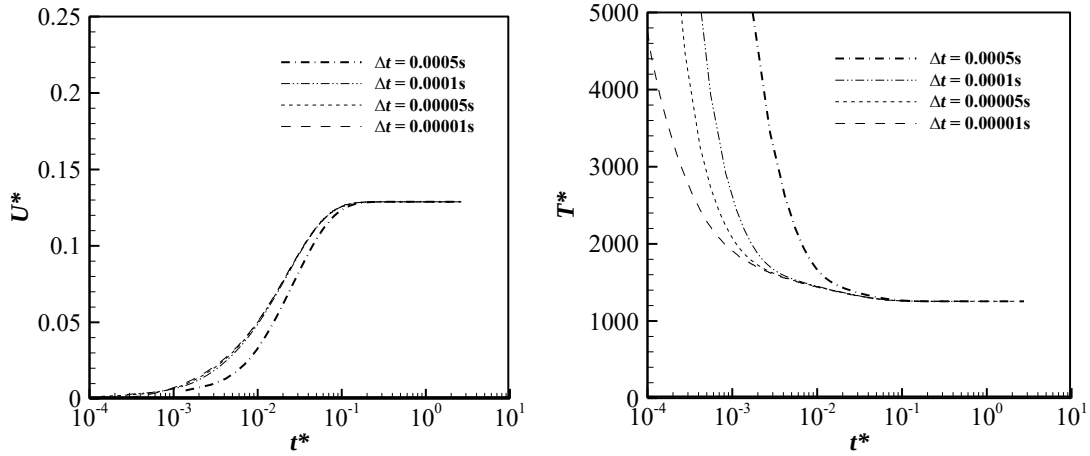

(a) (b)

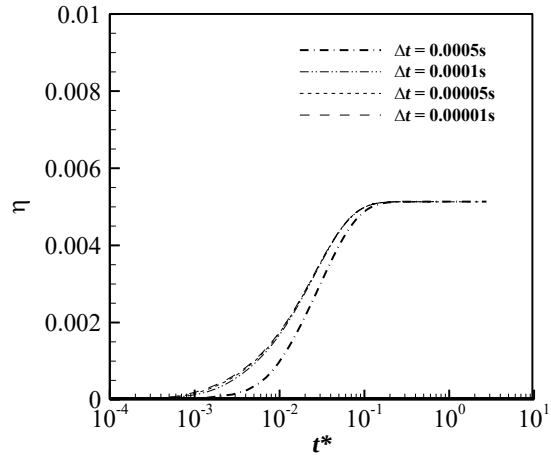

(c)

Fig. 4.49 Variation of pump (a) average velocity (b) driving power and (c) efficiency with time for different values of time step **Δt** and H*=2.5, W*=20, Re=1.0, P*=1.0, n=1.0

4.4.2 Transient Performance of the Viscous Micropump

Fig. 4.50illustrates the startup performance of viscous micropump at different P*. It is seen that at particular flow condition the pump requires a finite time to reach the steady state flow rate. Because, the energy in fluid layers adjacent to the cylinder are transmitted through a large number of fluid layers, which require a definite time to achieve the steady state. Therefore, it results in very low average velocity at the beginning which gradually increases with time shown in Fig. 4.50(a). Again, initially due to presence of high velocity gradient, the driving power requirement shown in Fig. 4.50(b) is higher, which gradually decreases with time. Therefore, the efficiency of pump increases until the steady state flow is obtained. Different cases of simulated results are also presented by varying P* in Fig. 4.50 or by varying Re in Fig. 4.51 to understand the unsteady performance of micropump.

To visualize the scenario of unsteady effect in flow field, the development of flow inside the micropump with time is shown in Fig. 4.52. At the beginning, vortices comparatively large in size start to form around the cylinder as well as both at downstream and upstream side. It is observed that the one pair of vortices forms both at upstream and downstream side and are symmetrical which then with time push to each other and decreases in size. This continues until the flow is stream wise flow. Similarly, a gradual change in X-velocity in contour plot shown in Fig. 4.53 is observed until the flow inside pump is fully developed.

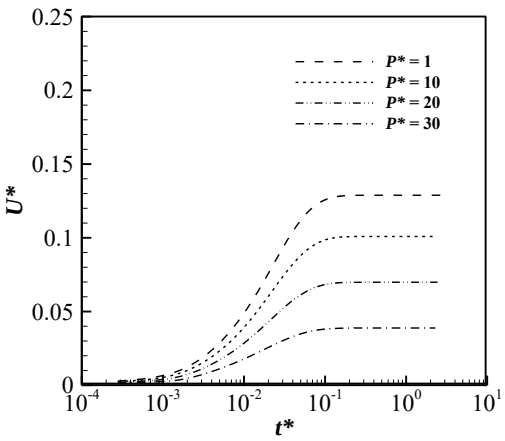

(a)

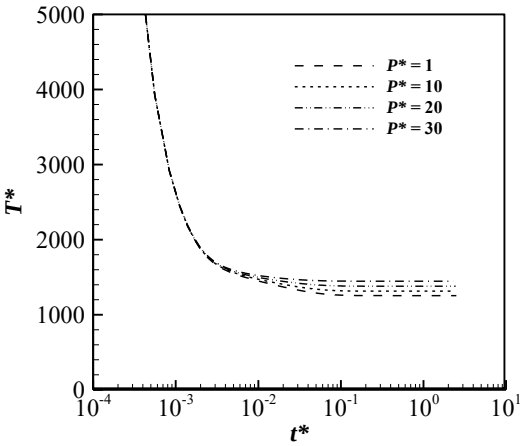

(b)

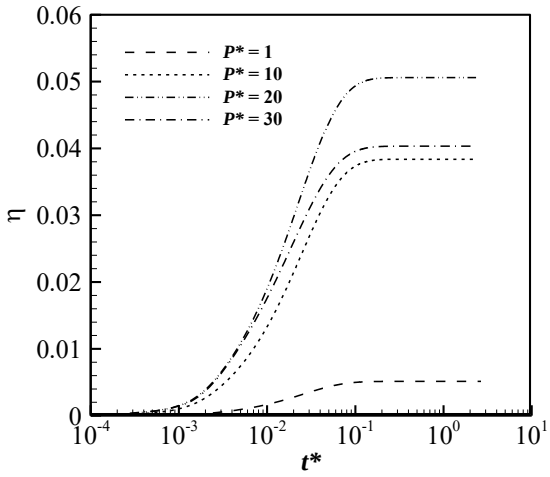

(c)

Fig. 4.50Variation of pump (a) average velocity (b) driving power and (c) efficiency with time for H*=2.5, ε*=0.05, W*=20, Re=1.0, n=1.0

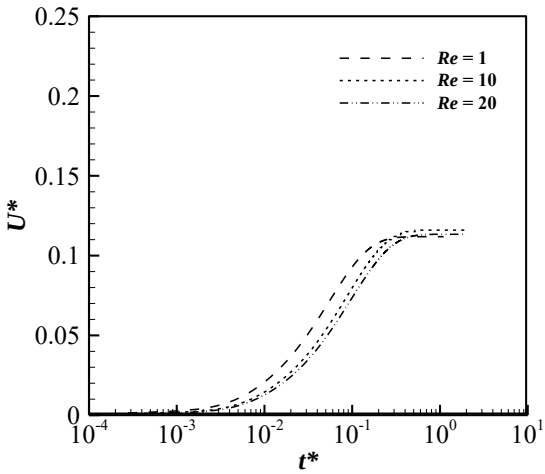

(a)

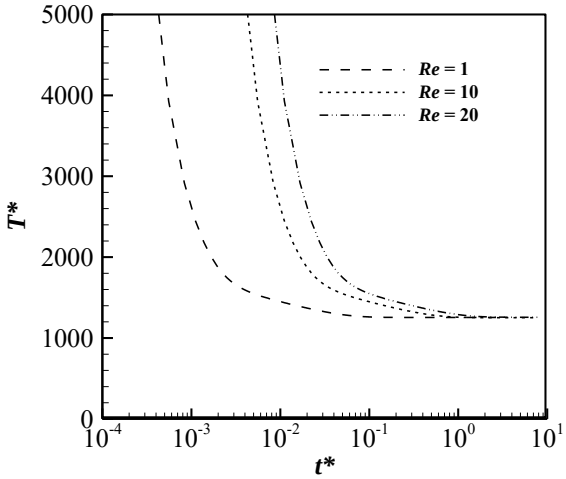

(b)

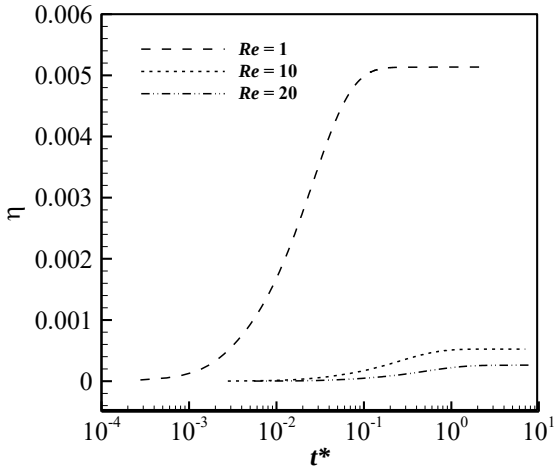

(c)

Fig. 4.51 Variation of pump (a) average velocity (b) driving power and (c) efficiency with time forH*=2.5, ε*=0.05, W*=20, P*=1.0, n=1.0

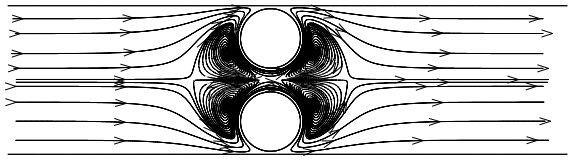

(a) t*=0.0056

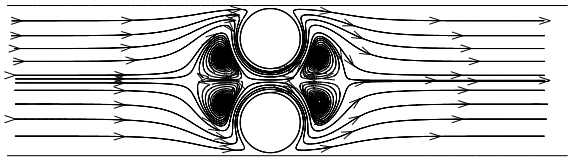

(b) t*=0.0139

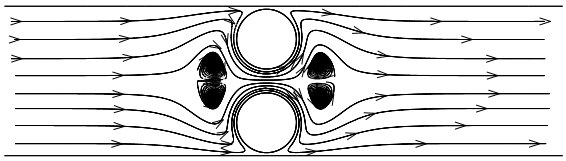

(c) t*=0.0278

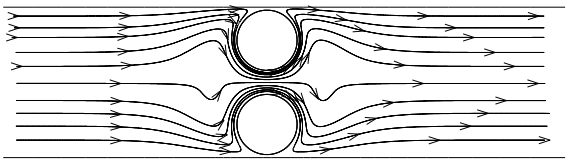

(d) t*=0.0417

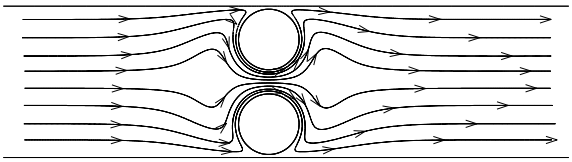

(e) t*=0.0556

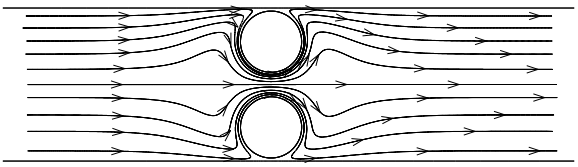

(f) Steady state

Fig .4.52Streamlines with time at Z*=0 (symmetric plane) for H*=2.5, W*=20, P*=1.0, Re=1.0, n=1.0

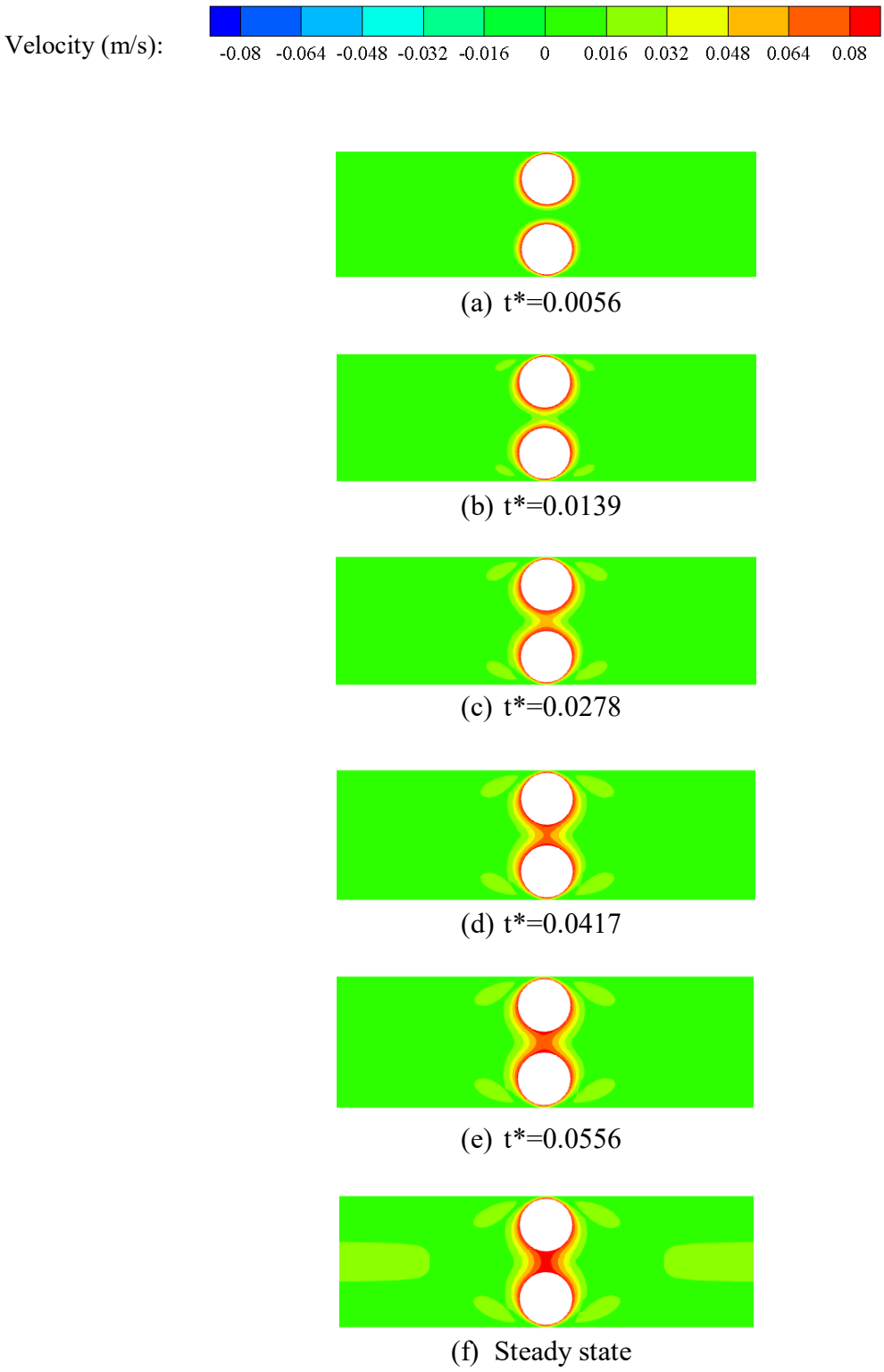

Fig. 4.53X-velocity contour with time at Z*=0 (symmetric plane) for H*=2.5, W*=20, P*=1.0, Re=1.0, n=1.0

4.4.3 Comparison with Steady State Results

Fig. 4.54 shows the variation of average velocity at channel exit with time at different flow condition. It is obvious that after a finite time the flow inside the micropump become steady and there is no signification variation in flow structures. At constant rotor speed Re=1 and at different P* shown in Fig. 4.54 [(a), (b), (c)], the steady state condition is achieved approximately at the same time i.e. $t^* \simeq 0.1$. Whereas at constant P*=1.0 and at different Re shown in Fig. 4.54 [(e), (f), (g)], the time for achieving steady state is higher with Re.

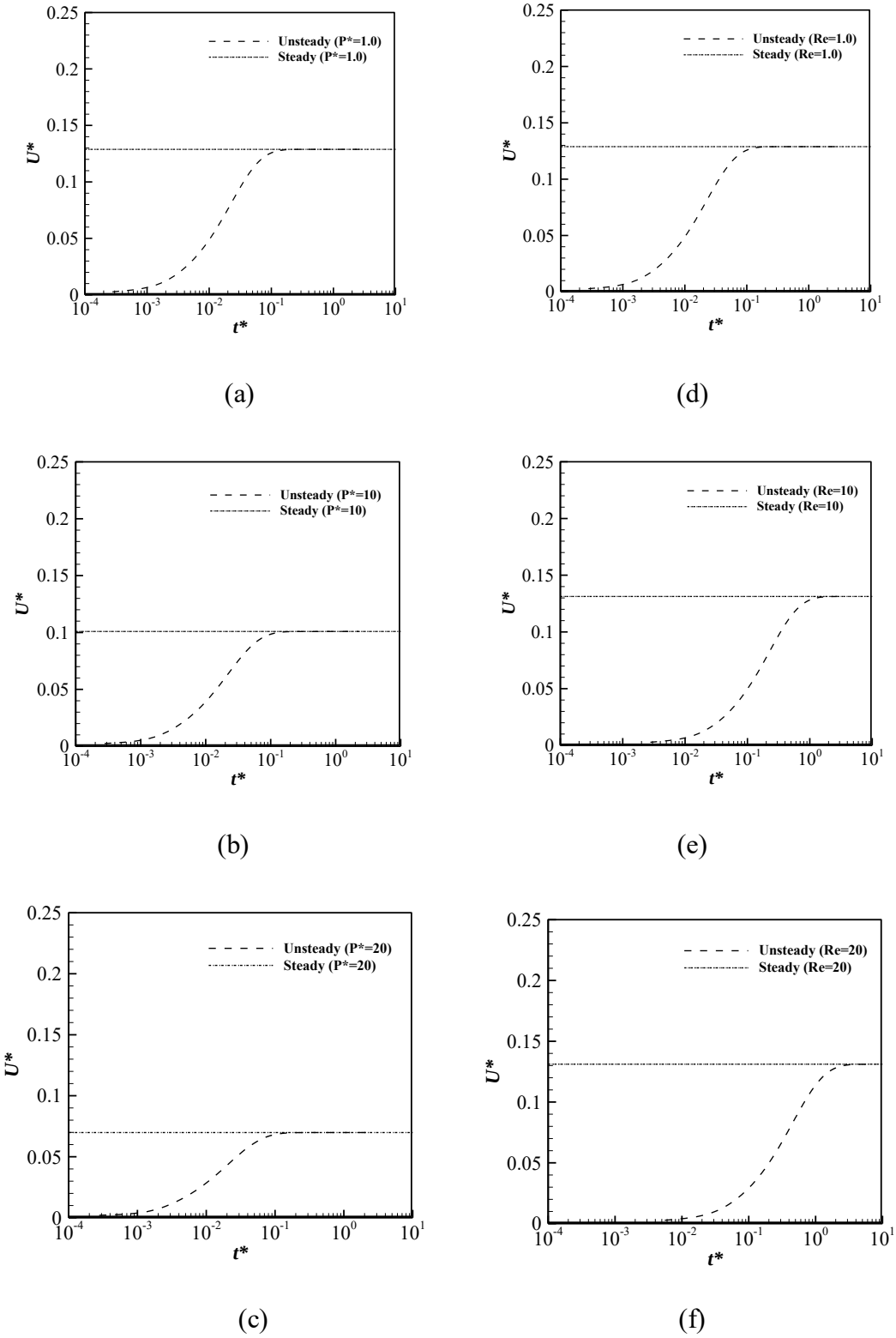

Fig. 4.54Comparisons of steady and unsteady results [(a), (b), (c)] for differentP*, Re=1.0[(e), (f), (g)]for differentRe, P*=1.0 at H*=2.5, ε*=0.05, W*=20, n=1.0

4.5 Transient Behavior Inside the Micropump with Non-Newtonian Fluid (n=0.785)

To investigate the transient performance with non-Newtonian flow, numerical simulations are carried out at different operating conditions by varying Re and P* shown in Fig. 4. 55-Fig. 4.56. It is observed that the trend of the all plots are similar to the case with Newtonian flow except in their respective numerical values of performance parameters. Fig. 4.55 shows the effect on performance at different pump load i.e. P* = 1, 10 and 20. Similarly, Fig. 4.56 shows the effect on pump performance at different Reynolds number i.e. Re = 1, 10 and 20.

To visualize the scenario of unsteady effect on non-Newtonian fluid flow field, the development of flow inside the micropump with time is shown in Fig. 4.57. At the beginning, vortices comparatively large in size start to form around the cylinder as well as both at downstream and upstream side, then with time decreases in size. The formation of flow patterns with time and its gradual change are quite similar to that of Newtonian case. Similarly, a gradual change in X-velocity in contour plot especially between the two rotors region shown in Fig. 4.58 is observed until the flow inside pump is fully developed.

Like Newtonian case, the comparisons between steady and numerical results for non-Newtonian fluid flow for same pump configurations are presented in Fig. 4.59. It is found that time required to reach steady state for the case of n=0.785 at constant Re and at varying P* is $t^* \simeq 0.12$, which is slight higher than the Newtonian case. However, at constant P* and varying Re, the time for achieving steady state is higher with Re.

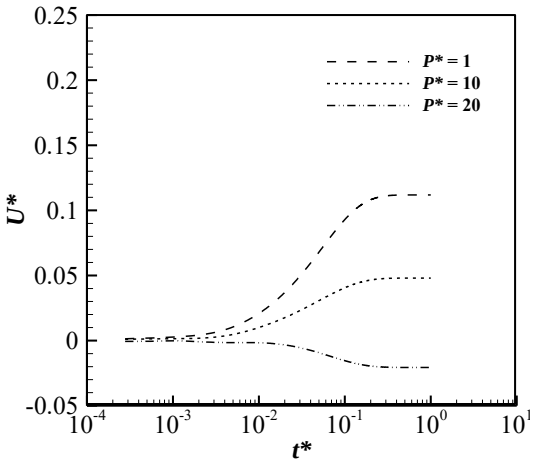

(a)

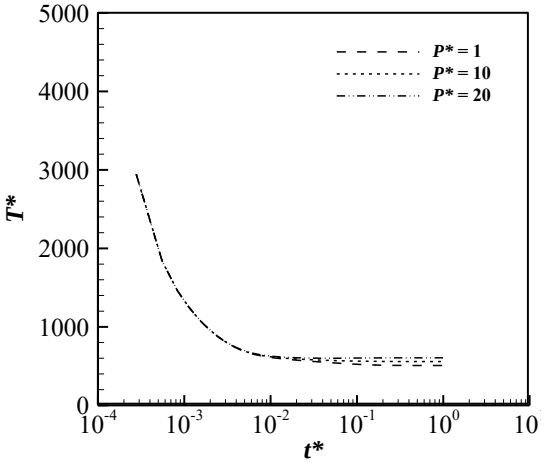

(b)

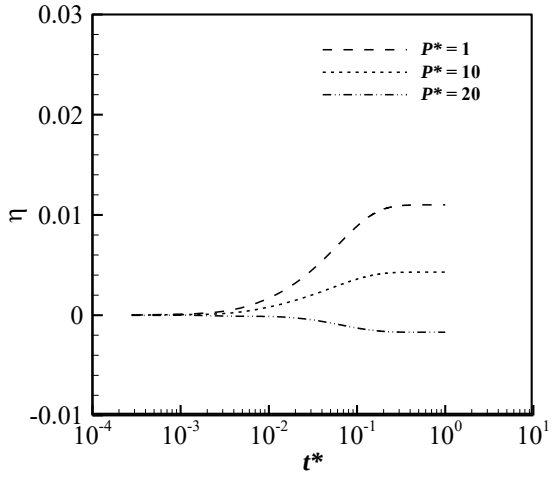

(c)

Fig. 4.55Variation of pump (a) average velocity (b) driving power and (c) efficiency with time for H*=2.5, ε*=0.05, W*=20, Re=1.0, n=0.785

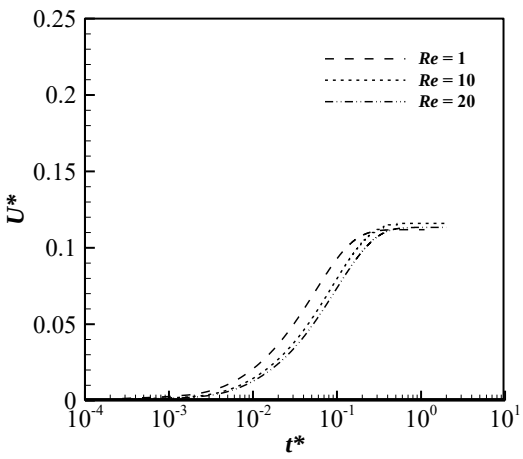

(a)

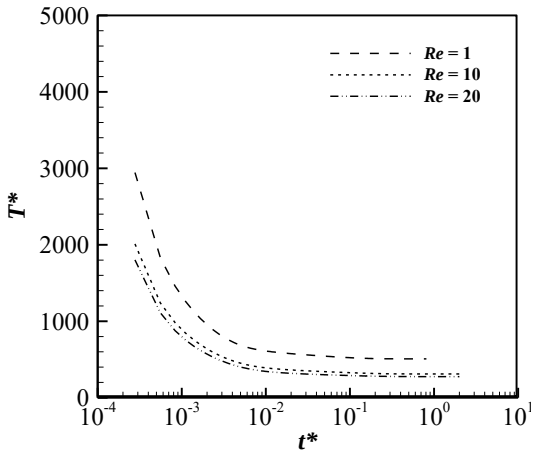

(b)

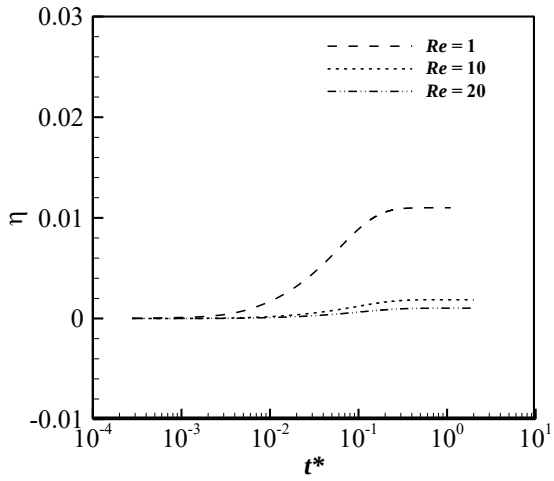

(c)

Fig. 4.56Variation of pump (a) average velocity (b) driving power and (c) efficiency with time for H*=2.5, ε*=0.05, W*=20, P*=1.0, n=0.785

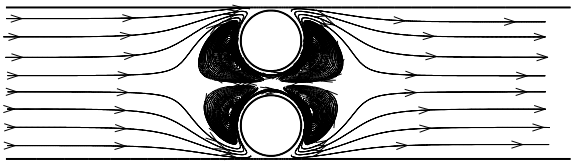

(a) t*=0.0056

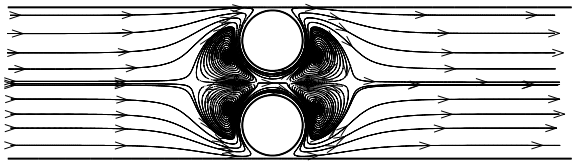

(b) t*=0.0139

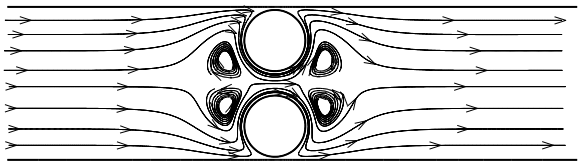

(c) t*=0.0278

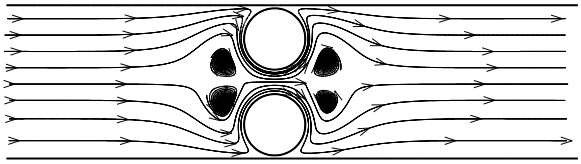

(d) t*=0.0417

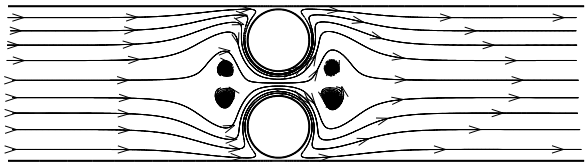

(e) t*=0.0556

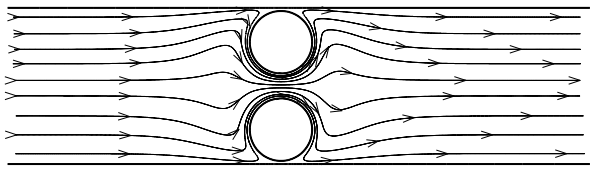

(f) Steady state

Fig .4.57 Streamlines with time at symmetric plane (Z*=0) for H*=2.5, W*=20, P*=1.0, Re=1.0, n=0.785

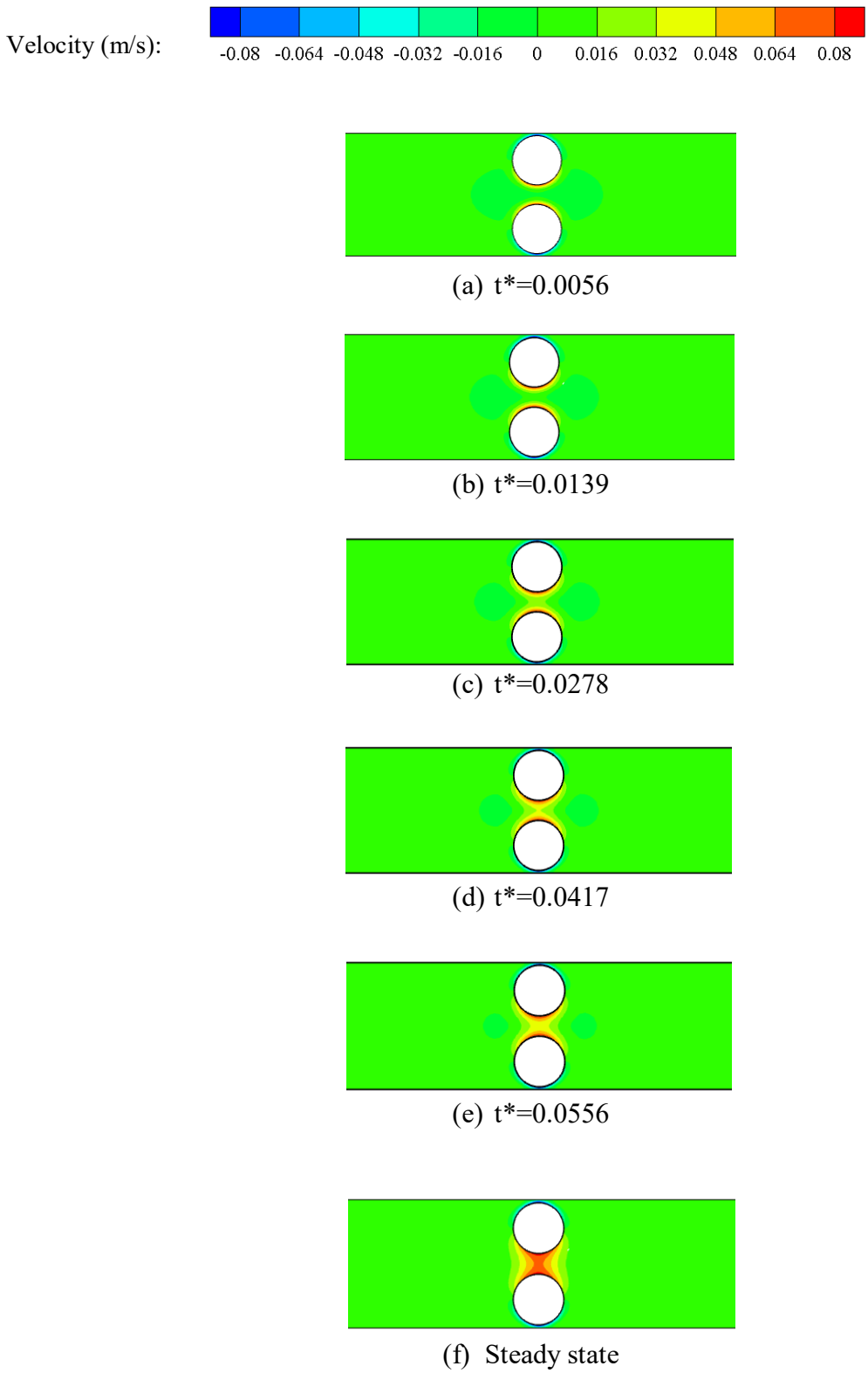

Fig. 4.58X-velocity contour with time at Z*=0 (symmetric plane) for H*=2.5, W*=20, P*=1.0, Re=1.0, n=0.785

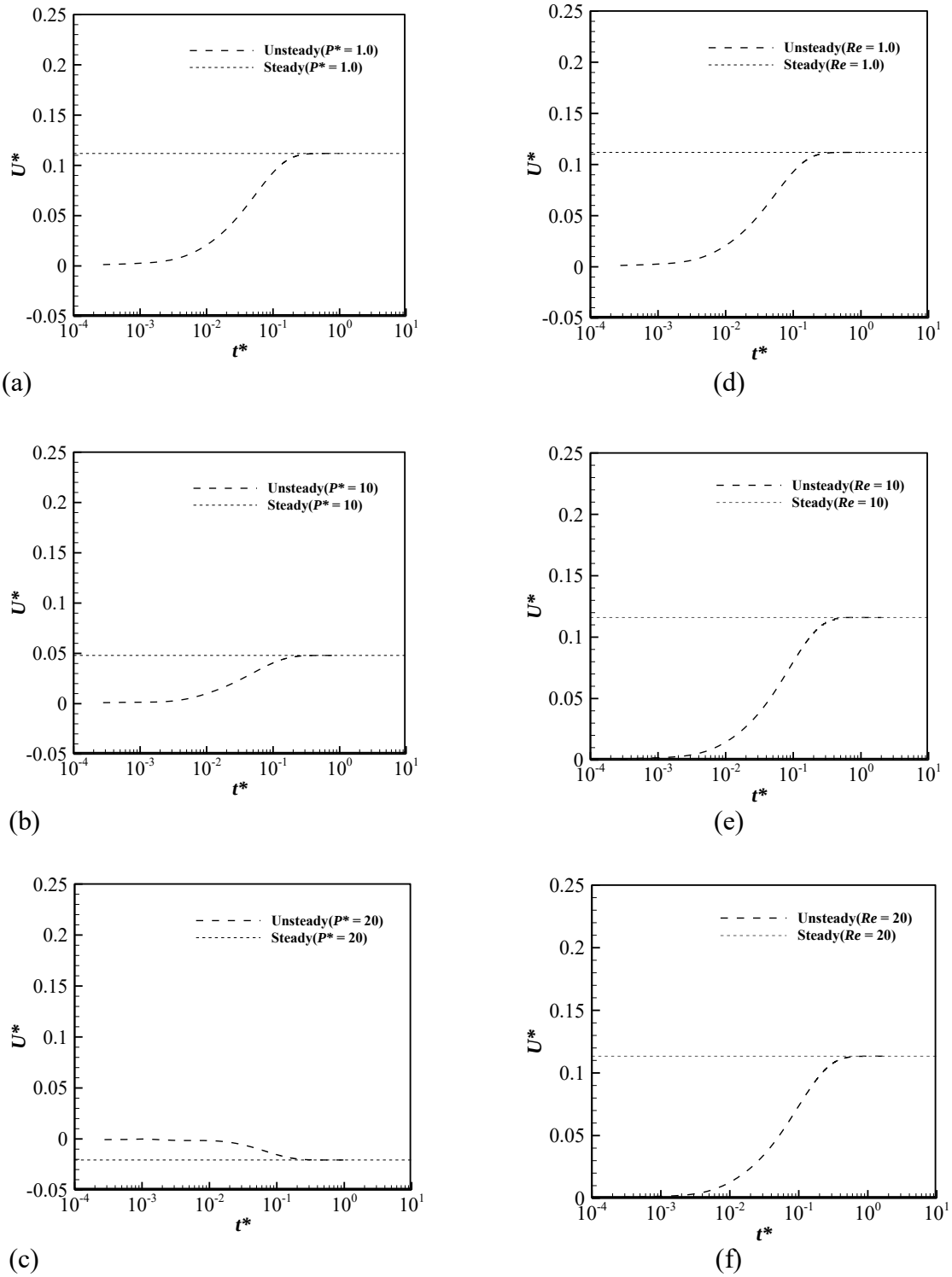

Fig. 4.59Comparisons of steady and unsteady results [(a), (b), (c)] for differentP*, Re=1.0[(e), (f), (g)]for differentRe, P*=1.0 at H*=2.5, ε*=0.05, W*=20, n=0.785.

CHAPTER 5
CONCLUSIONS

In the present study, a micro-scale dual rotor viscous pump has been analyzed in details. Several geometric configurations of micropumps have been studied considering wide range of application. A computational study based on Finite Volume Method (FVM) using 3-D laminar simulation is performed to investigate the performance of a viscous micropump. A channel with two cylinder symmetrically placed on the vertical position is used as the computational geometry. The discretization of the computational model is done using structured multi block mesh. The validation of the present numerical results is done by comparing with available experimental results. After that various flow structures and the effect of different parameters such as channel height (H^*), wall clearance (ε^*), channel width (W*), Reynolds number (Re), and pump load (P^*) on micropump performance are investigated. The unsteady effect on flow dynamics as well as the effect on flow with non-Newtonian flow are also investigated. Flow patterns for different conditions are also obtained. From the analysis, following conclusions can be drawn:

i. The average velocity for a given channel height inside the micro-scale viscous pump linearly decreases with the increase of wall clearance. However, the driving power decreases exponentially with increasing wall clearance. The average velocity inside microscale pump reaches about 18% of the cylinder surface velocity depending on the micropump dimensions and fluid property.

ii. For a given pump configuration at any flow condition, the flow becomes steady after a finite time. Time required to reach steady state for constant rotor speed and varying pump load are approximately same i.e. t*=0.10 but for constant pump load and varying Reynolds number it varies.

iii. The rotor position inside the pump house has significant effect on the flow field which results in different sizes of vortices formed both at downstream and upstream side of the pump.

iv. There is an optimal rotor position inside the pump house for a particular channel height where the pump provides the best performance. For channel height (H*) of 2.1, 2.3, 2.5, 2.7 and 3.0, the respective optimal rotor positions (ε*) are found to be 0.01, 0.02, 0.05, 0.075 and 0.10 for flow conditions of Re=1.0 and P*=1.0.

v. The channel width (W*) i.e. the side wall has significant effect on the pump performance as long as the channel width is 20 times the rotor diameter or less.

vi. There are best operating conditions at which the pump operates efficiently. For example, at H*=2.5, ε*=0.05 and W*=20, the effective flow conditions are: Re=1, P*=20; Re=5, P*=100, Re=10, P*=210 and so on. It is also determined that the efficiency decreases significantly with the increase of Reynolds number due to higher viscous dissipation.

vii. The range of operating pump load is fixed for particular channel height which increases with lower channel height. For example, at H*=2.5, ε*=0.05, W*=20 and Re=5.0, the pump load range is between 0.1 Pa up to 1 KPa or more. The maximum efficiency achieved is 5.5% or may be more depending on the pump dimension and fluid property.

viii. The findings of the optimization results with non-Newtonian flow is quite similar as the results on Newtonian flow. However, a significant variation in performance are found while working with non-Newtonian fluid at different power law indices.

ix. The use of additional rotor on vertical position has provided the higher flow rate as well as the higher efficiency than the single rotor type micropump.

However, based on these results it can be said that the micro-scale viscous micropumps are intended for low flow rate applications where the accuracy in delivering small flow rate is more important than the efficiency of the pump.

The following recommendations can be made for further work:

i. The effect of the rotor shape whether it is square, rectangular or triangular might have effect on the micropump performance or they may achieve better performances in some applications.

ii. In the present study, only the 3-D changes of the channel walls are considered. No 3-D changes to rotor shape or size is investigated although such changes might provide better performance or efficiency of the pump.

iii. The use of additional rotor above two either placed horizontally or vertically, might generate higher flow rate as well as provide better efficiency.

REFERENCES

[1] C. Mousoulis, M. Ochoa, D. Papageorgiou, and B. Ziaie,"A Skin-Contact-Actuated Micropump for Transdermal Drug Delivery", IEEE Transactions on Biomedical Engineering, Vol. 58 (5), pp. 1492-1498, 2011

[2] R. S. Nelson and C. L. Truwit, "Implantable Reservor and System for Delivery of Atherapeutic Agent", United States Patent, Patent No. US 7063691 B2, 2006.

[3] Fraunhofer EMFT, "Cost-effective Micropump for Medical Technology", COMPAMED Magazine, 2015.

[4] https://www.diabetespharmacist.com/2013/03/articles/insulin-pumps/insulin-pumps-equal-flexibility-and-accuracy-for-people-with-diabetes.

[5] https://stanfordhealthcare.org/medical-treatments/l/lvad.html

[6] A.Nisar, Nitin,Afzulpurkar,Banchong,Mahaisavariya, and AdisornTuantranont,"MEMS-based Micropumps in Drug Delivery and Biomedical Applications", Sensors and Actuators B: Chemical, Vol. 130(2), pp. 917-942, 2008.

[7] D. J. Laser and J. G. Santiago, "A Review of Micropumps", Journal of Micromachines and Microengineering, Vol. 14, pp. R35-R64, 2004.

[8] P. Woias, "Micropumps-Past, Progress and Future Prospects", Sensors and Actuators B: Chemical, Vol. 105(1), pp. 28-38, 2005.

[9] B. D. Iverson and S. V. Garimella, "Recent Advances in Microscale Pumping Technologies: A Review and Evaluation", Microfluidics and Nanofluidics, Vol. 5(2), pp. 145-174, 2008.

[10] D. Blanchard P. Ligrani, "Comparisons of Different Viscous Pumps based on PhysicalFow Behavior", Sensors and Actuators A, 126, 83–92, 2006.

[11] Q. Cui, C. Liu and Xuan F. Zha, "Study on a Piezoelectric Micropump for the Controlled Drug Delivery System", Microfluidics and Nanofluidics, Vol. 3(4), pp. 377-390, 2006.

[12] L. S. Jang and W. H. Kan, "Peristaltic Piezoelectric Micropump System for Biomedical Applications." Biomed Microdevices, Vol. 9(4), pp. 619-626, 2007.

[13] L. S. Jang, Y.J. Li, S. J. Lin, Y. Hsu, W. Yao, M. Tsai, Ching-Cheng Hou, "A Stand-alone Peristaltic Micropump Based on Piezoelectric Actuation." Biomed Microdevices, Vol. 9(2), pp.185-194, 2007.

[14] H. K. Ma, Y. T. Li, H. C. Su, W. F. Luo, T. J. Pan, F. M. Fang, and S. W. Hsu, "Development and Application of One-Sided Piezoelectric Actuating Micropump", Smart Materials Research, Vol. 2013, Article ID 498019, 2013.

[15] W.J. Spencer,"An Electronically Controlled Piezoelectric Insulin Pump and Valves" IEEE Transactions on Sonics and Ultrasonics, Vol. 25 (3) , pp. 153-156, 1978.

[16] T. Zhang and Q. M. Wang, "Performance Evaluation of a Valveless Micropump Driven by a Ring-Type Piezoelectric Actuator", IEEE Transactions of Ultrasonics, Feroelectrics and Frequency Control, Vol. 53 (2), pp. 463 – 473, 2006.

[17] K. S. Lee,B. Kim and M. A. Shannon , "An Electrostatically Driven Valve-less Peristaltic Micropump with a Stepwise Chamber", Sensors and Actuators A: Physical, Vol. 187, pp. 183-189, 2012.

[18] M. Sen, D. Wajerski, and M. Gad-el-Hak, "A Novel Pump for MEMS Applications", Journal of Fluids Engineering, Vol. 118, pp. 624–627, 1996.

[19] M. Abdelgawad, I. Hassan, and N. Esmail, "Microscale Thermophysical Engineering", Vol. 8 pp. 361–381, 2004.

[20] H. A. Arafa and T. A. Osman, "Viscous Pumps: Comparative Assessment of Effectiveness", Proc. Inst. Mech. Eng., PartJ: J. Eng. Tribol. Vol. 217, pp. 167–174, 2003.

[21] D. Blanchard P. Ligrani and B. Gale, "Miniature Single-disk Viscous Pump (single DVP) Performance Characterization", Journal of fluid engineering, Vol. 128, pp. 602-610, 2006.

[22] Y. Sato and J.D. Knight, "Performance Characteristics of Shrouded Rayleigh Step and Spiral Groove Viscous Pumps", ASME Trans. J. Tribol, Vol. 114, pp. 499–506, 2012.

[23] S.H. Winoto, "Performance of a Viscous Pump with Radial Pumping Grooves at Low Speeds", Tribol. Trans. Vol. 42, pp. 425–428, 1999.

[24] S.H. Winoto and K. Yohanand, “Analysis and Test of a Viscous Pump with Radial Pumping Grooves”, Tribol. Trans. Vol. 37, pp. 691–700, 1994.

[25] I. Etsion and R. Yaier, “Performance Analysis of a New Concept Viscous Pump”, ASME Trans. J. Tribol. Vol. 110, pp. 93–99, 1998.

[26] I. Green, M. Mainland and I. Etsion, “Experimental Investigation of a New Concept Viscous Pump”, ASME Trans. J. Tribol. Vol. 113, pp.725–728, 1991.

[27] E. Stemme and G. Stemme, “Valveless Diffuser/Nozzle-Based Fluid Pump”, Sensors and Actuators A: Physical, Vol. 39, pp. 159–167, 1993.

[28] S. Erik and S. Goran, “Valveless Diffuser/Nozzle-Based Fluid Pump”, Sensors and Actuators A: Physical, Vol. 39, pp. 159–167, 1993.

[29] M. C. Sharatchandra, M. Sen, and M. Gad-el-Hak, “Navier-Stokes Simulation of a Novel Viscous Pump”, Transaction of the ASME, Journal of Fluids Engineering, Vol. 119, pp. 372–382, 1997.

[30] M. C. Sharatchandra, M. Sen, and M. Gad-el-Hak, “Thermal Aspects of a Novel Viscous Pump”, Journal of Heat Transfer, Vol. 120, pp. 99–107, 1998.

[31] M. Abdelgawad, I. Hassan, and N. Esmail, “Transient Behavior of the Viscous Micropump,” Microscale Thermophysics Eng. Vol. 8(4), pp. 361–381, 2004.

[32] A.K. da Silva, M.H. Kobayashi, C.F.M. Coimbra, “ Optimal Theoretical Design of 2-D Micro-sclae Viscous Pumps for Maximum Mass Flow Rate and Minimum Power Consumption”, International Journal of Heat and Fluid Flow Vol. 28, pp. 526–536, 2007.

[33] D. J. Kang, “Effects of Channel Curvature on the Performance of Viscous Micro-pumps”, Journal of Mechanical Science and Technology, Vol. 28 (9), pp. 3733~3740, 2014.

[34] L. Jianfeng and D. Jing, “Flow Dynamical Behaviors and Characteristics of Aligned and Staggered Viscous Pumps”, International Journal of Heat and Mass Transfer, Vol. 53, 2092-2099, 2010.

[35] J. Lu and J. Ding, “Flow Dynamical Behaviors and Characteristics of Aligned and Staggered Viscous Pumps”, International journal of heat and mass transfer, Vol. 53, pp. 2092-2099, 2010.

[36] J. Lu, D. Jing, D. Yang and X. Yang , "Steady Dynamical Behaviors of Novel Viscous Pump with Groove under Rotor", International journal of heat and mass transfer, Vol. 53, pp. 2092-2099, 2010.

[37] P. Phutthavong and I. Hassan, "Transient Performance of Flow over a Rotating Object Placed Eccentrically inside a Micro Channel-Numerical Study", Microfuidics and Nanoluidics, Vol. 1(1), pp. 71–85, 2004.

[38] K. Yokota, K. Sato and M. Itoh, "Model Experiment, Numerical Simulation and Theoretical Analysis on the Characteristics of a Viscous Micropump using a Cylindrical Rotor in a Rectangular Duct", JSME International Journal Series B, Vol. 49, pp. 393–400, 2006.

[39] A. Martín-Alcántara, E. Sanmiguel-Rojas, and R. Fernandez-Feria, "On the Development of Lift and Drag in a Rotating and Translating cylinder", Journal of Fluids and Structures, Vol. 54, pp. 868–885, 2012.

[40] A. Rao, M. C. Thompson, T. Leweke, and K. Hourigan, "Flow Past a Rotating Cylinder Translating at Different Gap Heights along a Wall", Journal of Fluids and Structures, Vol. 57, pp. 314–330, 2015.

[41] D. Decourtye, M. Sen, and M. Gad-el-Hak, "Analysis of Viscous Micropumps and Microturbines", International Journal of CFD, Vol. 10, pp. 13–25, 1998.

[42] H. El-Sadi, N. Esmail and I. Hassan "Numerical Modelling of Non-Newtonian Flow in Viscous Micropump", Journal of the Society of Rheology, Vol. 36 (1), pp. 51-58, 2007.

[43] A. K. da Silva, M. H. Kobayashi and C. F. M. Coimbra, "Optimal Design of Non-Newtonian, Micro-scale Viscous Pumps for Biomedical Devices", Biotechnology and Bioengineering, Vol. 96, No. 1, 2007.

[44] M. Abdelgawad, I. Hasan, N. Esmail and P. Phuttavong, "Numerical Investigation of Multistage Viscous Micropump Configurations", Journal of Fluid Engineering, Vol. 127, pp. 734-742, 2005.

[45] F. J. Walburn and D. J. Schneck, "A Constitutive Equation for the Whole Human Blood", Biorheology, Vol. 13, pp. 201–210, 1976.

[46] R. B. Bird, W. E. Stewart and E. N. Lightfoot, "Transport Phenomena", NewYork: John Wiley & Sons, 2001.

[47] ANSYS Inc., Canonsburg, PA, USA (www.ansys.com).

APPENDICES

Appendix-A: Design of Numerical Experiments

Geometric Parameter			Flow Parameter		Remarks
H* = (2h/d)	**W* = (w/d)**	**ε* = (ε/d)**	**Re**	**P***	
1.11, 1.32, 1.56, 1.78, 2.11, 2.67, 3.22, 3.78	16.926	0.025	0.5	0.5	Exp. Validation (single rotor) of Sen et. al. [18] work
1.5	---------	0.0125	1	0	2D Numerical (single rotor) validation of Abdelgawad [31] work
2.1	20	0.00625, 0.01, 0.025	1	1	**ε^*_{opt}= 0.01**
2.3	20	0.00625, 0.01, 0.02, 0.03, 0.05, 0.075	1	1	**ε^*_{opt}= 0.02**
2.5	20	0.00625, 0.01, 0.02, 0.03, 0.05, 0.075, 0.1, 0.15	1	1	**ε^*_{opt}= 0.05**
2.7	20	0.00625, 0.01, 0.02, 0.03, 0.05, 0.075, 0.1, 0.15	1	1	**ε^*_{opt}= 0.075**
3.0	20	0.00625, 0.01, 0.02, 0.03, 0.05, 0.075, 0.1, 0.15, .2, .225	1	1	**ε^*_{opt}= 0.1**
2.5	1, 3, 5, 10, 15, 20, 30, 40	0.05	1	1	**W^*_{opt}= 20**
2.1	20	0.01	1	0,1,10,20, 50,70, 90,120,150	To check **P*** effect
2.3	20	0.02	1	0,1,10,20, 30,40,	To check **P*** effect

				50,60,70, 80,90	
2.5	20	0.05	1	0,1, 5, 10,15,20 25, 30, 35, 40, 42	To check **P*** effect
2.7	20	0.075	1	0,1,5,10,1 5,20,25	To check **P*** effect
3.0	20	0.10	1	0,1,3,5,7, 10,12,14	To check **P*** effect
2.5	20	0.05	1,5,10, 20, 50, 70, 100	1	To check **Re** effect
2.5	20	0.01, 0.02, 0.03, 0.05, 0.075, 0.1, 0.15	1	1	To check the effect of power law index**, n (0.785, 1.0, 1.5)** for non-Newtonian fluids
2.5	1, 3, 5, 10, 15, 20, 30, 40	0.05	1	1	To check **W*** effect for non-Newtonian fluid (n=0.785)
2.5	20	0.05	1	1,10,20,3 0	Transient study to check **P*** effect (n=1.0)
2.5	20	0.05	1,10,20	1	Transient study to check **Re** effect (n=1.0)
2.5	20	0.05	1	1,10,20,3 0	Transient study to check **P*** effect (n=0.785)
2.5	20	0.05	1,10,20	1	Transient study to check **Re** effect (n=0.785)

Appendix-B: Computational Fluid Dynamics (CFD)

Fluid dynamics is a sub-discipline of fluid mechanics which deals with the motion of fluids (liquids and gases), induced by external forces. Fluid flows are governed by partial differential equations (PDE) which represent conservation laws for the mass, momentum, and energy. Computational Fluid Dynamics (CFD) is the discipline of discretizing these PDE and solving those using computers.

Computational fluid dynamics is the use of applied mathematics, physics and computational software to visualize how a gas or liquid flows as well as how the gas or liquid affects objects as it flows past. It is based on the Navier-Stokes equations which describe how the velocity, pressure, temperature, and density of a moving fluid are related. So, we can say that it constitutes a relatively new approach in the philosophical study and development of the whole discipline of fluid dynamics. The advent of the high speed digital computer combined with the development of accurate numerical algorithms for solving physical problems on these computers has revolutionized the way we practice fluid dynamics today. Computational fluid dynamics is today an equal partner with pure theory and pure experiment in the analysis and solution of fluid dynamics problems. There is no doubt that computational fluid dynamics will continue to play this role indefinitely. Many commercial solvers, e.g., ANSYS (www.ansys.com) or COMSOL (www.comsol.com), implement one or several of these tools. They form the backbone of many solutions to problems in fluid mechanics and adjacent fields that cannot be solved analytically and which require numerical solutions.

Applications of CFD

Computational Fluid Dynamics (CFD) is used both for fundamental research, and Industrial research and development. In most industries, it is an essential part of the design cycle. Industries like Aerospace, automotive, chemical, power and bio-medical depend heavily on CFD for design, analysis, and even for service and maintenance of Mechatronic systems.

However, CFD is very useful tool in a wide variety of applications and here we note a few to give you an idea of its use in industry.

i. Electronics: For design and analysis of cooling system.
ii. Turbo machinery: For design and analysis of pumps, compressors, fans, blowers, turbines nozzle and diffusers.
iii. Power and Energy: For design and analysis of thermal, nuclear and hydro power plants. Construction: For design and analysis of dams, spillways, canals, HVAC systems of buildings.
iv. Hydraulics: For construction machinery like excavators, large automotive, aerospace and marine- aerodynamic design of vehicles, combustion modelling, performance of components like turbochargers, propellers, and cooling fans etc.
v. Biomedical- Design of medical equipment like stents, blood flow through veins and arteries, pathology.
vi. Sports- Evaluating performance of athletes, design of high performance gear like swimsuit and helmets.

CFD Analysis Process

The general process for performing a CFD analysis is outlined below so as to provide a reference for understanding the various aspects of a CFD simulation. The process includes:

i. Formulate the Flow Problem
ii. Model the Geometry and Flow Domain
iii. Establish the Boundary and Initial Conditions
iv. Generate the Grid
v. Establish the Simulation Strategy
vi. Establish the Input Parameters and Files
vii. Perform the Simulation
viii. Monitor the Simulation for Completion
ix. Post-process the Simulation to get the Results
x. Make Comparisons of the Results
xi. Repeat the Process to Examine Sensitivities

xii. Document

The above processes are categorized into three steps:

a. Pre Processing: This step consists of defining a geometry to define our domain of interest. The domain of interest is then divided into segments, called as mesh generation step and the problem is set-up defining the boundary conditions. Gambit, Gridgen, CFD-GEOM, ANSYS Workbench Environment & Modules, ANSYS ICEM CFD, TGrid etc., are some of the popular pre-processing softwares.

b. Solver: Once the problem is set-up defining the boundary conditions we solve it with the software on the computer, (can also be done by hand-calculations, but would take long time). We have different popular commercial softwares available for this like Star-CD and Star CCM+ (CD-Adapco), FLUENT and CFX (ANSYS, Inc.), GASP (Aerosoft, Inc.), CFD++ (Metacomp Technologies) etc. Also there are free to use softwares like OpenFOAM, CFL3D, Typhon, OVERFLOW, Wind-US etc., all with different capabilities. These softwares are capable of solving the equations at every probe-point defined during the mesh generation step and also we can include additional models as required by the physics. The numerical methods are also defined at the stage and we solve the whole problem.

c. Post-processing: Once we get the results as values at our probe points we analyze them by means of color plots, contour plots, and appropriate graphical representationsand can generate reports. Tecplot 360, EnSight, FieldView, ParaView, ANSYS CFD-Post etc., are some of the popular post processing softwares.

Fundamental Equations

The governing equation for the present study is the Continuity Equation (Conservation of Mass) and Navier-Stokes Equation (Conservation of Momentum) for incompressible (density, ρ is constant) flow.

A. Conservation of mass

For 3-D flow,

$$\frac{1}{\rho}\frac{\partial \rho}{\partial t} + \frac{\partial (u)}{\partial x} + \frac{\partial (v)}{\partial y} + \frac{\partial (w)}{\partial z} = 0$$

B. Conservation of momentum

For 3-D flow,

$$\rho\left(\frac{\partial(u)}{\partial t} + u\frac{\partial(u)}{\partial x} + v\frac{\partial(u)}{\partial y} + w\frac{\partial(u)}{\partial z}\right) + \frac{\partial(p)}{\partial x} = \mu\left(\frac{\partial^2 u}{\partial x^2} + \frac{\partial^2 u}{\partial y^2} + \frac{\partial^2 u}{\partial z^2}\right)$$

$$\rho\left(\frac{\partial(v)}{\partial t} + u\frac{\partial(v)}{\partial x} + v\frac{\partial(v)}{\partial y} + w\frac{\partial(v)}{\partial z}\right) + \frac{\partial(p)}{\partial y} = \mu\left(\frac{\partial^2 v}{\partial x^2} + \frac{\partial^2 v}{\partial y^2} + \frac{\partial^2 v}{\partial z^2}\right)$$

$$\rho\left(\frac{\partial(w)}{\partial t} + u\frac{\partial(w)}{\partial x} + v\frac{\partial(w)}{\partial y} + w\frac{\partial(w)}{\partial z}\right) + \frac{\partial(p)}{\partial z} = \mu\left(\frac{\partial^2 w}{\partial x^2} + \frac{\partial^2 w}{\partial y^2} + \frac{\partial^2 w}{\partial z^2}\right)$$

Discretization Method

The strategy of discretization is to replace the continuous problem domain with a discrete domain using a grid. In the continuous domain, each flow variable is defined at every point in the domain. For instance, the pressure p in the continuous 1D domain shown in the Fig. A-1 would be given as

$$p = p\,(x),\ 0 < x < 1$$

In the discrete domain, each flow variable is defined only at some the definite grid points. So, in the discrete domain shown below, the pressure would be defined only at the N grid points.

$P_i = p\,(x_i), i = 1, 2. . . , N$

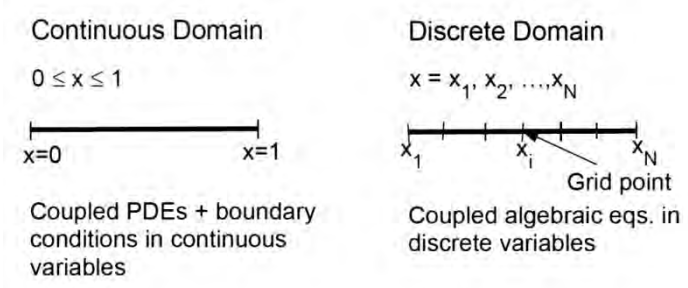

Fig. A-1 Continuous domain and discontinuous domain

In a CFD solution, one would directly solve for the relevant flow variables only at the grid points. The values at other locations are determined by interpolating the values at the grid points.

The governing partial differential equations and boundary conditions are defined in terms of the continuous variables p, V, etc. One can approximate these in the discrete domain in terms of the discrete variables p_i, V_i, etc. The discrete system is a large set of coupled, algebraic equations in the discrete variables. Setting up the discrete system and solving it (which is a matrix inversion problem) involves a very large number of repetitive calculations, a task we humans palm over to the digital computer.

This method of deriving the discrete equation using Taylor's series expansions is called the finite-difference method (FDM). However, most commercial CFD codes use the finite volume method(FVM) or finite-element method (FEM), which are better suited for modeling flow past complex geometries. In the present study, ANSYS FLUENT solver has been used which evaluate the solutions of the governing partial differential equations using finite volume method.

Different types of Grid/ Mesh

In the present study, a preprocessor, GAMBIT is used to generate the required grid for the solver. The grid generation is an important consideration in CFD. Grid designates the cells or elements on which the flow is solved.Grid is a discrete representation of the geometry of the problem. The grid has significant impact on

- Rate of convergence
- Solution accuracy
- CPU time required

The accuracy, precision and reliability of the solution entirely depend on the creation of a perfect grids or meshes. During grid generation process, number of grids should be selected carefully both for the perfection and reliability of the solution and the minimization of solution time. A very high number of grids provide good solution but a very high solution time is required. On the other hand, a coarser grid will provide solution quickly but the solution accuracy will not be satisfactory.

Meshing is the procedure of discretizing the domain creating different grid elements. According to the regularity of the mesh structure, mesh can be classified as,

- Structured mesh: the mesh follows a structured *i, j, k* convention.
- Unstructured mesh: no regularity to the mesh.
- Multiblock/Hybrid: the mesh consists of multiple blocks, each of which can be either structured or unstructured.

According to the cell type, mesh can be again categorized as,

1. Tri mesh: mesh consisting entirely of triangular elements.
2. Quad mesh: consists entirely of quadrilateral elements.
3. Hex mesh: consists entirely of hexahedral elements.
4. Tetrahedral mesh: mesh with only tetrahedral elements.
5. Hybrid mesh: mesh with one of the following:
    a. Triangles and quadrilaterals in 2D.
    b. Any combination of tetrahedra, prisms, pyramids in 3D.
    c. Boundary layer mesh: prisms at walls and tetrahedra everywhere else.
    d. Hexcore: hexahedra in centre and other cell types at walls.
6. Polyhedral mesh: consists of arbitrary polyhedra.
7. Non-conformal mesh: mesh in which grid nodes do not match up along an interface.

Discretization Using Finite Volume Method

The Governing equations of this present problem is discretized by finite volume method (FVM) using ANSYS Fluent [47]. Second order scheme is considered to discretize the governing equations in both spatial and temporal directions. Then the discretized equations are solved in a pressure based solver using implicit method.

The finite volume method is a method for representing and evaluating partial differential equations in the form of algebraic equations. Similar to the finite difference method or finite element method, values are calculated at discrete places on a meshed geometry. "Finite volume" refers to the small volume surrounding each node point on a mesh. In the finite volume method, volume integrals in a partial differential equation that contain a divergence term are converted to surface integrals, using the divergence theorem. These terms are then evaluated as fluxes at the surfaces of each finite volume. Because the flux entering a given volume is identical to that leaving the adjacent volume, these methods are conservative. Another advantage of the finite volume method is that it is easily

formulated to allow for unstructured meshes. The method is used in many computational fluid dynamics packages.

The integral conservation equation are written for a discrete volume,

$$\frac{\partial}{\partial x}\iiint U d\Omega + \oint_S \boldsymbol{F}.d\boldsymbol{S} = \iiint Q d\Omega$$

And applied to control volume Ω_J, when the discretized equation associated with U_J is to be defined. This equation can be replaced by the discrete form,

$$\frac{\partial}{\partial x}(U_J \Omega_J) + \sum_{sides}(\boldsymbol{F}.\boldsymbol{S}) = Q_J \Omega_J$$

Where, the sum of the flux terms refers to all the external sides of the control cell Ω_J. This is the general formulation of the finite volume method, and the user has to define, for a selected Ω_J, how to estimate the volume and cell face areas of the control volume Ω_J and how to approximate the fluxes at the faces.
The following constraints on the choice of the choice of the Ω_J volumes for a conservative finite volume method have to be satisfied:

1. The sum should cover the whole domain Ω;
2. Adjacent Ω_J may overlap if each internal surface is common to two volumes;
3. Fluxes along a cell surface have to be computed by formulas independent of the cell in which they are considered.

The first term of equation (3.6) represents the time rate of change of the averaged flow variable over the selected finite volume. In absence of source terms, the finite volume formulation expresses that the variation of the average value U over the time interval Δt is equal to the sum of the fluxes exchanged between neighbouring cells. For stationary flows the numerical solution is obtained as a result of balance of all the fluxes entering the control volume. That is,

$$\sum_{sides}(\boldsymbol{F}.\boldsymbol{S}) = 0$$

Physically, this equation means that the net volume flow into the control volume is zero. Here is a rectangular cell shown below in Fig. A-2.

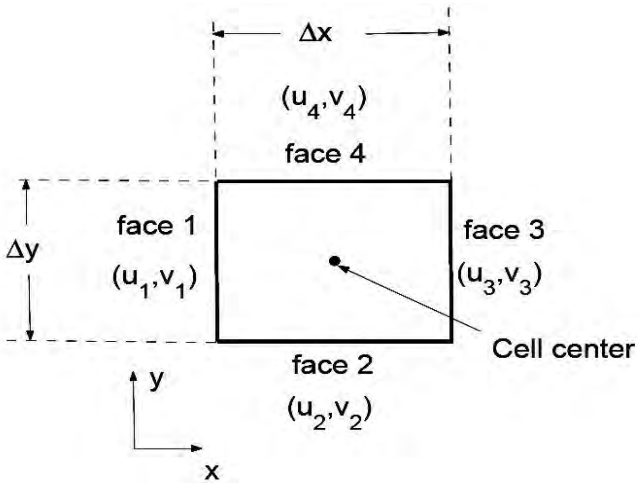

Fig. A-2 Rectangular control volume

The velocity at face is taken to be $V_i = u_i i + v_i j$. Applying the mass conservation equation to the control volume defined by the cell gives,

$$-u_1\Delta y - v_2\Delta x + u_3\Delta y + v_4\Delta x = 0$$

This is the discrete form of the continuity equation for the cell. It is equivalent to summing up the net mass flow into the control volume and setting it to zero. So it ensures that the net mass flow into the cell is zero i.e. that mass is conserved for the cell. Usually, though not always, the values at the cell centres are solved for directly by inverting the discrete system.

The face values u_1, v_2, etc. are obtained by suitably interpolating the cell-center values at adjacent cells. Similarly, one can obtain discrete equations for the conservation of momentum and energy for the cell. One can readily extend these ideas to any general cell shape in 2D or 3D and any conservation equation.The code finds solution such that mass, momentum, energy and other relevant quantities are being conserved for each cell. Also, the code directly solves for values of the flow variables at the cell centres; values at other locations are obtained by suitable interpolation.

Solver Setting

ANSYS FLUENT 14.5 [47] is used for computation. This CFD tool solved the governing integral equations for the conservation of mass and momentum.

Table A-1 Solver setting

Solver	Velocity Formulation	Space	Time
Pressure based	Absolute	3-D	Transient

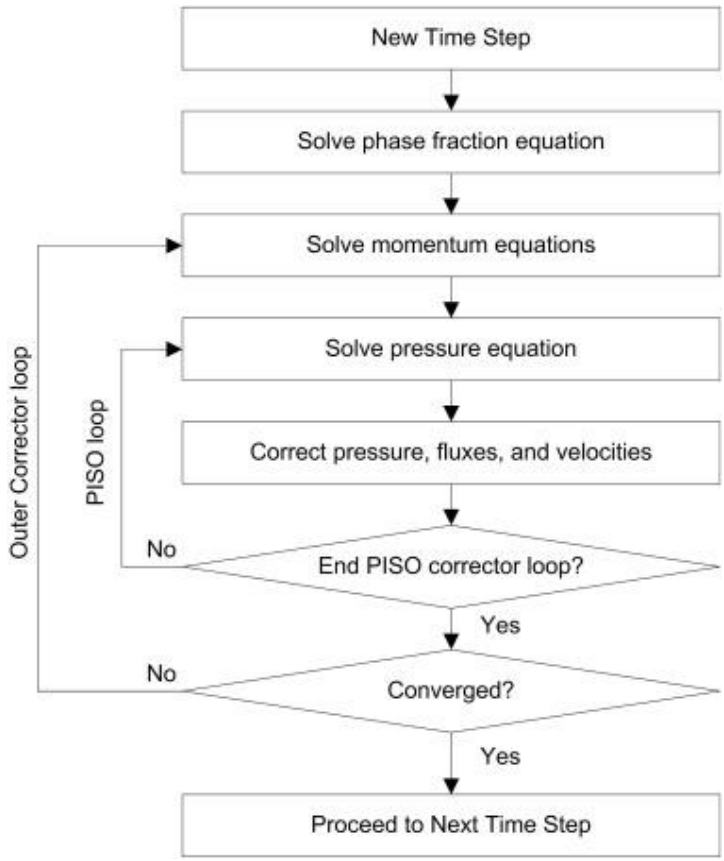

Fig. A-3 Solution procedure

Pressure Based Solver

The pressure-based approached was developed for low-speed incompressible flows. In this method velocity field is obtained from the momentum equations. The pressure field is extracted by solving a pressure or pressure correction equation which is obtained by manipulating continuity and momentum equation. During the numerical analysis we used pressure-based solver. PISO algorithm (Pressure-Implicit with Splitting of Operators) is

used for getting the solution. Block diagram for this method is given in Fig. A-3. It was proposed by Issa in 1986 without iterations and with large time steps and a lesser computing effort. It is an extension of the SIMPLE (semi-implicit method for pressure lined equation) algorithm used in computational fluid dynamics (CFD) to solve the Navier-Stokes equations. PISO is a pressure-velocity calculation procedure for the Navier-Stokes equations developed originally for non-iterative computation of unsteady compressible flow, but it has been adapted successfully to steady-state problems. PISO involves one predictor step and two corrector steps and is designed to satisfy mass conservation using predictor-corrector steps.
The algorithm can be summed up as follows:

Set the boundary conditions.

1. Solve the discretized momentum equation to compute an intermediate velocity field.
2. Compute the mass fluxes at the cells faces.
3. Solve the pressure equation.
4. Correct the mass fluxes at the cell faces.
5. Correct the velocities on the basis of the new pressure field.
6. Update the boundary conditions.
7. Repeat from 3 for the prescribed number of times.
8. Increase the time step and repeat from 1.

Appendix-C: Buckingham's PI Theorem

If there are **n** variables in a problem and these variables contain **m** primary dimensions (for example M, L, T) the equation relating all the variables will have **(n-m)** dimensionless pi groups.

The final equation obtained is in the form of:

$$\phi(\Pi_1, \Pi_2, \Pi_3 .....\Pi_{n-m}) = 0$$
$$or$$
$$\Pi_1 = \phi(\Pi_2, \Pi_3 .....\Pi_{n-m})$$

(1) Back pressure, Δ P = P_{out}- P_{in}

$$\Delta P = f(\rho, \upsilon, d, U)$$

Pressure variation at channel outlet due to rotation of rotor across channel depends on the rotor diameter (d), fluid density(ρ), kinematic viscosity (ν) and cylinder tangential velocity (U).

No. of variables (dependent and independent), n= 5

No. of fundamental dimensions, m = 3 (That is, [M], [L], [T])

By Buckingham's theorem,

No. of dimensionless groups = n-m = 5-3 = 2

Selection of repeater variables: The repeating variables are any set of variables which, by themselves, cannot form a dimensionless group. Number of repeater variables (among independent variables) must equal to the number of basic dimensions.

Repeater variables may be

1. ρ, d, ν
2. ρ, d, U
3. ν, d, U

In present study, repeater variables ρ, d and ν are selected to construct dimensionless groups.

The first Pi term can be expressed as,

$$\Pi_1 = \Delta P \rho^a d^b \nu^c$$

Here, a, b and c are unknown exponents. Since the above expression is to be dimensionless, it follows that,

$$[M^0L^0T^0]=[M^1L^{-1}T^{-2}]\ [ML^{-3}]^a\ [L]^b\ [L^2T^{-1}]^c$$

For,

M: 0=1+a ; a = -1

L: 0=-1-3a+b+2C; b = 2

T: 0=-2-c; c = -2

Therefore, the first Pi term becomes,

$$\Pi_1 = \Delta P \rho^{-1} d^2 \nu^{-2}$$

or

$$\Pi_1 = \frac{\Delta P}{\rho \nu^2 / d^2}$$

The above process is repeated for finding the 2nd Pi term,

$$\Pi_2 = U \rho^a d^b \nu^c$$

Or, $[M^0L^0T^0] = [LT^{-1}]\,[ML^{-3}]^a[L]^b\,[L^2T^{-1}]^c$

For,

M: 0=a ; a = 0

L: 0=1-3a+b+2C; b = 1

T: 0=-1-c; c = -1

$$\Pi_2 = U \rho^0 d^1 \nu^{-1}$$

or

$$\Pi_2 = \frac{Ud}{\nu}$$

The final forms dimensionless groups are

$$\phi(\Pi_1, \Pi_2) = 0$$

$$\text{Or,} \quad \phi\left(\frac{\Delta P}{\rho \nu^2 / d^2}, \frac{Ud}{\nu}\right) = 0$$

However, dimensionless back pressure and Reynolds number can be expressed as,

$$P^* = \frac{\Delta P}{\rho \nu^2 / d^2}$$

$$\mathrm{Re} = \frac{Ud}{\nu}$$

(2) Driving power/Shaft power, (P_s=Mω)

$$P_s = f(\rho, \upsilon, d, U)$$

Driving power to rotate the rotor inside the liquid filled channel depends on the rotor diameter (d), fluid density (ρ), kinematic viscosity (ν) and rotor tangential velocity (U).

No. of variables (dependent and independent), n= 5

No. of fundamental dimensions, m = 3 (That is, [M], [L], [T])

By Buckingham's theorem,

No. of dimensionless groups = n -m = 5-3 = 2

In present study, repeater variables ρ, d and U are selected to construct dimensionless groups.

The first Pi term can be expressed as,

$$\Pi_1 = P_s \rho^a d^b U^c$$

$$\text{Or, } [M^0L^0T^0] = [M^1L^2T^{-3}]\ [ML^{-3}]^a[L]^b\ [LT^{-1}]^c$$

For,

M: 0=1+a; a = -1

L: 0=2-3a+b+C; b = -2

T: 0=-3-c; c = -3

$$\Pi_1 = P_s \rho^{-1} d^{-2} U^{-3}$$

$$or$$

$$\Pi_1 = \frac{P_s}{\rho d^2 U^3}$$

The above process is repeated for finding the 2nd Pi term,

$$\Pi_2 = \nu \rho^a d^b U^c$$

$$\text{Or, } [M^0L^0T^0] = [L^2T^{-1}]\ [ML^{-3}]^a[L]^b\ [LT^{-1}]^c$$

For,

M: 0=a ; a = 0

L: 0=2-3a+b+C; b =-1

T: 0=-1-c; c = -1

$$\Pi_2 = \nu \rho^0 d^{-1} U^{-1}$$

$$or$$

$$\Pi_2 = \frac{\nu}{dU}$$

The final forms dimensionless groups are

$$\phi(\Pi_1, \Pi_2) = 0$$

$$\text{Or, } \quad \phi\left(\frac{P_s}{\rho d^2 U^3}, \frac{\nu}{Ud}\right) = 0$$

However, dimensionless driving power and Reynolds number can be expressed as,

$$T^* = \frac{P_s}{\rho d^2 U^3}$$

$$\mathrm{Re} = \frac{Ud}{\nu}$$

(3) Efficiency of pump, η

The efficiency is defined as the flow energy rise to the shaft power.

Flow energy rise = Flow rate × Pressure rise

$$= \frac{m}{\rho} \times \Delta P \quad ; \quad m \text{ is the mass flow rate.}$$

Shaft power, P_s= Torque × rotor angular speed

$$= M \times \omega$$

Efficiency, $\eta = \dfrac{\frac{m}{\rho} \times \Delta P}{M.\omega}$